Development of New Estimation Formula

for Globe Temperature and

Polyethylene Chamber for Research

of Heat Exchanges on Vegetation Surface:

Experimental Approach Based on Heat Budget

January 2014

Maki OKADA

Development of New Estimation Formula

for Globe Temperature and

Polyethylene Chamber for Research

of Heat Exchanges on Vegetation Surface:

Experimental Approach Based on Heat Budget

A Dissertation Submitted to

the Graduate School of Life and Environmental Sciences,

the University of Tsukuba

in Partial Fulfillment of the Requirements

for the Degree of Doctor of Philosophy in Science

(Doctoral Program in Geoenvironmental Sciences)

Maki OKADA

Abstract

Globe temperature is one of the elements in a heat stress index, Wet Bulb Globe Temperature. Globe temperature is not explicitly predicted in numerical simulation, and its stable measurement is difficult. Therefore, some empirical formulae were introduced to estimate globe temperature using standard meteorological variables, including air temperature, global solar radiation and wind speed. Observations and heat balance analysis of a globe revealed that globe temperature depended curvilinearly on global solar radiation. Additionally, wind speed influenced this dependence. The previous estimation formulae did not consider this physical law of a globe. Therefore, they had a systematic error of globe temperature depending on global solar radiation. Thus, we developed a new estimation formula based on heat balance of a black globe surface. The new formula was able to predict the curvilinear dependence of globe temperature on global solar radiation without any systematic error, and it also showed the globe temperature response to wind speed. In addition, the numerical constants of the newly developed formula were reevaluated from long-term observation data. Therefore, this new formula was applicable to estimate globe temperature under wide global solar radiation and wind speed.

Urban green area is one of the countermeasures for urban thermal environment. There is no clear answer for optimal vegetation size and its allocation to ameliorate an urban thermal environment. To answer these problems, basic knowledge should be enhanced on heat exchange process between vegetation and surrounding air, and how vegetation morphology affects this process. However, there is hardly a way to investigate how heat exchange changes according to vegetation size and allocation. Then, we developed a new apparatus, "polyethylene (PE) chamber",

to simulate heat exchange between vegetation surface and surrounding air with black Kent papers. The chamber was a 1.51 m-long tube structure with its two ends serving as an air inlet and an air outlet, and it was ventilated in the longitudinal direction using an exhaust fan. Therefore, there is an air temperature difference between the inlet and the outlet of the chamber. Using the air temperature difference between the inlet and the outlet and other heat balance components, we could evaluate the heat exchange process and its dependency to vegetation morphology. The measurement section of the PE chamber was covered with a thin polyethylene film. Such a thin polyethylene film transmits approximately 85% of both shortwave and longwave radiation. Therefore, the PE chamber was applicable to evaluate heat exchange under nocturnal radiative cooling. The outdoor experiments using black Kent papers instead of a real leaf and simple heat balance analysis of the PE chamber revealed the following points: 1) The colder surface did not necessarily produce the larger cooling the surrounding air. 2) Increase of the heat exchange surface resulted in an increase of convective heat transfer, but this relationship did not change linearly and approached a balance point. 3) The scattered heat exchange surface resulted in an increase of convective heat transfer.

Keywords; *Heat budget, Globe temperature, Estimation formula, Wet bulb globe temperature, Polyethylene chamber, Vegetation morphology, Convective heat transfer.*

Contents

iii

List of Tables

List of Figures

xvii

List of Symbols

List of Abbreviations

a_g Absorptivity of the globe for shortwave radiation

$a_{l\text{-}f}$ Absorptivity of the floor for longwave radiation

$a_{l\text{-}p}$ Absorptivity of the polyethylene film for longwave radiation

$a_{s\text{-}f\text{-}down}$ Absorptivity of the floor for downward shortwave radiation

$a_{s\text{-}p\text{-}down}$ Absorptivity of the polyethylene film for downward solar radiation

$a_{s\text{-}p\text{-}up}$ Absorptivity of the polyethylene film for upward solar radiation

A_f Area of the floor surface (m^2)

A_g Surface area of the black globe (m^2)

A_{nor} Projected area of direct shortwave radiation normal to beam (m^2)

A_p Area of the polyethylene film surface (m^2)

A_w Area of the sidewalls surface (m^2)

c_p Specific heat of air at constant pressure ($J\ K^{-1}\ kg^{-1}$)

$C_{H\text{-}g}$ Bulk coefficient of the globe

$C_{H\text{-}gr}$ Bulk coefficient of the ground surface

d Thickness of extruded polystyrene foam panel (= 0.03 m)

e Atmospheric water vapor pressure (hPa)

E Evapotranspiration ($kg\ m^{-2}\ s^{-1}$)

g_H Conductance for convective heat transfer ($W\ m^{-2}\ K^{-1}$)

g_R Conductance for radiative heat transfer ($W\ m^{-2}\ K^{-1}$)

g_V Conductance for ventilated heat transfer ($W\ m^{-2}\ K^{-1}$)

G Ground heat flux (W m^{-2})

$h_{c\text{-}f}$ Convective heat transfer coefficient at the floor surface (W m^{-2} K^{-1})

$h_{c\text{-}g}$ Convective heat transfer coefficient at the black globe surface (W m^{-2} K^{-1})

$h_{c\text{-}in}$ Convective heat transfer coefficient at the inside polyethylene film surface (W m^{-2} K^{-1})

$h_{c\text{-}k}$ Convective heat transfer coefficient at the Kent paper surface (W m^{-2} K^{-1})

$h_{c\text{-}out}$ Convective heat transfer coefficient at the outside polyethylene film surface (W m^{-2} K^{-1})

$h_{r\text{-}g}$ Radiative heat transfer coefficient at the black globe surface (W m^{-2} K^{-1})

$h_{r\text{-}in}$ Radiative heat transfer coefficient at the inside polyethylene film surface (W m^{-2} K^{-1})

$h_{r\text{-}out}$ Radiative heat transfer coefficient at the outside polyethylene film surface (W m^{-2} K^{-1})

h_t Heat transmission coefficient (W m^{-2} K^{-1})

H_g Convective heat flux at the globe surface (W m^{-2})

H_{gr} Convective heat flux at the ground surface (W m^{-2})

l Latent heat (J kg^{-1})

LAI Leaf area index

$L_{f\text{-}up}$ Longwave radiation flux density going upward at the floor surface (W m^{-2})

$L_{p\text{-}down}$ Longwave radiation flux density going downward at the inside film surface (W m^{-2})

$L_{p\text{-}up}$ Longwave radiation flux density going upward at the outside film surface (W m^{-2})

L_{sky} Longwave radiation flux density of the sky (W m^{-2})

L^{*}_{a} Net longwave radiation flux density above the polyethylene film (W m^{-2})

L^{*}_{b} Net longwave radiation flux density below the polyethylene film (W m^{-2})

L^{*}_{g} Net longwave radiation flux on the black globe surface (W m^{-2})

m	Optical air mass
$Q_{c\text{-}f}$	Convective heat flux at the floor surface (W)
$Q_{c\text{-}in}$	Convective heat flux at the inside polyethylene film surface (W)
$Q_{c\text{-}h}$	Convective heat flux at the cable heater surface (W)
$Q_{c\text{-}k}$	Convective heat flux at the Kent paper surface (W)
$Q_{c\text{-}n}$	Convective heat flux at the non-woven fabric surface (W)
$Q_{c\text{-}out}$	Convective heat flux at the outside polyethylene film surface (W)
$Q_{e\text{-}n}$	Latent heat flux at the non-woven fabric surface (W)
$Q_{g\text{-}f}$	Conductive heat flux through the floor (W)
$Q_{g\text{-}p}$	Conductive heat flux through the polyethylene film (W)
$Q_{g\text{-}w}$	Conductive heat flux through the sidewall (W)
Q_h	Heat supply by the heating cable (W)
Q_p	Heat transmission flux through the polyethylene film (W)
$Q_{r\text{-}a}$	Radiative cooling flux in a volume (W)
$Q_{r\text{-}in}$	Radiative heat flux at the inside polyethylene film surface (W)
$Q_{r\text{-}h}$	Radiative heat flux at the cable heater surface (W)
$Q_{r\text{-}out}$	Radiative heat flux at the outside polyethylene film surface (W)
Q_v	Heat flux due to ventilation (W)
$Q^{*}_{r\text{-}a}$	Net radiation flux above the polyethylene film (W)
$Q^{*}_{r\text{-}b}$	Net radiation flux below the polyethylene film (W)
$Q^{*}_{r\text{-}f}$	Net radiation flux at the floor surface (W)
$Q^{*}_{r\text{-}k}$	Net radiation flux at the upper surface of the Kent paper (W)
$Q^{*}_{r\text{-}n}$	Net radiation flux at the non-woven fabric surface (W)

$r_{l\text{-}f}$	Reflectivity of the floor surface for longwave radiation
$r_{l\text{-}p}$	Reflectivity of the polyethylene film for longwave radiation
$r_{s\text{-}f\text{-}down}$	Reflectivity of the floor surface for downward shortwave radiation
$r_{s\text{-}p\text{-}down}$	Reflectivity of the polyethylene film for downward shortwave radiation
$r_{s\text{-}p\text{-}up}$	Reflectivity of the polyethylene film for upward shortwave radiation
r^*_g	Radius of the globe (m)
S	Outdoor shortwave radiation flux density (W m^{-2})
S_d	Direct shortwave radiation (W m^{-2})
S_{dif}	Diffuse shortwave radiation (W m^{-2})
$S_{f\text{-}up}$	Shortwave radiation flux density going upward at the floor surface (W m^{-2})
S_{nor}	Direct shortwave radiation normal to the beam (W m^{-2})
S_o	Global solar radiation (W m^{-2})
$S_{p\text{-}down}$	Shortwave radiation flux density going downward at the inside film surface (W m^{-2})
S_{po}	Solar constant (W m^{-2})
$S_{p\text{-}up}$	Shortwave radiation flux density going upward at the outside film surface (W m^{-2})
S_{ref}	Reflected shortwave radiation (W m^{-2})
S^*_a	Net shortwave radiation flux density above the polyethylene film (W m^{-2})
S^*_b	Net shortwave radiation flux density below the polyethylene film (W m^{-2})
S^*_g	Net shortwave radiation flux to the globe surface (W m^{-2})
t_a	Atmospheric transmittance
$t_{l\text{-}p}$	Transimissivity of the polyethylene film for longwave radiation
$t_{s\text{-}p\text{-}down}$	Transimissivity of the polyethylene film for downward solar radiation
$t_{s\text{-}p\text{-}up}$	Transimissivity of the polyethylene film for upward solar radiation

T_a	Air temperature (K)
T_{db}	Dry bulb temperature (= Air temperature) (°C)
T_f	Floor surface temperature (K)
T_g	Globe temperature (°C)
T_{gr}	Ground surface temperature (K)
T_{in}	Air temperature inside the PE-chamber (K)
T_{inlet}	Air temperature at the air inlet of the PE-chamber (K)
T_k	Kent paper surface temperature (K)
T_n	Non-woven fabric surface temperature (K)
T_{out}	Outdoor air temperature (K)
T_{outlet}	Air temperature at the air outlet of the PE-chamber (K)
T_p	Polyethylene film temperature (K)
T_{sky}	Sky temperature (K)
T_{wb}	Wet bulb temperature (°C)
U	Wind speed (m s^{-1})
V	Ventilation rate of the exhaust fan (m^3 s^{-1})
α_{gr}	Albedo of the globe surface
β	Bowen's ratio
ΔT_a	Air temperature difference between the inlet and the outlet of the PE-chamber (outlet - inlet) (K)
ΔT_f	Temperature difference between the inside and the outside surface of the floor (inside - outside) (K)
ΔT_{in}	Temperature difference between the inside of the chamber and the inside surface of

the polyethylene film (inside – inside surface) (K)

ΔT_{out} Temperature difference between the outside surface of the polyethylene film and the outside of the chamber (outside surface – outside) (K)

ΔT_p Temperature difference between the inside and outside surface of the polyethylene film (inside surface – outside surface) (K)

ΔT_w Temperature difference between the inside and outside surface of the sidewalls (inside surface – outside surface) (K)

ε_f Emissivity of the floor surface

ε_g Emissivity of the globe

ε_{gr} Emissivity of the ground

ε_k Emissivity of the Kent paper surface

ε_p Emissivity of the polyethylene film

λ Heat conductivity of extruded polystyrene foam (= 0.04 W m^{-1} K^{-1})

ρ Air density (kg m^{-3})

θ Solar zenith angle (radian)

σ Stefan-Boltzmann's constant (= 5.67 x 10^{-8} W m^{-2} K^{-4})

ϕ Diameter of a thermocouple (mm)

List of Subscripts

a above

b below

c convection

d direct

db	dry-bulb
dif	diffusive
down	downward
f	floor surface
g	globe surface
gr	ground surface
h	cable heater
H	convective heat transfer
in	inside
inlet	inlet
k	Kent paper
l	longwave radiation
n	non-woven fabric
nor	normal
o	global
out	outside
outlet	outlet
p	polyethylene film
r	radiation
ref	reflective
R	radiative heat transfer
s	shortwave radiation
sky	sky

t	transmission
up	upward
v	ventilation
V	ventilated heat transfer
w	sidewall
wb	wet-bulb
$*$	net

1. Introduction

1.1 Influence of urban thermal environment

The expansion of urban areas is frequently associated with changes in the regional climate which often results in the deterioration of human environments. To mention a few: Daytime heat discomfort of urban residents caused by crowding of high-buildings, an increase of artificial exhaust heat, and so on. This heat discomfort remains during the nighttime by the urban heat island effect. In Japan, news of heat strokes have been appearing in the media on a daily basis every summer in recent years. For example, the number of patients transported by emergency vehicles as a result of heatstroke was 23,699 in July of 2013 (Fire and Disaster Management Agency 2013). This was the highest record in July since the investigation started in 2008 (Fire and Disaster Management Agency 2013). On the other hand, the ratio of nocturnal heatstroke dead was 40 percent during the summer in 2013 (Bureau of Social Welfare and Public Health, Tokyo Metropolitan Government 2013). Nocturnal heatstroke in urban areas has been getting more attention in recent years. Heatstroke patients tend to come from urban areas as a result of high population concentration. To mitigate the expansion of heat related injuries to urban residents, it is important to investigate the influence of urban thermal environment.

Global warming may deteriorate heat discomfort in an urban area. IPCC (2013) showed the global mean surface temperature change for the period 2016–2035 relative to 1986–2005. For example, there is a possibility that global mean surface temperature may increase by +2.6°C to +4.8°C under the Representative Concentration Pathway scenario 4.5. In addition, it is considered that the occurrence of heat waves will increase. Recently, a small number of previous studies investigated urbanization impact on regional climate with climate change scenarios using

the Weather Research and Forecasting (WRF) model (Georgescu et al. 2012; Kusaka et al. 2012). These studies focused on metropolitan areas, and their target period was limited to summer because people usually endure the highest heat stress during the warmest months. In Japan, for example, August average temperatures in the 2070s were projected to increase by +2.3°C compared to the 2000s in Tokyo, Nagoya, and Osaka (Kusaka et al. 2012). Furthermore, they projected the number of days with sleep disorders (e.g., minimum nighttime temperature exceeding 26°C) in August, and suggested that the occurrence of uncomfortable nights will increase in the future under climate change.

As of 2011, 52.1 percent of people in the world live in the urban areas (United Nations 2012). According to a projection by United Nations (2012), this ratio will increase to 67.1 percent in 2050. Thus, heat related injuries are expected to rise globally by an increase in urban population ratio. To mitigate and prevent heat related injuries to urban residents, it is important to assess the influence on urban resident's health and to provide effective countermeasures.

1.2 Evaluation of human health by thermal indices

Air temperature, alone, cannot adequately represent the human thermal environment. Meteorological factors and human metabolism determine human comfort and discomfort such as humidity, solar radiation, sweating and so on. To represent those numerically, various thermal indices have been developed (**Table 1.1**). Simple thermal indices consider heat exchange between human skin and its surrounding air only. Such indices express human comfort and discomfort using meteorological factors. For example, Operative Temperature (OT; Winslow et al. 1937) is calculated from air temperature, mean radiative temperature, convective heat transfer coefficient and radiative heat transfer coefficient to know physical effects of convection and

radiation. Thom (1959) considered that human discomfort was dependent on air temperature and humidity, and developed Temperature-Humidity Index (THI) to represent human discomfort. Also, Wet Bulb Globe Temperature (WBGT) developed by Yaglou and Minard (1957) considers air temperature, humidity and radiation to represent the risk for heat stroke. These thermal indices can simply evaluate human comfort and discomfort because they only need a few parameters. However, humans also regulate their body temperature by clothing and sweating. Thus, the energy balance of a human body regarding metabolism and conductance of the body (body skin and clothes) is necessary to adequately represent thermal sensation. There are many thermal indices dealing with human metabolism and clothing condition; i.e., Standard new Effective Temperature (SET*; Gagge et al. 1959), Predicted Mean Vote (PMV; Fanger 1972), Universal Thermal Climate Index (UTCI; Fiala et al. 2001). These thermal indices were calculated from meteorological factors, physiological responses and clothing condition, and those can represent thermal sensation adequately.

In recent years, evaluation of thermal sensation of urban residents using thermal indices has been necessary to predict heat stress risk arising from urban heat island. WBGT, SET* and PMV were recognized widely in architecture and environmental engineering fields. The thermal indices with physiological responses and clothing condition like SET* and PMV can adequately represent human discomfort. However, information of physiological response and clothing condition cannot be obtained from meteorological observation network and meteorological numerical models. Thus, it is also difficult to predict them using the meteorological numerical models in the future under climate change. The Japanese Ministry of Environment has been using Wet Bulb Globe Temperature (WBGT) as a preventive index for heat stroke at 841 cities in Japan since 2013. WBGT (Yaglou and Minard 1957) were proposed to prevent heat strokes

for soldiers training in hot and humid environments, and has been recognized as a standard heat stress index by public agencies worldwide (Budd 2008; ISO7243 1989; JIS Z 8504 1999). In recent years, some studies considered a preventive index for heat stroke from the physical law of human body (e.g., Mochida et al. 2007; Mochida and Sakoi 2010; Mochida and Sakoi 2011). However, such index required not only the meteorological data but also the clothing condition and the metabolic parameter. On the other hand, WBGT simply predict heat stress risk, because WBGT does not consider physiological responses and clothing condition. To evaluate heat stroke risk, WBGT requires measurement of three parameters: natural wet bulb temperature T_{wb}, globe temperature T_g, and air (dry bulb) temperature T_{db}. WBGT is defined as **Eq. 1.1**.

$$WBGT = 0.7T_{wb} + 0.2T_g + 0.1T_{db} \qquad (1.1)$$

Among three components for calculating WBGT, globe temperature is used to evaluate radiant heat, and is measured by installing thermometer into the center of a black globe. This black globe is a copper hollow sphere and is painted black. However, stable and long-term observation of globe temperature is generally difficult because a black globe is deteriorated by the rain and the wind. Also, WBGT cannot be predicted in meteorological numerical models because numerical models do not calculate globe temperature as default. Therefore, previous studies estimated globe temperature considering heat budget of a black globe surface (Hunter and Minyard 1999; Gaspar and Quintela 2009). Hunter and Minyard (1999) tried to estimate globe temperature by an iterative procedure on heat balance of a black globe surface. Dimiceli et al. (2011) simplified the formula proposed by Hunter and Minyard to a linear function formula to estimate globe temperature without an iterative procedure. The formula proposed by Dimiceli et

al. (2011) estimated globe temperature more accurately than the empirical formula. But, their formula required average fractional contribution of direct and diffuse solar radiation, as well as zenith angle. In general, we cannot get such meteorological factors from regular meteorological observation networks, nor from output data from meteorological numerical models. Therefore, it is difficult to use these formulae for estimating globe temperature.

On the other hand, there are empirical methods to estimate globe temperature using a few meteorological factors. For example, Takaichi et al. (2003) developed the empirical formula to predict WBGT under greenhouse work. The Japanese Ministry of the Environment uses the empirical formula proposed by Tonouchi and Murayama (2008) to predict WBGT. These empirical formulae estimate globe temperature using air temperature, wind speed and global solar radiation only. Such empirical formulae are also more convenient for numerical simulation studies because standard output factors are enough to use empirical formulae. Some recent studies predicted WBGT to evaluate heat stroke risk using numerical models (Ohashi et al. 2010; Kusaka et al. 2012; Takane et al. 2013). Since WBGT is used widely as a thermal index for heat stroke prevention, the estimation formula, which considers physical law of a black globe, is necessary to physically interpret calculated globe temperature.

1.3 Effect of vegetation for urban thermal environment

Variable countermeasures were considered to mitigate the influence of urban thermal environment to urban residents. Reducing energy consumption, wind blow trail and greening are typical countermeasures. Among them, an urban green area serves as an oasis in an urban area. Maruta (1972) distinguished the effect of an urban green area from "existence effect" in "utility effect". "Existence effect" was an urban green area that improved the atmospheric

environment surrounding built-up areas. Air temperature in an urban green area became lower mainly by evapotranspiration in daytime (e.g., Kanda et al. 1997; Spronken-Smith et al. 2000) and radiative cooling at night (e.g., Hamada and Mikami 1994; Narita et al. 2004). Also, it was considered that an urban green area transports clean air into the built-up areas (Eliasson and Upmanis 2000). On the other hand, "utility effect" was an urban green area that served as a resting place and an evacuation area in the time of disaster. Thus, an urban green area plays various and important roles in an urban area. However, an urban area does not have enough space to enlarge a green area. Urban planners have been seeking solutions to adequately mitigate the influence of urban thermal environment with vegetation size and its allocation (Oke 1989). To answer these problems, we should enhance our understanding of heat exchange between vegetation and its surrounding air and its relation to vegetation morphology: i.e., vegetation size and its allocation.

It has been known that the air temperature of a larger park is generally lower than that of a smaller one (e.g., Barradas 1991; Spronken-Smith and Oke 1998; Upmanis and Chen 1999; Chang et al. 2007). Therefore, it has been believed that a larger park is more effective to mitigate the urban thermal environment. Many previous studies observed the cooling effect of a larger park (e.g., Jauregui 1991; Ca et al. 1998; Narita et al. 2004; Sugawara et al. 2006; Okada et al. 2013a). A larger park, however, is more isolated from its surrounding built-up area in terms of a microclimate. As a result, the heat exchange between the park and the city is less enhanced. Lower temperatures measured in larger parks should thus be a consequence of isolation and resultant in attenuated heat exchange. Thus, it could be thought that larger parks do not cool the surrounding urban atmosphere effectively. Some of the previous studies argued that a scattered plant canopy was capable to cool the surrounding an urban atmosphere more effectively during

the daytime (Kanda and Hino 1990a, b; Honjo and Takakura 2000a, b; Huang et al. 2011). For example, Kanda and Hino (1990a, b) coupled plant physiology to an atmospheric model and effectively explained the isolation effect for daytime vegetation cooling. Also, Hagishima et al. (2007) revealed that scattered plant canopy increased evapotranspiration using pot plants. The target time period of these previous studies was the daytime. On the other hand, nocturnal cooling effect related to the vegetation morphology was not well known at the time.

There are four methods to investigate how vegetation morphology impacts heat exchange between vegetation and its surrounding air at night: 1) field experiment, 2) Computational Fluid Dynamics (CFD), 3) wind tunnel and 4) ventilated chamber. Field experiment is the appropriate way to evaluate the phenomena, but it is difficult to generalize the measurement results because real urban green areas are complex in structure and weather conditions fluctuate. CFD is a powerful tool to model all aspects of coupled convective heat and mass transfer at multiple scales, with which parameter and sensitivity studies could be performed in a straightforward way (Defraeye et al. 2013). In fact, CFD was used to investigate the daytime cooling by an urban park (e.g., Yu and Hien 2006; Rijal et al. 2010). However, enormous calculation resources are necessary to assure the small calculation grid and the extensive calculation field under stable atmospheric conditions at night (Arya 2001). A wind tunnel is an effective tool for fluid research, but it does not adequately evaluate the radiative and convective balance at vegetation surface. In addition, it is most difficult to evaluate nocturnal radiative cooling in a wind tunnel experiment. In the agricultural meteorology field, ventilated chambers are often used to evaluate the evapotranspiration from vegetation. Heat balance analysis of a ventilated chamber is useful to evaluate convective heat exchange. However, most ventilated chambers are built with rugged materials, hence they have high transmission in shortwave radiation, but little consideration is

given to longwave radiation (Denmead 1984). Therefore, a new method is needed to easily evaluate heat exchange processes between vegetation and its surrounding air particularly at night.

1.4 Objectives

In the future climate, it is worried that the urban thermal environment will be deteriorated by the urbanization and the advance of the global warming. The deterioration of the urban thermal environment leads to an increase of heat stroke patients, and the comprehensive approach is required to mitigate the urban thermal environment. The improvement of the reliability is the subject of the influence assessment on human health. Meanwhile, the accumulation of the basic knowledge about cooling the urban atmosphere is the subject to establish the suitable greening.

The purpose of this study are as follows: 1) to develop a new formula derived from heat balance at the black globe surface, and 2) to develop a new apparatus for investigating heat exchange between the vegetation surface and its surrounding air. The purpose of 1) contributes to the improvement of the reliability for evaluating the heat stress, and it is performed in Chapter 2. On the other hand, the purpose of 2) contributes to the accumulation of the basic knowledge about cooling the urban atmosphere, and it is performed in Chapter 3 and 4.

In Chapter 2, firstly, variations of globe temperature by meteorological factors are evaluated by a heat balance model of the black globe surface. Secondly, errors of the previous estimation formulae are examined by comparing with measurement data. Then, a new formula to estimate globe temperature is developed, and its versatility is enhanced using long-term observation data. In Chapter 3, a new experimental chamber "polyethylene (PE) chamber" is developed using a thin PE film that effectively transmits both shortwave and longwave radiation. The theory of

radiation and heat balance in the PE chamber and its performance are explained. In Chapter 4, we first examine whether the PE chamber correctly evaluates convective heat exchange by increasing the heat exchange area. Secondly, wet non-woven fabric is used to examine convective heat transfer on the evaporation surface in the PE chamber. Finally, relationships between convective heat transfer and heat exchange area, and with characteristic length, are investigated respectively.

Table 1.1. List of the representative index of thermal indices.

Using factor	Index name	Abbreviation	Author
Meteorology	Operative Temperature	OT	Winslow et al. (1937)
	Temperature-Humidity Index	THI	Thom (1959)
	Wet Bulb Globe Temperature	WBGT	Yaglou and Minard (1957)
Meteorology + Physiology	Standard new Effective Temperature	SET*	Gagge et al. (1959)
	Predicted Mean Vote	PMV	Fanger (1972)
	Universal Thermal Climate Index	UTCI	Fiala et al. (2001)

2. Proposal of a new formula to estimate globe temperature for calculating Wet Bulb Globe Temperature

2.1 Previous studies and objective

There are four kinds of methods to calculate WBGT (Wet Bulb Globe Temperature) as follows.

1) Wet bulb temperature, globe temperature and air temperature are measured first. Then, WBGT is calculated from the formula of Yaglou and Minard (1957).

2) Wet bulb temperature and air temperature are measured, and globe temperature is estimated by the physical estimation formula. Then, WBGT is calculated from the formula of Yaglou and Minard (1957) (Hunter and Minyard 1999; Gaspar and Quintela 2009).

3) Wet bulb temperature and air temperature are measured, and globe temperature is estimated by the empirical estimation formula. Then, WBGT is calculated from the formula of Yaglou and Minard (1957) (e.g., Takaichi et al. 2003; Tonouchi and Murayama 2008).

4) WBGT is estimated from empirical formula using the meteorological data without measuring wet-bulb and globe temperature (e.g., Nakai et al. 2006; Ono et al. 2006).

The methods 2), 3) and 4) could get WBGT without measuring globe temperature. The method 2) required some meteorological factors that cannot get from regular meteorological observation networks, nor from output data from meteorological numerical models. On the other hand, the methods 3) and 4) required meteorological factors obtained from regular meteorological observation networks. Horie and Fujiwara (2010) evaluated the accuracy of the methods 3) and 4) for calculating WBGT (Nakai et al. 1992; Takaichi et al. 2003; Ono et al.

2006; Tonouchi and Murayama 2008) in comparison with WBGT parameters measured on the building's roof. They concluded that the errors of estimation were minimized when using the formula proposed by Tonouchi and Murayama (2008). Thus, the estimation formula proposed by Tonouchi and Murayama (2008) is the most accurate empirical formula to estimate globe temperature. Globe temperature is generally discussed by the heat balance of convection and radiation at the black globe surface because of the high thermal conductivity of a copper hollow black globe. However, their formula given by Tonouchi and Murayama (2008) was not proposed on the basis of the physical law of a globe. The estimation formula, which considers the physical law of a globe, is required to estimate its temperature more accurately and enlarge the application of the estimation formula.

Takaichi et al. (2003) proposed the estimation formula for globe temperature, T_g, to evaluate the occupational risk of greenhouse workers (**Eq. 2.1**). On the other and, the formula proposed by Tonouchi and Murayama (2008) (**Eq. 2.2**) is currently in use by JME to calculate WBGT.

$$T_g = T_a + 0.090 S_o / \left(1 + 0.0037 S_o\right) \tag{2.1}$$

$$T_g = T_a - 0.3 + 0.0256 S_o - 0.18 U^{1/2} \left(S_o \leq 400 W\,m^{-2}\right) \tag{2.2a}$$

$$T_g = T_a + 12.1 + 0.0067 S_o - 2.40 U^{1/2} \left(S_o > 400 W\,m^{-2}\right) \tag{2.2b}$$

where T_g is globe temperature, T_a is air temperature, S_o is global solar radiation, and U is wind speed.

Using these empirical formulae is expected to calculate WBGT because recent studies conducted the outdoor experiment to calculate WBGT on various places (e.g., Suzuki et al. 2005;

Ohashi et al. 2009; Takane et al. 2013). Then, it is needed to know whether the previous estimation formulae can be applied to environments having surfaces different from where the formulae were experimentally derived and their numerical constants were determined. For example, an urban park plays a major role as places of the rest and the evacuation. Hence, it is important to evaluate WBGT in an urban park.

In this chapter, the goal is the development of a new formula to estimate globe temperature derived from the heat balance at the black globe surface. First, the applicability of the previous empirical formulae is examined by the meteorological observation and heat balance analysis at the globe surface. Second, a new formula is developed considering the heat balance at the black globe surface. Finally, the applicability of this new formula is enhanced by long-term observation data.

2.2 Development of a new estimation formula and its adaptation to an urban park

2.2.1 Measurements

In this chapter, we examine the applicability of the previous empirical formulae to the urban park. It has been known that the air temperature in a park is dependent on the area of a park (e.g., Barradas 1991; Spronken-Smith and Oke 1998; Upmanis and Chen 1999; Chang et al. 2007). Then, we conducted the experiment from September 8th to 10th, 2011 at three parks, each of a different size, in the city of Tsukuba: Doho park (20ha), Ninomiya park (4ha) and Kitamukai park (0.5ha). **Figure 2.1** shows the map plotting the observation sites. We measured globe temperature, air temperature, global solar radiation, and wind speed to examine the applicability of the previous empirical formulae (**Eqs. 2.1** and **2.2**). **Figure 2.2** shows the photos that the

measurement instruments were placed on each park. Air temperature was measured with a thermistor sensor (RTR-52A; T&D, Matsumoto, Japan) installed in an aspirated radiation shield (Murakami and Kimura 2010) (**Fig. 2.3a**). Globe temperature was measured with an RTR-52A thermistor inserted in a Vernon type globe with a diameter of 150mm (**Fig. 2.3b**). Global solar radiation and wind speed were measured using the weather station system (Vantage Pro2; Davis Instruments, San Francisco, USA) with a cup anemometer (**Fig. 2.3c**) and a solar radiation sensor (**Fig. 2.3d**). Each instrument was placed at a height of 1.5m above open sunlit turf grass in each park. The recording interval was 5sec for air and globe temperature, and 1min for wind speed and 10min for global solar radiation because of the restrictions of the data logging procedure. In general, a 10-min interval is too long to accurately measure variable solar radiation, so we did not use the instantaneous record, but three consecutive records at 10-min intervals collected when global solar radiation was continuously stable. A 20-min mean value was calculated from the three records by assuming a linear change between two adjacent records. Accordingly, all of the other variables were averaged over 20min.

The six thermistor sensors were calibrated using a quartz thermometer (DMT-621; Tokyo Denpa, Tokyo, Japan) and a stirring water bucket (**Fig. 2.4**). The stirring water is easy to keep water temperature uniformly because of the thin thermocline. Water temperature control is also easier than that in the air using the heater device, and heat transfer to the sensor is fast in the stirring water. Thus, using the stirring water is expected to calibrate thermistor sensors with high accuracy.

At first, the water temperature was set to 0°C by putting ice into the stirring water bucket. Then, the water temperature was risen to 50°C in steps of 5°C using the heater device put in the stirring water bucket. Temperatures were recorded in every 5sec keeping the water temperature

during 1min. From the experimental result, linear regression equations of each thermistor sensor were derived using the least squares method. The errors of each thermistor sensor from the quartz thermometer became ±1.0°C after the calibration experiment (**Fig. 2.5**)

2.2.2 Verification of the heat balance model at the black globe surface

The response of globe temperature to the meteorological factors was investigated by heat balance analysis at the black globe surface. Considered about heat balance at the black globe surface, we assume that the black globe is placed above an open flat surface where the black globe can view only the sky and the ground.

Heat balance at the black globe surface (**Fig. 2.6**) is given by:

$$S_g^* + L_g^* + H_g = 0 \tag{2.3}$$

where S_g^* is net shortwave radiation flux on the black globe surface, L_g^* is net longwave radiation flux on the black globe surface and H_g is convective heat flux.

By reference to previous studies (Toriyama et al. 2001; Ohashi et al. 2009; Gaspar and Quintela 2009), net shortwave radiation flux on the globe surface, S_g^*, is given by the sum of three components, namely, the direct beam from the sun, diffuse radiation from the sky and the reflection of shortwave radiation (**Eq. 2.4**):

$$S_g^* = a_g \left(\frac{S_{nor}}{4} + \frac{S_{dif}}{2} + \frac{S_{ref}}{2} \right) \tag{2.4}$$

where S_{nor} is direct shortwave radiation normal to the beam, S_{dif} is diffuse shortwave radiation, S_{ref} is reflected shortwave radiation, a_g is absorptivity of the globe for shortwave radiation.

Note that the flux density of S_{nor} is based on the surface perpendicular to the solar beam, whereas S_{dif} and S_{ref} are based on a horizontal surface (**Fig. 2.7**). The constant in the denominator of the first term in the parentheses results from the ratio of the projected globe area perpendicular to the direct solar beam (πr_g*^2) to the surface of the globe ($4\pi r_g*^2$) (**Fig. 2.7a**). Also, the constants in the denominator of the last two terms result from the reciprocal of the view factor of the globe surface relative to the sky and that to the ground surface (**Fig. 2.7b**). When global solar radiation at the horizontal surface, S_o, and the albedo of the surrounding ground surface, α_{gr}, are used instead of S_{nor} and S_{ref}, **Eq. 2.4** is rewritten as:

$$S_g^* = a_g \left(\frac{S_o - S_{dif}}{4\cos\theta} + \frac{S_{dif}}{2} + \frac{\alpha_{gr} S_{dif}}{2} \right) \tag{2.5}$$

where θ is solar zenith angle.

Net longwave radiation flux on the globe surface, L_g^*, is given by **Eq. 2.6**. Again, the constants in the denominator correspond respectively to the reciprocal of the view factor of the globe relative to the sky and to the ground.

$$L_g^* = \varepsilon_g \left(\frac{L_{sky}}{2} + \frac{(1-\varepsilon_{gr})L_{sky}}{2} + \frac{\varepsilon_{gr}\sigma T_{gr}^4}{2} - \sigma T_g^4 \right) \tag{2.6}$$

where L_{sky} is longwave radiation flux density of the sky, T_{gr} is ground surface temperature, T_g is globe temperature, ε_{gr} is emissivity of the ground, and ε_g is emissivity of the globe.

16

Convective heat flux at the globe surface, H_g, in **Eq. 2.3** is given by **Eq. 2.7**:

$$H_g = \rho c_p C_{H-g} U \left(T_a - T_g \right)$$

(2.7)

where C_{H-g} is the bulk coefficient of the globe, U is wind speed, and T_a is air temperature.

Toriyama et al. (2001) observed globe temperature and other meteorological factors in the outdoors, and determined the bulk coefficient of the globe as a residual of heat balance at the globe surface. They proposed the empirical form to calculate the bulk coefficient of the globe from the relationship between the bulk coefficient of the globe and wind speed (**Eq. 2.7**):

$$C_{H-g} = 0.0156 U^{-0.82}$$

(2.8)

In order to calculate **Eq. 2.6**, the surrounding ground surface temperature, T_{gr}, is required. The heat balance at the ground surface is given by:

$$\left(1 - \alpha_{gr} \right) S_o + \varepsilon_{gr} \left(L_{sky} - \sigma T_{gr}^4 \right) = H_{gr} + lE + G$$

(2.9)

where lE is latent heat flux and G is ground heat flux.

By introducing Bowen's ratio, β, and assuming that the heat flux, G, into the soil is 30% of the net radiation at the ground surface (Oke 1987), **Eq. 2.9** can be rewritten as follows:

$$0.7 \left\{ \left(1 - \alpha_{gr} \right) S_o + \varepsilon_{gr} \left(L_{sky} - \sigma T_{gr}^4 \right) \right\} - H_{gr} - \frac{H_{gr}}{\beta} = 0$$

(2.10)

Convective heat flux at the ground surface, H_{gr}, in **Eq. 2.10** is calculated using a bulk transfer equation.

$$H_{gr} = \rho c_p C_{H-gr} U \left(T_{gr} - T_a \right) \qquad (2.11)$$

The bulk coefficient of the ground, C_{H-gr}, in **Eq. 2.11** is a transport coefficient for a grass field with a plant height of 0.1m in calm and unstable conditions (Kondo 2000).

$$C_{H-gr} = 0.0065 \left(T_{gr} - T_a \right)^{1/3} \qquad (2.12)$$

Equation 2.12 can be applied to wind speed below 2.0 m s^{-1}. In this study, the observed mean wind speed was 0.57 m s^{-1}, the maximum wind speed was 1.3 m s^{-1}, and no measurement exceeded 2.0 m s^{-1}.

Diffuse solar radiation, S_{dif}, is required to calculate **Eq. 2.5**, but no diffuse solar radiation was measured in the experiment. We first calculated both direct and diffuse solar radiation for a clear sky from **Eqs. 2.13** and **2.14** given by Campbell and Norman (1998) using 1365 W m^{-2} for the solar constant and 0.7 for atmospheric transmittance. We then estimated the diffuse solar radiation by multiplying the observed global solar radiation by the ratio of S_{dif} to the sum of S_d and S_{dif} calculated from the following formulae.

$$S_d = S_{po} t_a^m \cos\theta \qquad (2.13)$$

$$S_{dif} = 0.3\left(1 - t_a^m\right) S_{po} \cos\theta \tag{2.14}$$

where S_{po} is solar constant, t_a is atmospheric transmittance, m is optical air mass.

The solar zenith angle, θ, for the experimental place and time was obtained from the website of the Ephemeris Computation Office, Public Relations Center, National Astronomical Observatory of Japan (http://eco.mtk.nao.ac.jp/koyomi/index.html).

Longwave sky radiation, L_{sky}, in **Eq. 2.6** is calculated from Brunt's formula (Brunt 1939) with air temperature, T_a, and water vapor pressure, e, at ground level according to the parameters of Watanabe (1965):

$$L_{sky} = \left(0.52 + 0.063\sqrt{e}\right) \sigma T_a^4 \tag{2.15}$$

In the model calculation, the values of 0.92 and 0.95 were used for the absorptivity (Toriyama et al. 2001) and the emissivity (Ohashi et al. 2009) of the black globe surface, respectively. The albedo and the emissivity of the surrounding ground used 0.2 (Munn 1966) and 0.95 by assuming a grass surface.

For comparison with the observations, the black globe and the surrounding ground surface temperature were calculated by giving air temperature, humidity, global solar radiation, and wind speed observed in the experiment. The Bowen's ratio was introduced to simulate the change in wetness and resultant surface temperature of the surrounding ground in the heat balance model. As we did not observe the Bowen's ratio in the experiment, we first determined the Bowen's ratio so as to minimize errors in estimating globe temperature by the model. The

root mean square error (RMSE) of estimation became the smallest at a Bowen's ratio of 1.1. The Bowen's ratio thus determined corresponds to that obtained on a dry grass surface in the previous studies (e.g., Inoue et al. 2004). Our experiment sites were covered with turf grass, which had often been mowed but not artificially irrigated. At the time of the experiment the grass surface was dry so that the value of 1.1 is considered to be in a reasonable range of the Bowen's ratio in this study.

The predicted globe temperature by the heat balance model was compared to that observed in **Fig. 2.8** where RMSE was at its minimum of 1.2°C at the Bowen's ratio of 1.1. **Figure 2.8** indicates that the heat balance model developed here can properly simulate the response of globe temperature to weather variables in three different parks and the site-specific deviation of prediction errors across the experiment sites was not significant.

2.2.3 Dependence of globe temperature on weather and ground surface conditions

Previously proposed empirical formulae were derived from observations in a dry greenhouse (Takaichi et al. 2003: **Eq. 2.1**) or on the building's roof (Tonouchi and Murayama 2008: **Eq. 2.2**), whereas our data were collected in green parks. One can speculate that wind conditions and/or the surrounding ground surface temperature would differ among these sites and thus would affect globe temperature through convection and exchange of longwave radiation. To evaluate the effects of wind and surrounding ground surface conditions, we conducted the analysis using the heat balance model introduced in the section 2.2.2.

Suppose that a black globe is similarly exposed to wind and sunlight in an open space, whether in a park or on a building's roof. In the model calculation, air temperature was fixed at the mean value of 30.3°C averaged over the observed data from 27.6 to 33.3°C, and water vapor

pressure was also fixed at the mean value of 23.1hPa averaged over the observed data from 13.5 to 30.0hPa and the Bowen's ratio at 1.1 as determined above. Direct and diffuse solar radiation was calculated from **Eqs. 2.13** and **2.14** by changing the solar zenith angle under an assumed clear sky.

Since globe temperature largely depends not only on solar radiation and/or wind speed but also on air temperature, we plotted the globe minus air temperature difference, $T_g - T_a$, as a function of global solar radiation (**Fig. 2.9**). The observed $T_g - T_a$ is shown separately for wind speed ranges above and below 0.5 m s^{-1} in **Fig. 2.9**. The calculated $T_g - T_a$ by the heat balance model was also plotted in the same figure for a wind speed of 0.2, 0.57 and 1.3 m s^{-1}; each corresponding to the minimum, mean and maximum wind speed observed in the experiment.

Both the observed and the calculated $T_g - T_a$ similarly responded to the change in global solar radiation curvilinearly. As represented in **Eq. 2.5**, the curvilinear response of $T_g - T_a$ to global solar radiation results from the term that includes the cosine of the solar zenith angle θ. This response is considered to be significant as a behavior of globe temperature in relation to solar radiation.

The observed $T_g - T_a$ in **Fig. 2.9** tended to increase as wind speed decreased and suggests that wind speed had an influence on the curvilinear response to global solar radiation. The influence of wind speed was more clearly explained by the model calculation. The variation induced by changes in wind speed became large as global solar radiation increased.

We then evaluated the effect of the surrounding ground surface temperature on globe temperature by altering the Bowen's ratio in the range between 0.2 for well-watered turf grass (Kondo 1994) and 5.0 for an asphalt surface (Kondo 1994). **Figure 2.10** shows the temperature difference, $T_g - T_a$, calculated for three levels of the Bowen's ratio at a wind speed of 0.2 m s^{-1},

21

the observed minimum (**Fig. 2.10a**) and of 0.57 m s^{-1}, the observed mean (**Fig. 2.10b**). At a

larger wind speed the curves were similar to those in **Fig. 2.10**, but $T_g - T_a$ decreased and the

distance between the curves became closer (data not shown).

Globe temperature depended on the surrounding ground surface temperature, especially

when solar radiation was intense, and globe temperature increased as Bowen's ratio became

larger (**Fig. 2.10**). For example the globe and the ground surface temperature calculated by the

heat balance model was 44.3°C and 41.2°C at a Bowen's ratio of 0.2, 46.4°C and 55.3°C at 1.0,

and 47.5°C and 62.0°C at 5.0, respectively, when global solar radiation was 900 W m^{-2} and wind

speed 0.57 m s^{-1}. The increase of globe temperature accompanied by an increased Bowen's ratio,

however, tended to diminish. As seen in **Fig. 2.10**, the distance between the curves for $\beta = 0.2$

and $\beta = 1.0$ was much larger than that between the curves for $\beta = 1.0$ and $\beta = 5.0$, and the curve

for Bowen's ratio larger than 5.0 was close to the curve for 5.0 (data not shown). This means that

the Bowen's ratio, which measures the moisture of the surrounding ground surface, by itself

cannot affect globe temperature except a surface that is as wet as well-watered grass vegetation

or water surface.

2.2.4 Applicability of the previous empirical formulae

The observed globe minus air temperature difference, $T_g - T_a$, was plotted as a function of

global solar radiation in the three parks together with the functions given by the two empirical

formulae in **Fig. 2.11a**. **Equation 2.1** is a hyperbolic function of global solar radiation and

disregards wind speed. To examine the change of the estimated globe temperature depending on

wind speed in **Eq. 2.2**, **Eq. 2.2** was calculated for four wind speeds, 0.0, 0.57, 2.0 and 4.0 m s^{-1}.

Equation 2.2 consists of two linear bivariate functions of global solar radiation and wind speed;

one is used for global solar radiation above 400 W m^{-2} and the other for global solar radiation below that value. The two functions are not contiguous at this boundary, and thus show a notable discontinuity especially at wind speeds near zero.

Comparison of the estimates by the empirical formulae with the observed values clearly showed systematic errors **(Fig. 2.11b)**. The globe temperature was estimated by giving observed global solar radiation, wind speed and air temperature to the empirical formulae and the errors in the estimate [estimated T_g minus measured T_g] were plotted against global solar radiation. **Equation 2.1** overestimated globe temperature over almost the entire range of global solar radiation, especially at low radiation intensity. Horie and Fujiwara (2010) reported a similar result, although their location on a building's roof was different thermally and environmentally from ours in an urban park. **Equation 2.2** also overestimated globe temperature, but the error depended to a considerable extent on global solar radiation: the errors were very small for global solar radiation below 400 W m^{-2}, where the first formula in **Eq. 2.2** was used. Above 400 W m^{-2}, where the second formula was used in **Eq. 2.2**, the errors decreased as global solar radiation increased. Therefore, the errors were largest near the discontinuity where we switched from one formula to the other. As clearly seen in **Fig. 2.11a**, the slope of the second formula of **Eq. 2.2** was different from that of the observations, whereas the slope of the first formula was quite similar to the slope of the observations.

We first hypothesized that the overestimation by **Eqs. 2.1** and **2.2** was caused by site-specific differences in surrounding ground surface conditions such as surface moisture. The former model calculation, however, did not support this hypothesis, but it suggested that wind speed was more influential on the relationship between globe temperature and global solar radiation. One possible reason for the overestimation is, hence, the different wind regime at the

measurement sites where the empirical formulae and their numerical constants were derived. In fact, **Eq. 2.1**, which has no wind term, was derived in a greenhouse, and **Eq. 2.2** was derived from observations made on a building's roof. Wind conditions (especially turbulence) both in a greenhouse and on a building's roof may be considerably different from those at ground level in a park. The numerical constants used in the empirical formulae may therefore reflect a bias specific to the site where they were determined.

To determine values for the constants applicable to the urban park environment, we fitted the formulae to the observed data. As **Eq. 2.1** is a non-linear function of global solar radiation, the downhill Simplex method (Nelder and Mead 1965), an optimization technique to search the minimum value of a nonlinear function, was used to determine the constants that minimized the sum of squared errors. We used the operation program (Kobayashi 1981) with the algorithm to evaluate whether the value converged the local minimum. Then, it was confirmed that the values did not converge to other minimums with the change of initial conditions. Multiple regression was used to fit **Eq. 2.2** to the data. The newly determined constants of **Eqs. 2.1** and **2.2** are shown in **Table 2.1**. In comparison with **Fig. 2.9**, the errors in the new estimate were significantly improved (**Fig. 2.12**): the root mean square error (RMSE) of **Eq. 2.1** was reduced from 4.3°C to 1.0°C, and RMSE of **Eq. 2.2** was reduced from 1.6°C to 0.76°C, after the numerical constants were altered.

The discontinuity in **Eq. 2.2** became small but was not eliminated, since it is inherent in the form of the formulae. $T_g - T_a$ calculated with **Eq. 2.1** more closely followed the observed curvilinear response of globe temperature to global solar radiation, although it could not reflect differences related to wind speed.

2.2.5 Development of a new formula

As the analysis based on the heat balance at the black globe surface revealed that globe temperature depended curvilinearly on global solar radiation and wind speed influenced this dependence, we derive a new formula to estimate globe temperature by rearranging the formulae of the physical model of the black globe surface.

Eqs. 2.6 and **2.7** were substituted into **Eq. 2.1**:

$$S + L_a - \varepsilon_g \sigma T_g^4 + h_{c-g}\left(T_a - T_g\right) = 0 \tag{2.16}$$

where h_{c-g} is the convective heat transfer coefficient of the globe: $h_{c-g} = \rho c_p C_{H-g} U$, $L_a = \varepsilon_g \left(L_{sky} + \varepsilon_{gr}\sigma T_{gr}^4\right) / 2$.

Equation 2.16 is rearranged with respect to the term $(T_g - T_a)$.

$$h_{c-g}\left(T_g - T_a\right) + \varepsilon_g \sigma\left(T_g^4 - T_a^4\right) = S + L_a - \varepsilon_g \sigma T_a^4 \tag{2.17}$$

The nonlinear term $(T_g^4 - T_a^4)$ in **Eq. 2.17** was linearized according to the Taylor expansion.

$$\left(h_{c-g} + h_{r-g}\right)\left(T_g - T_a\right) = S + L_a - \varepsilon_g \sigma T_a^4 \tag{2.18}$$

$$T_g = \left(S + L_a - \varepsilon_g \sigma T_a^4\right) \Big/ \left(h_{c-g} + h_{r-g}\right) + T_a \tag{2.19}$$

where h_{r-g} is the radiative heat transfer coefficient, that is, $h_{r-g} \approx 4\varepsilon_g \sigma T_a^3$.

Suppose that h_{c-g} is a simple function of wind speed (McAdams 1954), that is, $h_{c-g} = k_1 U +$

k_2. Also, suppose that air temperature, global solar radiation and wind speed are only variables available for the inputs. Then **Eq. 2.19** is reduced to the form:

$$T_g = T_a + (S + j_1)/(k_1 U + j_2)$$

(2.20)

where $j_1 = L_a - \varepsilon_g \sigma\, T_a^{\,4}$, $j_2 = k_2 + h_{r\text{-}g}$.

Since global solar radiation, S_o, is the only variable obtainable from weather stations, S must be replaced with S_o. As suggested by **Eq. 2.1** in **Fig. 2.12a**, a hyperbolic function adapts flexibly to the nonlinear response of globe temperature to global solar radiation. We incorporated this idea and obtained the new formula shown below:

$$T_g = T_a + (S_o + a)/(b S_o + c U + d)$$

(2.21)

The numerical constants in **Eq. 2.21** were determined as in **Table 2.1** by fitting the formula to the observed data by the downhill Simplex method and the resulting curves are shown in **Fig. 2.13a**. $T_g - T_a$ calculated with **Eq. 2.21** is able to respond nonlinearly to global solar radiation without any discontinuity and it also responds to wind, unlike $T_g - T_a$ calculated with **Eq. 2.1**, although the errors in the estimate were of a similar order among the three formulae **(Fig. 2.13b)**; the RMSE for **Eq. 2.21** was 0.78°C. **Equation 2.1** requires only two constants but cannot respond to changes in wind speed. **Equation 2.2** requires totally six constants to respond to global solar radiation and wind speed. On the other and, the new formula (**Eq. 2.21**) requires four constants, and estimate globe temperature nonlinearly to global solar radiation without any

26

discontinuity.

As mentioned in section 2.2.3, the observations were conducted under a limited range of wind speeds. Wind speed exceeded 1.0 m s^{-1} in only five of the 96 observations, and the maximum observed speed was 1.3 m s^{-1}. Thus, the numerical constants determined from those data can be applied to calm wind conditions under which severe heat stress is usually encountered, but may not be used for wind speed out of the experimental range (wind speed below 1.3 m s^{-1}).

2.3 Application to an extension area of a new formula

2.3.1 Data

Japanese Ministry of the Environment has observed globe temperature of major cities in Japan from 2006 (Japanese Ministry of the Environment 2010). Data is collected hourly from June to September. Relatively long observation data were left in four major cities of Tokyo, Nagoya, Osaka and Fukuoka (data in Nagoya on September in 2006 was not recorded only). Therefore, we used the globe temperature data of these cities to reevaluate the numerical constants of the formula proposed by Okada and Kusaka (2013). In addition, we used air temperature, global solar radiation and wind speed measured in the meteorological station. Globe temperature was observed by placing a Vernon type globe with a diameter of 150mm at a height of 1.5m above the grass field in the meteorological station. The height of anemometer is different in each meteorological station: 35.1m in Tokyo, 17.8m in Nagoya, 22.9m in Osaka and 34.6m in Fukuoka. These heights are needed to correspond to the heights of the globe placed at. Additionally, global solar radiation are needed to convert into work of the average time same as air temperature and wind speed, because global solar radiation recorded in the meteorological

station is the hourly integral solar radiation (unit : MJ m^{-2}). However, JME uses the observation data obtained from Japan Meteorological Agency (hereafter referred to as JMA) without correcting specially, when they predict WBGT. Therefore, we also used the long-term observation data without correcting. Global solar radiation (W m^{-2}) was given from dividing hourly integral solar radiation by 3600sec. Consequently, we used the total of 35105 data which global solar radiation was more than 0.0 W m^{-2} and globe temperature was not zero or deficit values. The data included the observation data at the time of rainfall or after the rainfall.

Figure 2.14 shows the histogram of air temperature, wind speed, global solar radiation and globe temperature used to reevaluate the numerical constants of **Eq. 2.21**. The average air temperature was 28.1°C and air temperature 25 ~ 30°C was mostly recorded (**Fig. 2.14a**). The average wind speed was 3.1 m s^{-1}, and wind speed 2.0 ~ 4.0 m s^{-1} was mostly recorded (**Fig. 2.14b**). The average wind speed 3.1 m s^{-1} was bigger than the average wind speed 0.6 m s^{-1} in Okada and Kusaka (2013). Maximum global solar radiation was 1083.3 W m^{-2}, and global solar radiation less than 100.0 W m^{-2} was mostly recorded (**Fig. 2.14c**). The average globe temperature was 34.1°C, and globe temperature 25 ~ 30°C was mostly recorded (**Fig. 2.14d**).

2.3.2 Correction of a new formula using long-term observation data

As with the determination of numerical constants of **Eq. 2.21**, the downhill simplex method was used to reevaluate the numerical constants of **Eq. 2.21**. **Equation 2.22** shows the corrected Okada and Kusaka's formula.

$$T_g = T_a + \frac{S_o - 38.5}{0.0217S_o + 4.35U + 23.5} \qquad (2.22)$$

The estimated globe temperature by **Eq. 2.22** was compared to that observed in **Fig. 2.15**. The regression line showed a little far from a straight line of $y = x$, and the estimated globe temperature little overestimated the observed one. RMSE showed 2.39°C.

Figure 2.16 shows the dependence of temperature difference, $T_g - T_a$, on global solar radiation. The estimated globe temperature, T_g, was calculated using the observed air temperature, wind speed, global solar radiation by **Eq. 2.22**. Although the usage data included the measurement data under rainy weather, the temperature difference increases depending on global solar radiation nonlinearly according to cosine law shown by Okada and Kusaka (2013). The observed temperature difference varied largely, and the largest variance was shown in the range of global solar radiation 200 ~ 800 W m^{-2}. The dependence of temperature difference on wind speed was not shown clearly. Thus, it is considered that temperature difference is influenced by other factors than global solar radiation and wind speed. On the other hand, the estimated temperature difference increased nonlinearly and clearly depending on global solar radiation. Also, the estimated temperature difference became small in the stronger wind speed, since convective heat exchange on the black globe surface stimulates in the strong wind speed. **Figure 2.17** shows a box plot of the estimated error for global solar radiation. The estimated error was calculated from subtracting the observed globe temperature from the estimated one. The numerical parameters a ~ d in **Eq. 2.21** are considered as constants in Okada and Kusaka (2013). Thus, their formula, for example, cannot evaluate the dependence of direct shortwave radiation on solar elevation. Also, their formula cannot consider the difference of atmospheric radiation between fine and cloudy weather. Therefore, the large estimated error was shown in **Fig. 2.17**. However, the median of the estimated error concentrated on around 0.0°C. Additionally, the 75 and 25 percentile values were less than ±5.0°C. Thus, it was indicated that

29

Eq. 2.22 did not have the systematic error on global solar radiation.

Figure 2.18 shows the dependence of temperature difference $T_g - T_a$ on wind speed. The large variation of temperature difference was shown not only in the observed results but also in the estimated ones. Furthermore, its variation was the largest in the low wind speed. The temperature difference increased depending on global solar radiation (**Fig. 2.16**). Thus, it is considered that temperature difference is affected more by global solar radiation. However, the estimation formula given by Takaichi et al. (2003) overestimated the outdoor globe temperature (Okada and Kusaka 2013). Their formula does not consider the effect of wind speed. Therefore, the wind speed term in the estimation formula cannot be excluded easily. **Figure 2.19** shows the box plot of the estimated error for wind speed. The estimated error for wind speed also varied widely like that for global solar radiation. The convective heat transfer coefficient of the black globe surface depends on zenith angle and solar radiation (Dimiceli et al. 2011). This dependence cannot be represented in the formula given by Okada and Kusaka (2013). The median of the estimated error in each wind speed concentrated on around 0.0°C. Therefore, it was indicated that **Eq. 2.22** did not also have the systematic error on wind speed.

2.3.3 Estimated globe temperature obtained from a new formula in each city and year

For the determination of the numerical constants by Okada and Kusaka (2013), the range of wind speed and the number of the samples were limited. On the other hand, the numerical constants of **Eq. 2.22** were decided by long-term observation data in four major cities from 2006 to 2012. Therefore, **Eq. 2.22** has the wide applicability than Okada and Kusaka (2013).

Globe temperature changes depending on global solar radiation and wind speed. This

tendency of globe temperature is expected to differ in each city and year. Thus, we investigated the tendency of globe temperature in each city and year.

Figure 2.20 showed the histogram of globe temperature in each city. In the cities except for Nagoya, globe temperature $25 \sim 30°C$ was mostly recorded. On the other hand, globe temperature $40 \sim 45°C$ was mostly recorded in Nagoya. **Table 2.2** showed the result that the regression analysis with observed and estimated globe temperature by **Eq. 2.22** in each city. The slope of the regression line of Tokyo was almost 1.0 most, while the regression line in other cities deviated slightly from $y = x$ line. However, RMSE of Osaka and Fukuoka was the smallest, while that of Tokyo was biggest. **Figure 2.21** shows the relationship between temperature difference and global solar radiation in each city. In Tokyo, there were a lot of samples of smaller temperature difference $0 \sim 5°C$ under global solar radiation $400 \sim 800$ W m^{-2}. These samples deviate from the non-linear relations between global solar radiation and temperature difference. Hence, it is considered that these samples caused the large RMSE in Tokyo.

Figure 2.22 shows the histogram of globe temperature in each year. Globe temperature $25 \sim 30°C$ was mostly recorded except for 2010. On the other hand, globe temperature $30 \sim 35°C$ was mostly recorded in 2010 (**Fig. 2.22e**). Additionally, the number of sample of globe temperature $45 \sim 50°C$ in 2010 was the most of all years. The climatic normal difference of the mean temperature of the summer in 2010 was $+1.64°C$. This value was the highest value after 1988 when the meteorological statistics started by the Meteorological Agency. **Table 2.3** showed the result that the regression analysis with the observed and estimated globe temperature by **Eq. 2.22** in each year. The slope of the regression line turned in a negative value from 2010. In addition, RMSE after 2010 were bigger than that before 2010. **Table 2.4** shows the average values of air temperature, global solar radiation, wind speed, globe temperature in each year.

Maximum averaged air temperature and globe temperature were 29.2°C and 35.7°C, respectively. Both values were recorded in 2010, and 2010 was the hottest year in latest years from the viewpoint of thermal environment. The averaged global solar radiation after 2010 was higher than that before 2010. Then, we counted the number of the samples which global solar radiation was more than 1000 W m^{-2}. As a result, they were 55 in 2006, 76 in 2007, 93 in 2009, 142 in 2010, 128 in 2011 and 156 in 2012, respectively. It was clear that there were many days with high global solar radiation after 2010. The median of the estimated error of **Eq. 2.22** is +2.41°C with global solar radiation more than 1000 W m^{-2}, and **Eq. 2.22** tended to underestimate the observation data during the high global solar radiation (**Fig. 2.17**). Therefore, it is considered that higher global solar radiation caused that RMSE after 2010 was bigger than that before 2010.

2.4 Summary

In this chapter, we rearranged the heat balance equation at the black globe surface to estimate globe temperature from air temperature, global solar radiation, and wind speed. This new formula could estimate globe temperature using meteorological factors given from regular meteorological observation network despite of the derivation from the physical law of the black globe.

First, we investigated the responses of globe temperature on the weather conditions and the surrounding ground conditions as part of a study intended to evaluate heat stress on humans. Since the previous formulae used were originally derived from observations made on a building's roof or in a greenhouse, we examined whether they were applicable to an urban park environment. The two formulae examined here overestimated the globe temperature experimentally observed in three urban parks. We first speculated that this overestimation was

caused by differences in the condition of the surrounding ground, such as surface moisture, but the heat balance analysis at the black globe surface did not support this speculation. Globe temperature did increase when the surrounding ground surface was dryer, but the increase was too low to account for the overestimation by the empirical formulae. The heat balance analysis suggested that wind speed was more influential on globe temperature and site-specific difference in wind regime caused the overestimation of the formulae.

When we reevaluated the numerical constants in the previous empirical formulae by fitting them to the observed data, the estimated errors were largely reduced. There is bias in the constants of these formulae, specific to the site where they were empirically determined. Therefore, the constants need to be reevaluated at each site where the model is applied. Although we reduced the errors by reevaluating the constants, there were still inherent defects in the formulae, including no effect of wind speed and a discontinuity in the predicted nonlinear response to global solar radiation. Using the heat balance model at the black globe surface, we then derived a new empirical formula for globe temperature. This new formula showed the nonlinear dependence on global solar radiation without any discontinuity and takes into account wind speed.

Since the numerical constants in the new empirical formula were determined under low wind speed, we then reevaluated them using long-term observation data. Error analyses were conducted whether the new formula showed the systematic error related to global solar radiation and wind speed. The median of the estimated error concentrated around 0.0°C in both of global solar radiation and wind speed. Thus, it was indicated that the reevaluated new formula did not have the systematic error.

This new formula was derived from the heat balance at the black globe surface unlike the

previous empirical formulae, and did not show the systematic error on global solar radiation and wind speed. In addition, the new formula was fertile because the numerical constants were determined using long-term data in wide global solar radiation and wind speed. Thus, this new formula will be useful to monitor and predict WBGT in observation network and meteorological model.

Table 2.1. Previous empirical formulae (**Eqs. 2.1** and **2.2**) with newly determined numerical constants and the newly proposed formula (**Eq. 2.21**). The constants in the **Eqs. 2.1** and **2.21** were determined by downhill Simplex method (Nelder and Mead 1965). The constants in the **Eq. 2.2** were determined by multiple regression.

Eq. 2.1	$T_g = T_a + 0.0271 S_o / \left(1 + 0.000563 S_o\right)$
Eq. 2.2a	$T_g = T_a + 0.557 + 0.0277 S_o - 2.39 U^{1/2} \left(S_o \leq 400\, W\, m^{-2}\right)$
Eq. 2.2b	$T_g = T_a + 6.40 + 0.0142 S_o - 3.83 U^{1/2} \left(S_o > 400\, W\, m^{-2}\right)$
Eq. 2.21	$T_g = T_a + \left(S_o - 30.0\right) / \left(0.0252 S_o + 10.5 U + 25.5\right)$

Table 2.2. Results of the regression analysis between the observed values and the estimated values of globe temperature in each city. Globe temperature was observed from June to September. Data period was from 2006 to 2012. Estimated globe temperature was calculated from **Eq. 2.22**.

City name	Slope of regression line	Interpret of regression line (°C)	Coefficient of determination	RMSE (°C)
Tokyo	1.02	0.66	0.89	2.76
Nagoya	0.91	2.27	0.93	2.39
Osaka	0.92	3.01	0.93	2.15
Fukuoka	0.89	3.22	0.93	2.23

Table 2.3. Results of the regression analysis between the observed values and the estimated values of globe temperature in each year. Data period was from June to September. Estimated globe temperature was calculated from **Eq. 2.22**.

Year	Slope of regression line	Interpret of regression line (°C)	Coefficient of determination	RMSE (°C)
2006	0.97	+0.98	0.93	2.16
2007	0.98	+0.82	0.93	2.07
2008	0.99	+0.54	0.93	2.15
2009	1.00	+0.34	0.92	2.13
2010	1.02	-0.89	0.91	2.55
2011	1.02	-1.04	0.90	2.59
2012	1.01	-0.63	0.87	2.95

Table 2.4. Average of air temperature, global solar radiation, wind speed and globe temperature in each year. Data period was from June to September.

Year	Air temperature (°C)	Global solar radiation (W m^{-2})	Wind speed (m s^{-1})	Globe temperature (°C)
2006	27.6	303.8	3.00	33.2
2007	28.1	318.3	3.10	33.8
2008	28.0	326.7	2.81	34.1
2009	27.2	320.8	3.00	33.2
2010	29.2	368.7	3.08	35.7
2011	28.1	345.2	3.36	34.1
2012	28.5	364.3	3.16	34.7
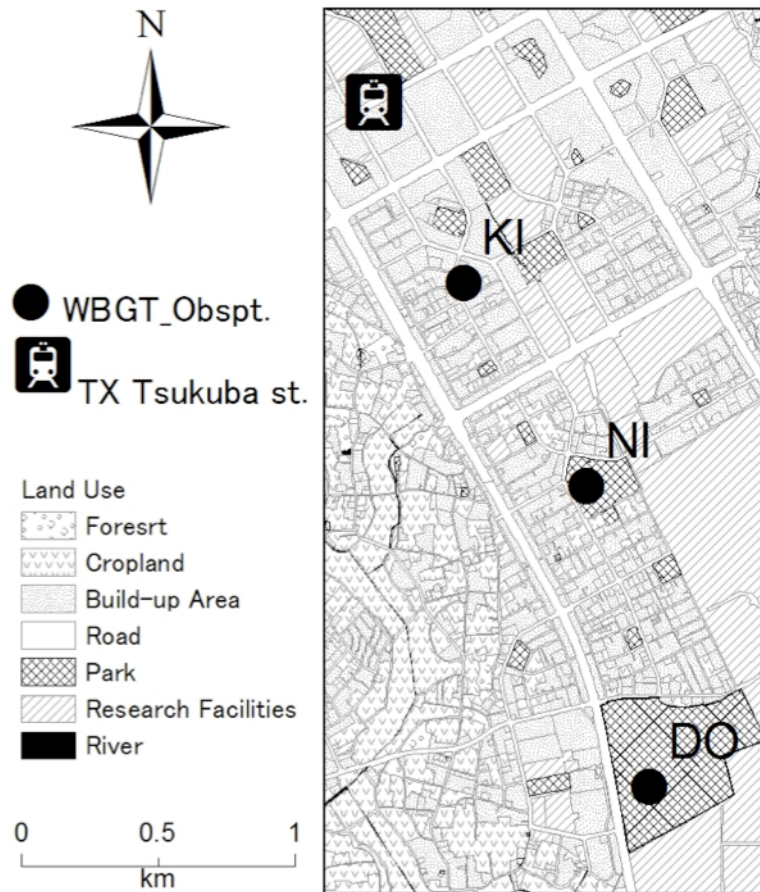
Fig. 2.1. Map of observation site and the land use in Tsukuba city. Circle symbols indicate the observation point in each park. All observations were conducted on an open grass field. Abbreviations of KI, NI, DO mean the name of the urban parks: Kitamukai park, Ninomiya park and Doho park, respectively. The Area of Kitamukai park, Ninomiya park and Doho park were 0.5ha, 4ha and 20ha, respectively.
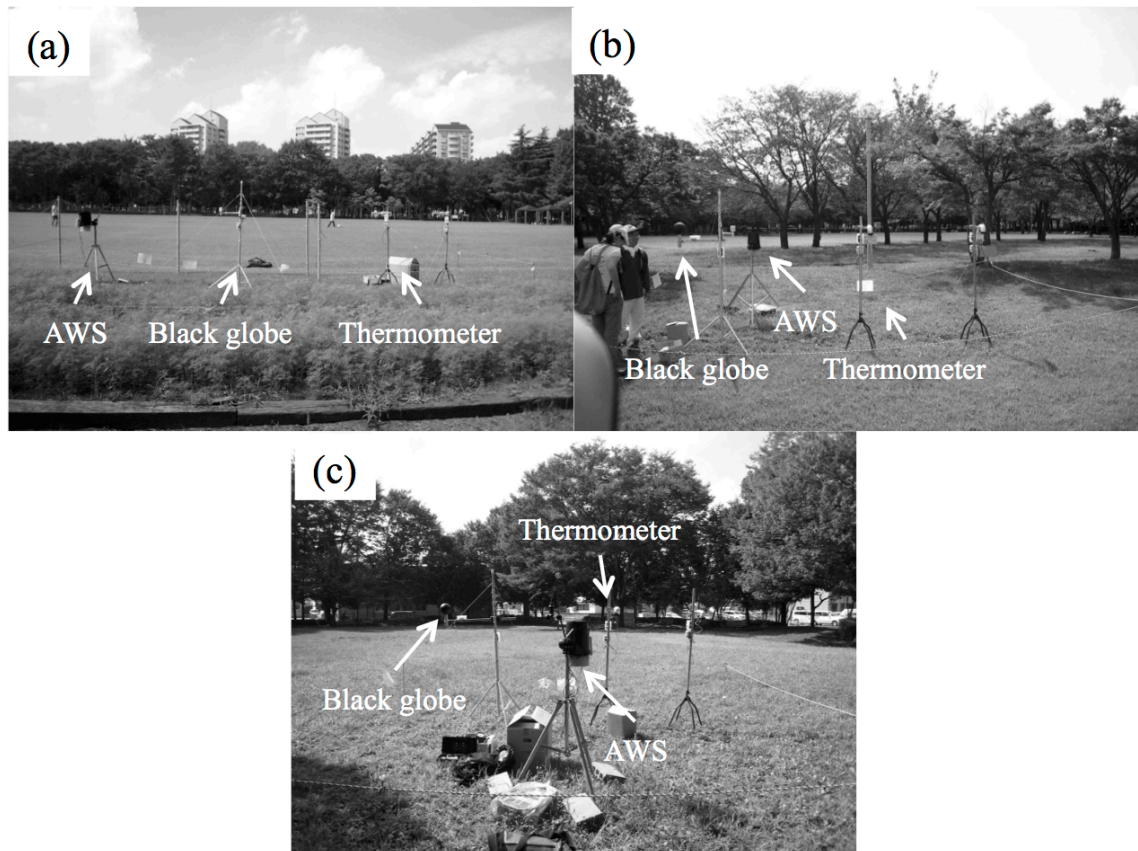
Fig. 2.2. View of the measurements in Doho park (a), Ninomiya park (b) and Kitamukai park (c). AWS means Automatic Weather Station: Vantage Pro2 in this study. Observation was conducted on an open grass field in the park. All sensors were placed at a height of 1.5m above the ground surface. Photo (a) was taken from east side. Photo (b) and (c) were taken from north side.
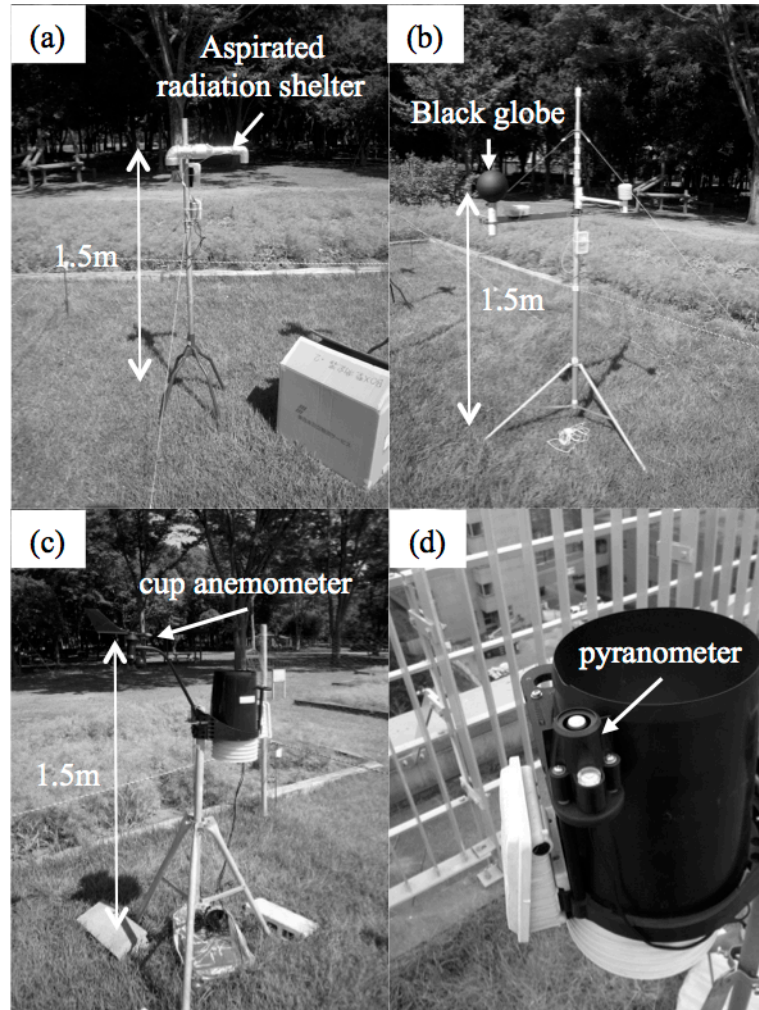
Fig. 2.3. View of the measurement using the aspirated radiation shield by Murakami and Kimura (2010) (a), the Vernon type globe (b), the automatic weather station (c), and the pyranometer installed the automatic weather station (d).
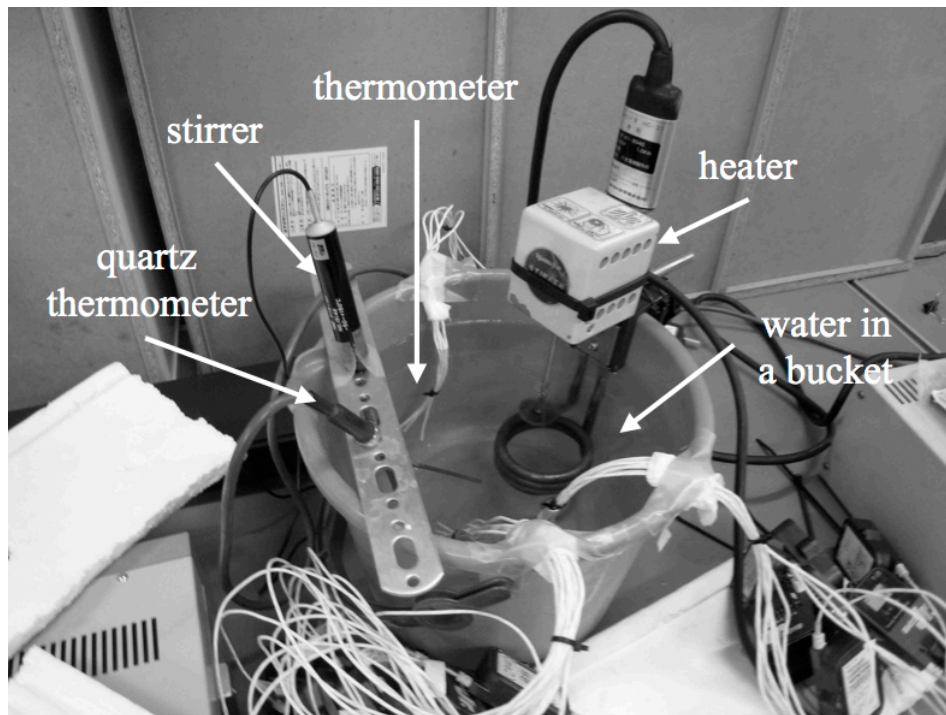
Fig. 2.4. View of the calibration experiment for thermometers using a quartz thermometer and a stirring water bucket. Sensors of the thermometers were put into the water in the bucket. The water in the bucket was stirred by a stirrer. The water temperature was firstly set to 0°C by putting ices into the stirring water, and increased the water temperature gradually using the heater.

(a)

(b)
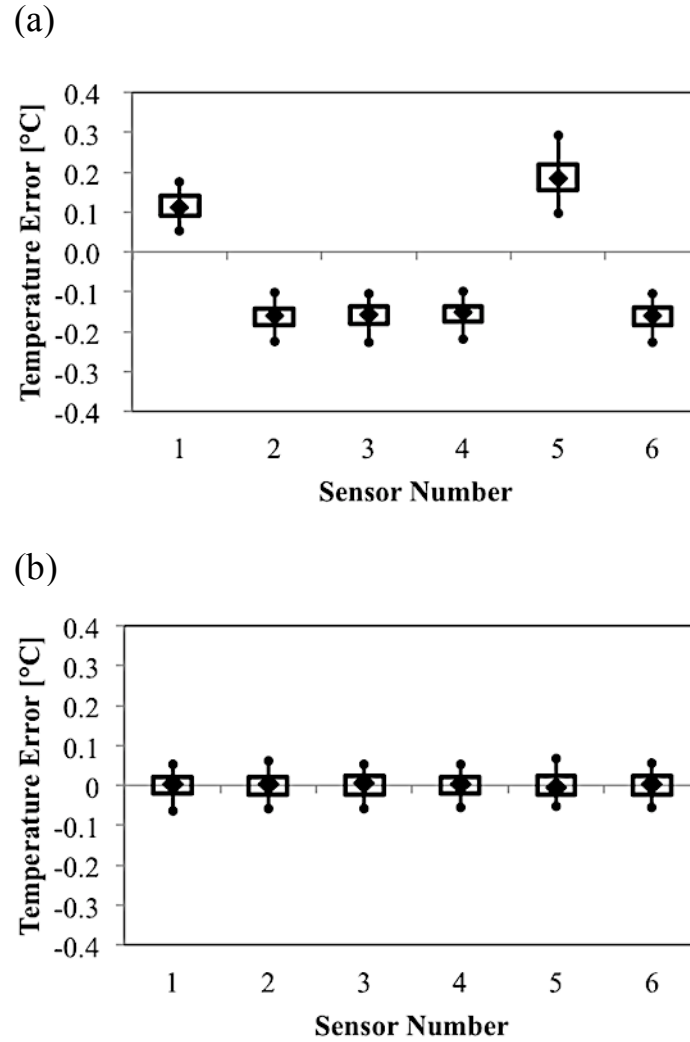
Fig. 2.5. Box plot of the temperature error of each thermistor sensor from the quartz thermometer before (a) and after (b) the calibration. Upper and lower circle symbols indicate the maximum and minimum values, respectively. Upper and lower sides of the box indicate 75 and 25 percentile values. Diamond symbols indicate the median values.
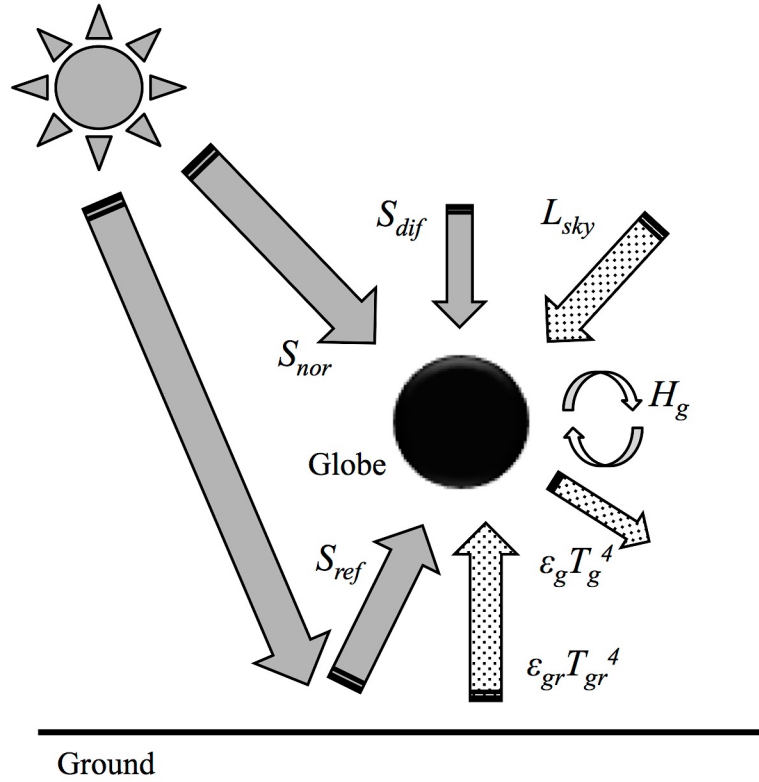
Fig. 2.6. Schematic of heat balance of the black globe. By the high thermal conductivity of the copper, it can be considered that heat balance of the black globe consists of radiation and convection. S_{nor} is direct shortwave radiation normal to the beam, S_{dif} is diffuse shortwave radiation, S_{ref} is reflected shortwave radiation, a_g is absorptivity of the globe for shortwave radiation. L_{sky} is longwave radiation flux density of the sky, T_{gr} is ground surface temperature, T_g is globe temperature, e_{gr} is emissivity of the ground, and e_g is emissivity of the globe. H_g is convective heat flux at the globe surface.
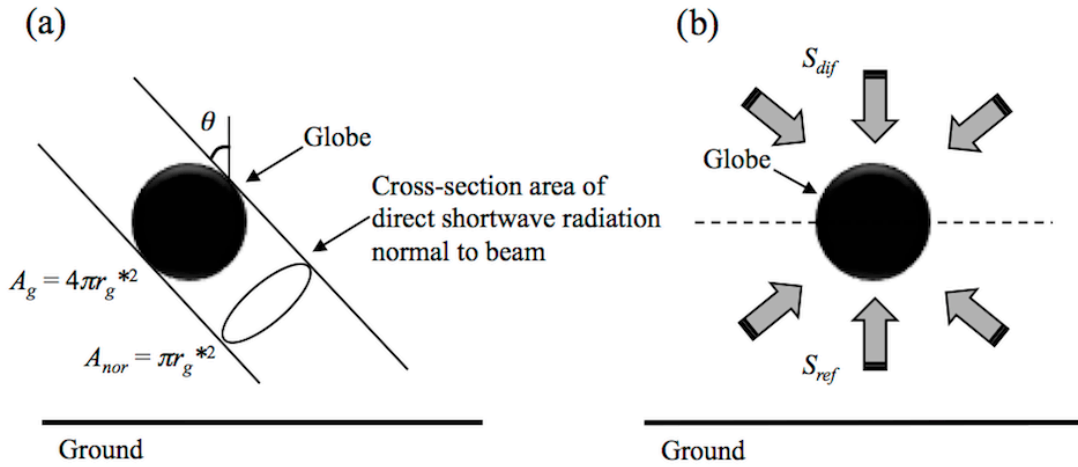
Fig. 2.7. Schematic of shortwave radiation incidnet to the black globe. (a) Direct shortwave radiation normal to beam. (b) Diffuse and reflective shortwave radiation. Direct shortwave radiation normal to beam enters based on the surface perpendicular to the solar beam. In this study, we assumed that diffuse shortwave radiation, S_{dif}, enters the upper half of the black globe, and reflected shortwave radiation, S_{ref}, enters the lower half of the black globe. A_g is the surface area of the black globe, A_{nor} is the projected area of direct shortwave radiation normal to beam, and θ is solar zenith angle.
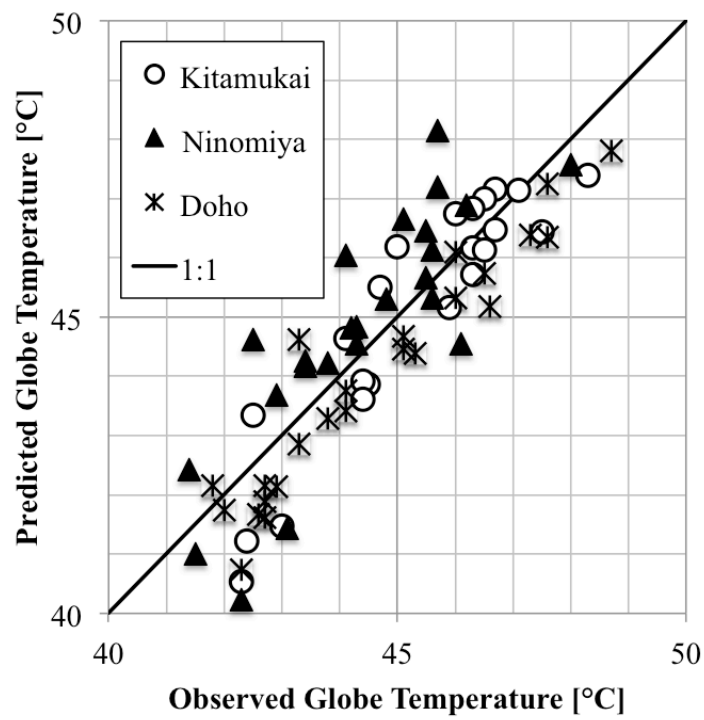
Fig. 2.8. Comparison of globe temperature predicted by the physical model to that observed. Symbols denote the data observed in three different parks. Globe temperature is predicted by the observed air temperature, solar radiation, wind speed and water vapor pressure as input variables and the Bowen's ratio fixed at 1.1.

46
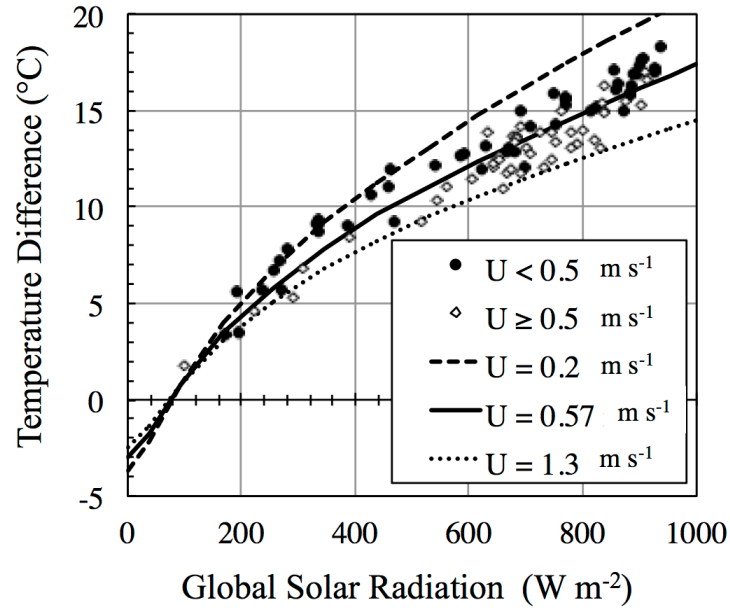
Fig. 2.9. Effects of wind speed on the relationship between the temperature difference, $T_g - T_a$, and global solar radiation calculated by the physical model. Bowen's ratio is fixed at 1.1. The solid line indicate the calculated data by the physical model for wind speed 0.57 m s^{-1}, the broken line for wind speed 0.2 m s^{-1}, and the dashed line for wind speed 1.3 m s^{-1}. The black dots indicate the observed data for a wind speed range below 0.5 m s^{-1} and the open diamonds above 0.5 m s^{-1}.
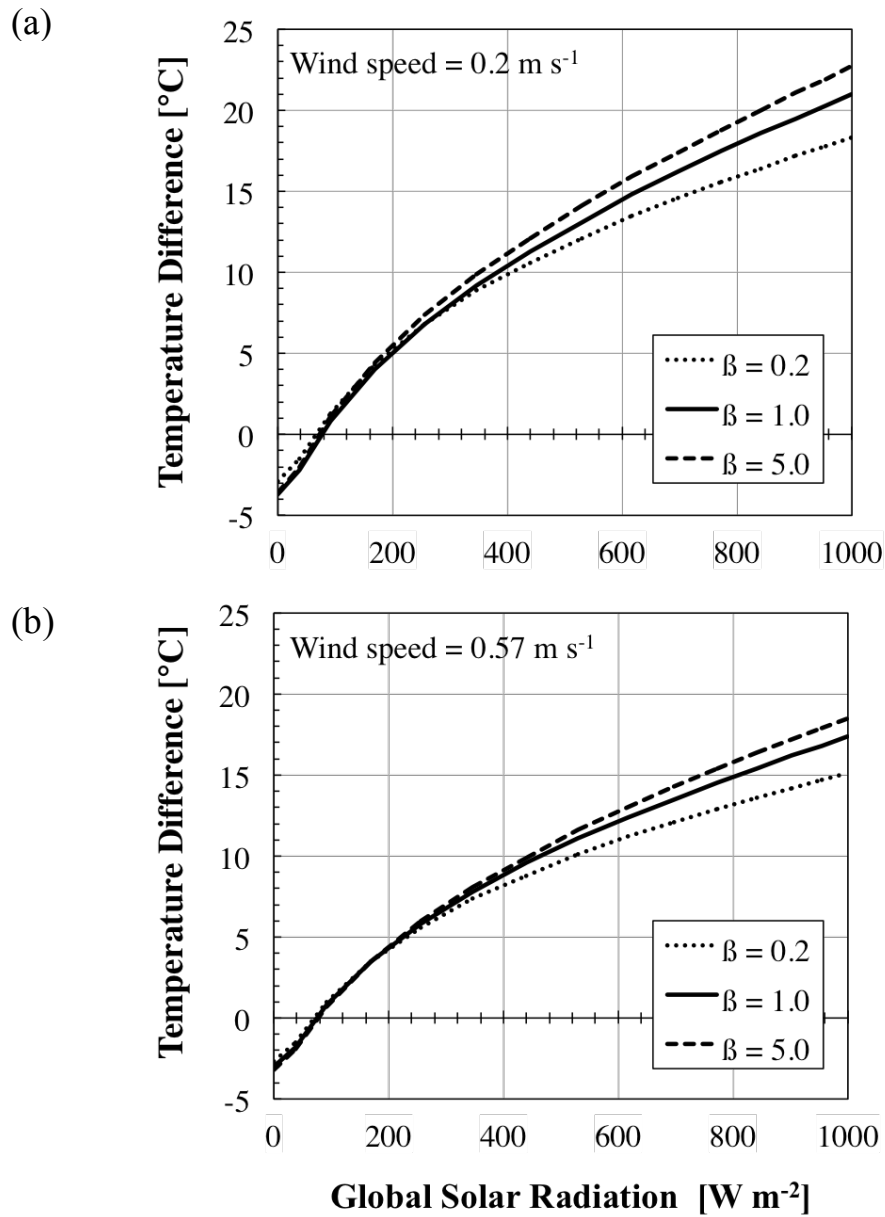
Fig. 2.10. Effects of Bowen's ratio of the surrounding ground surface on the relationship between the temperature difference, $T_g - T_a$, and global solar radiation calculated by the physical model; at a wind speed of 0.2 m s^{-1} (a) and at 0.57 m s^{-1} (b). The solid line indicate the calculated data by the physical model for Bowen's ratio at 1.0, the broken line for Bowen's ratio at 5.0, and the dashed line for Bowen's ratio at 0.2.

48
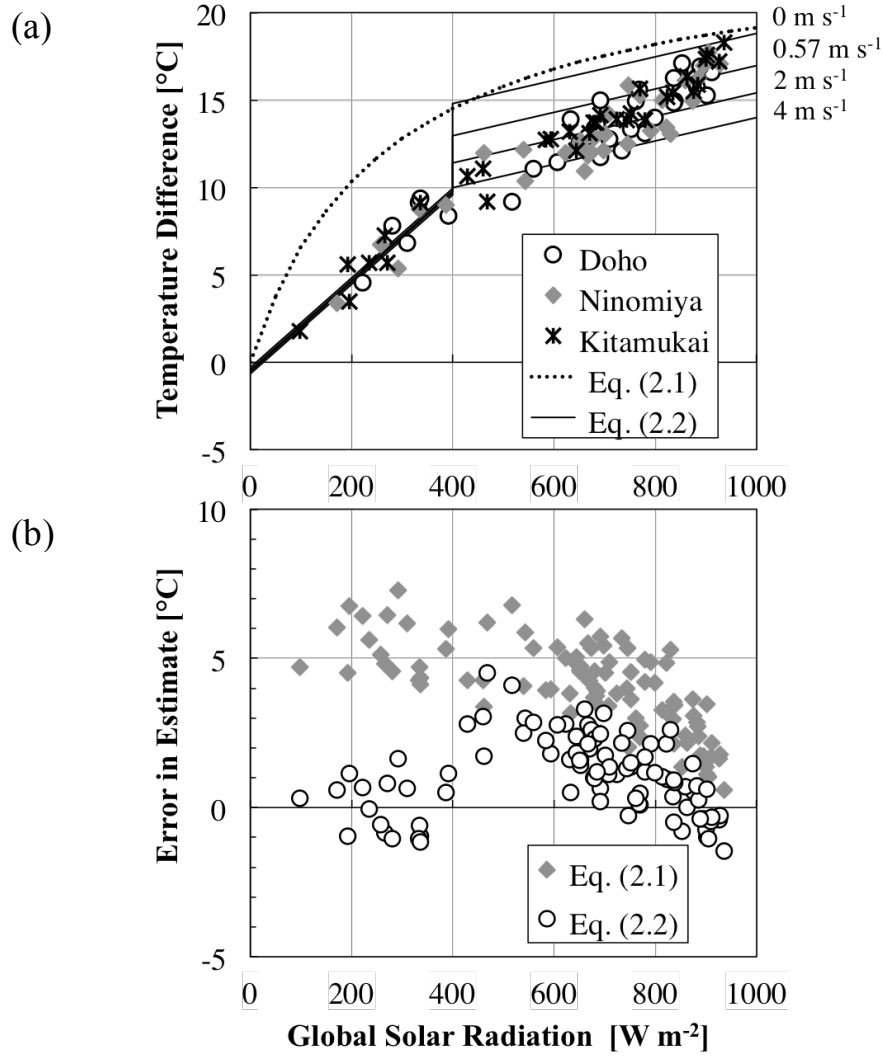
Fig. 2.11. (a) Dependence of the temperature difference, $T_g - T_a$, calculated from the two empirical formulae on global solar radiation. Symbols denote the observed data in three different parks. The dotted line indicates the calculation by **Eq. 2.1** and the solid lines by **Eq. 2.2** at four wind speeds. (b) Errors in estimate [estimated T_g from **Eqs. 2.1** or **2.2** minus measured T_g] as a function of global solar radiation. The diamond symbols indicate the error in estimate calculated from **Eq. 2.1**, and the circle symbols calculated from **Eq. 2.2**.
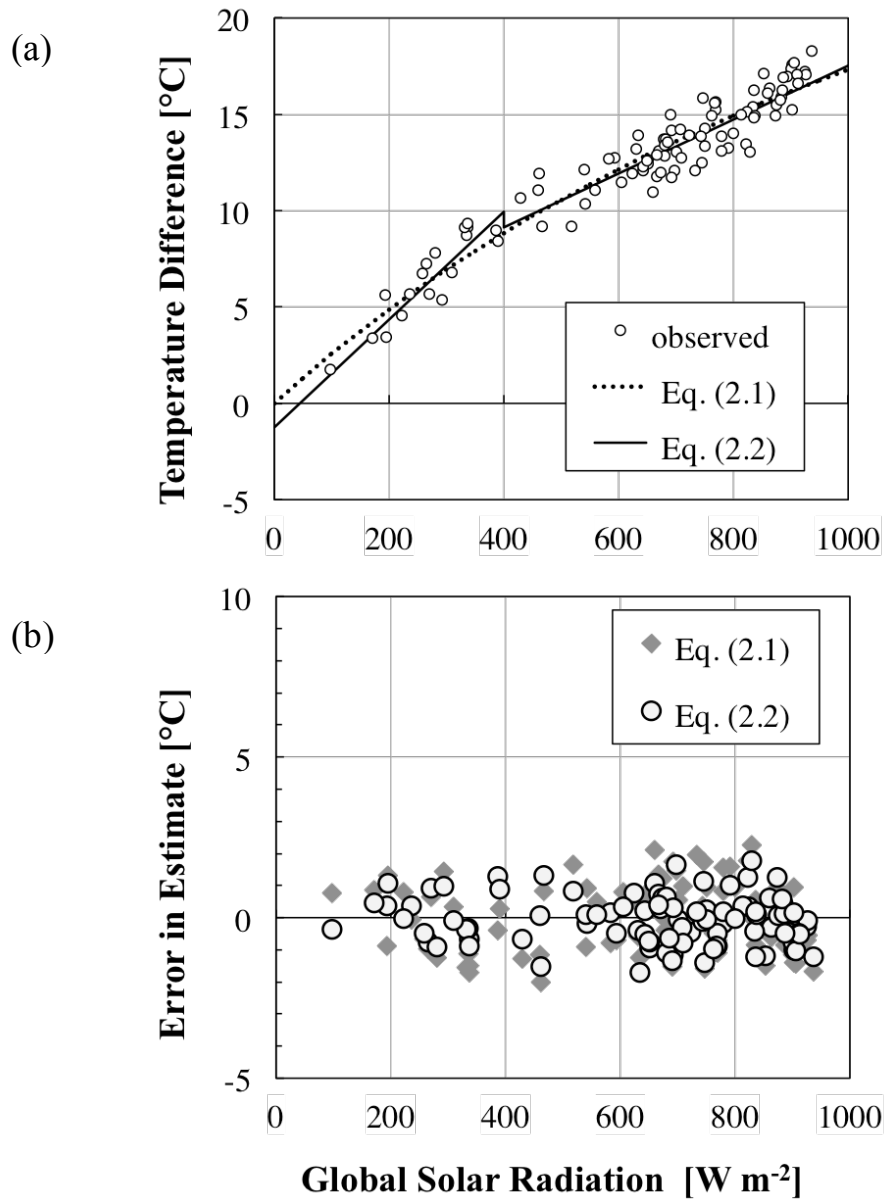
Fig. 2.12. (a) Dependence of the temperature difference, $T_g - T_a$, calculated from the two empirical formulae with newly determined numerical constants (see **Table 2.1**) on global solar radiation together with the observed values. **Eqs. 2.1** and **2.2** are plotted for a wind speed of 0.57 m s^{-1}. (b) Errors in estimate [estimated T_g minus measured T_g] given by the two formulae. The diamond symbols indicate the error in estimate calculated from **Eq. 2.1**, and the circle symbols calculated from **Eq. 2.2**.

50
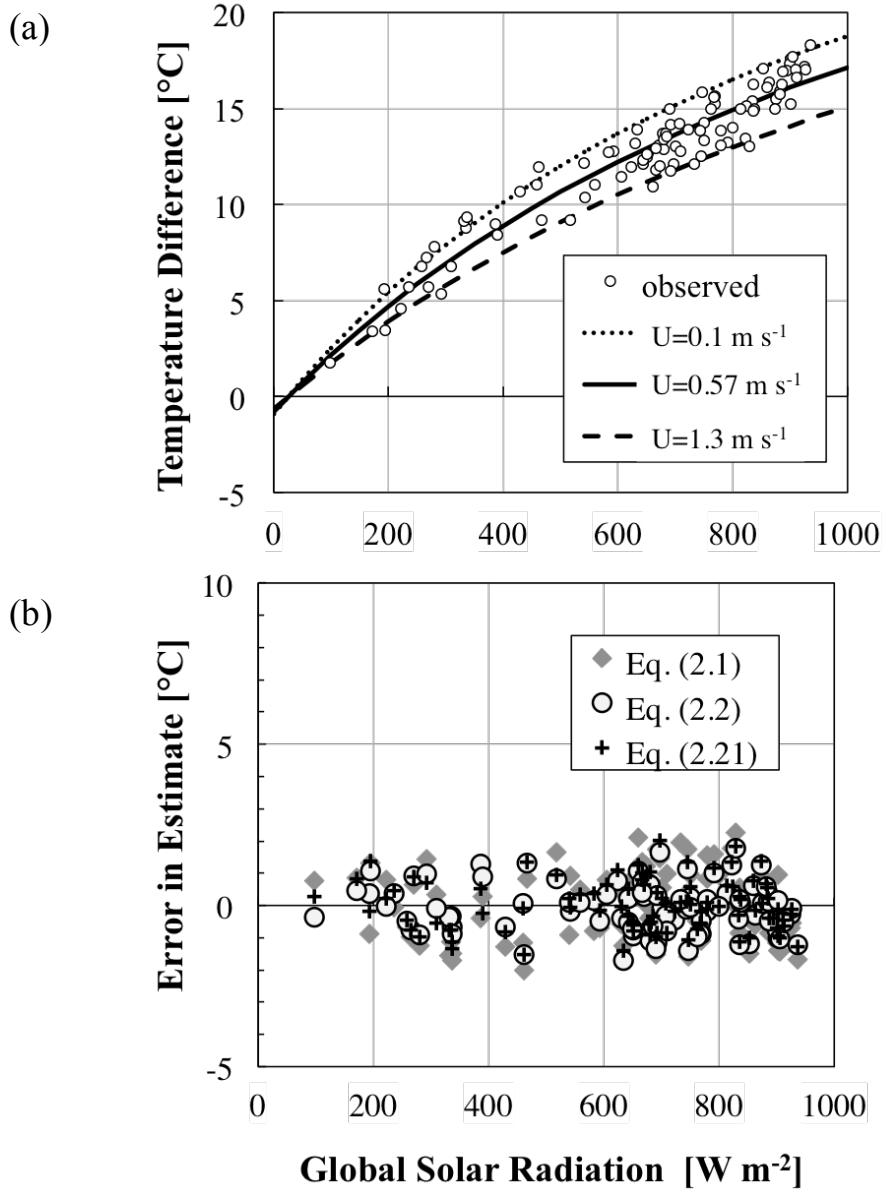
Fig. 2.13. (a) Dependence of the temperature difference, $T_g - T_a$, calculated from the new formula (**Eq. 2.21**) on global solar radiation together with the observed values. **Eq. 2.21** was plotted for a wind speed of 0.2, 0.57 and 1.3 m s^{-1}. (b) Errors in estimate [estimated T_g minus measured T_g] given by the three formulae. The diamond symbols indicate the error in estimate calculated from **Eq. 2.1** in **Table 2.1**, the circle symbols calculated from **Eq. 2.2** in **Table 2.1** and the cross symbols calculated from **Eq. 2.21**.
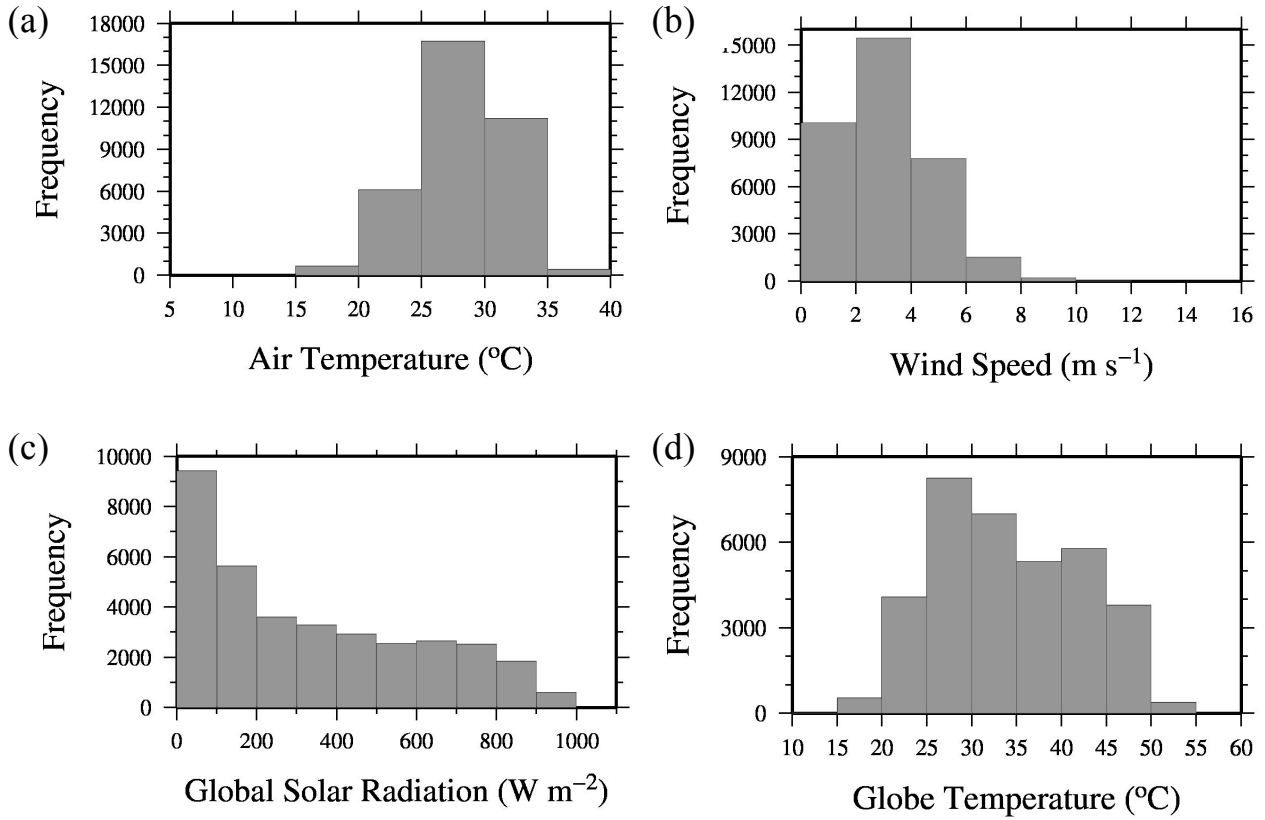
Fig. 2.14. Histogram of (a) air temperature, (b) wind speed, (c) global solar radiation and (d) globe temperature used to determine the numerical constants in **Eq. 2.22**. Air temperature, wind speed, and global solar radiation were obtained from Japan Meteorological Agency. Globe temperature was obtained from Japanese Ministry of the Environment. All data were collected hourly.
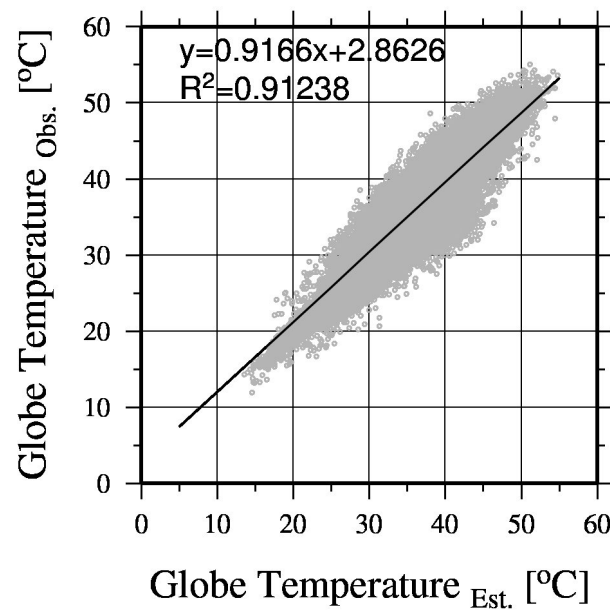
Fig. 2.15. Comparison of globe temperature estimated by **Eq. 2.22** to that observed. Globe temperature is estimated using the observed air temperature, solar radiation, and wind speed by **Eq. 2.22**.
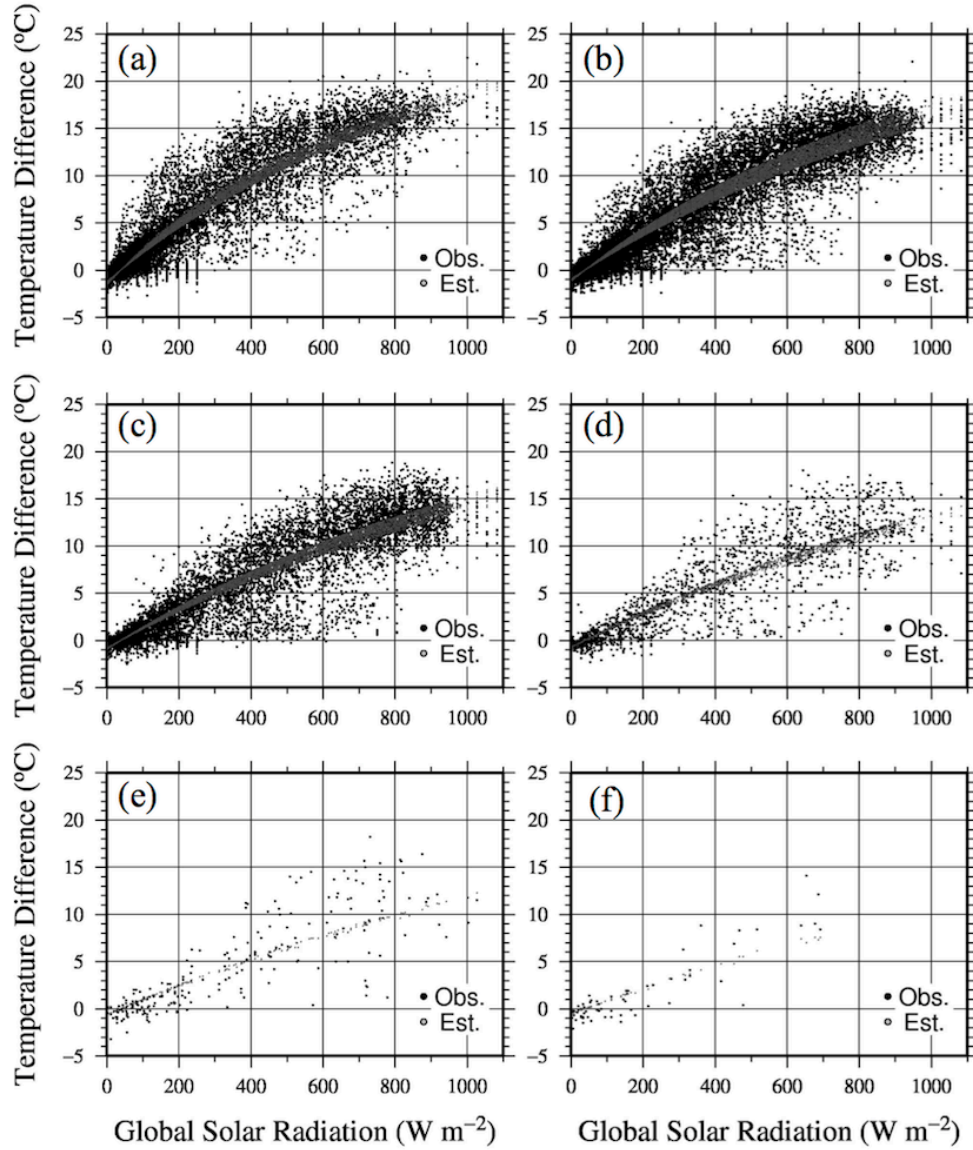
Fig. 2.16. Dependence of temperature difference, $T_g - T_a$, on global solar radiation in long-term observation data. (a) wind speed less than 2.0 m s^{-1}, (b)wind speed more than and equal to 2.0 m s^{-1} and less than 4.0 m s^{-1}, (c)wind speed more than and equal to 4.0 m s^{-1} and less than 6.0 m s^{-1}, (d) wind speed more than and equal to 6.0 m s^{-1} and less than 8.0 m s^{-1}, (e) wind speed more than and equal to 8.0 m s^{-1} and less than 10.0 m s^{-1}, (f) wind speed more than and equal to 10.0 m s^{-1}. Globe temperature, T_g, is estimated using the observed air temperature, solar radiation, and wind speed by **Eq. 2.22**.
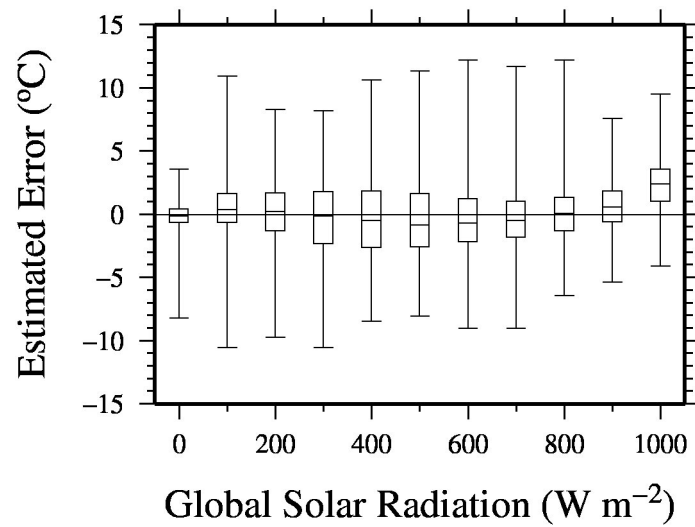
Fig. 2.17. Box plot of the estimated error (the values temperature that subtracted the observed globe temperature from the estimated one) for global solar radiation. Estimated globe temperature is estimated using the observed air temperature, solar radiation, and wind speed by **Eq. 2.22**. Upper and lower horizontal bar indicate the maximum and minimum values, respectively. Upper and lower sides of the box indicate 75 and 25 percentile values. Center horizontal bar inside the box indicate the median value.
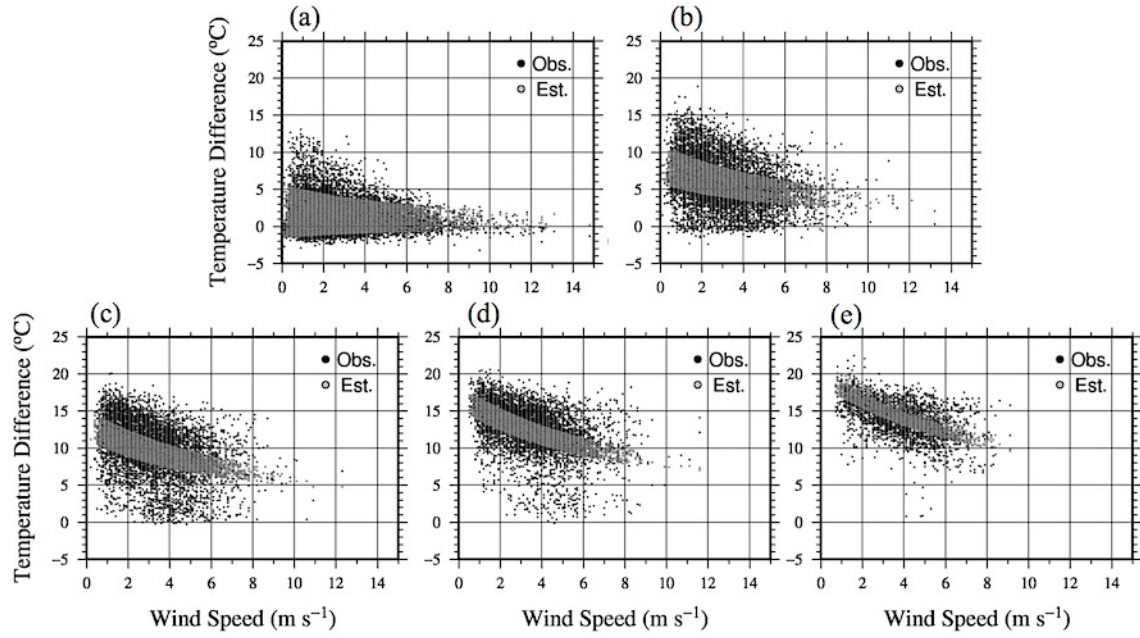
Fig. 2.18. Dependence of temperature difference, $T_g - T_a$, on wind speed in the long-term observation data. (a) global solar radiation less than 200 W m^{-2}, (b)wind speed more than and equal to 200 W m^{-2} and less than 400 W m^{-2}, (c)wind speed more than and equal to 400 W m^{-2} and less than 600 W m^{-2}, (d) wind speed more than and equal to 600 W m^{-2} and less than 800 W m^{-2}, (e) wind speed more than and equal to 800 W m^{-2}. Globe temperature, T_g, is estimated using the observed air temperature, solar radiation, and wind speed by **Eq. 2.22**.
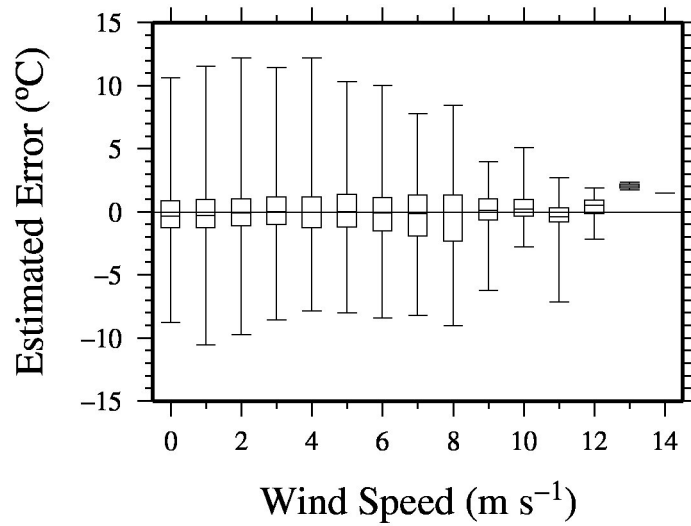
Fig. 2.19. Box plot of the estimated error (the values temperature that subtracted the observed globe temperature from the estimated one) for wind speed. Estimated globe temperature is estimated using the observed air temperature, solar radiation, and wind speed by **Eq. 2.22**. Upper and lower horizontal bar indicate the maximum and minimum values, respectively. Upper and lower sides of the box indicate 75 and 25 percentile values. Center horizontal bar inside the box indicate the median value.
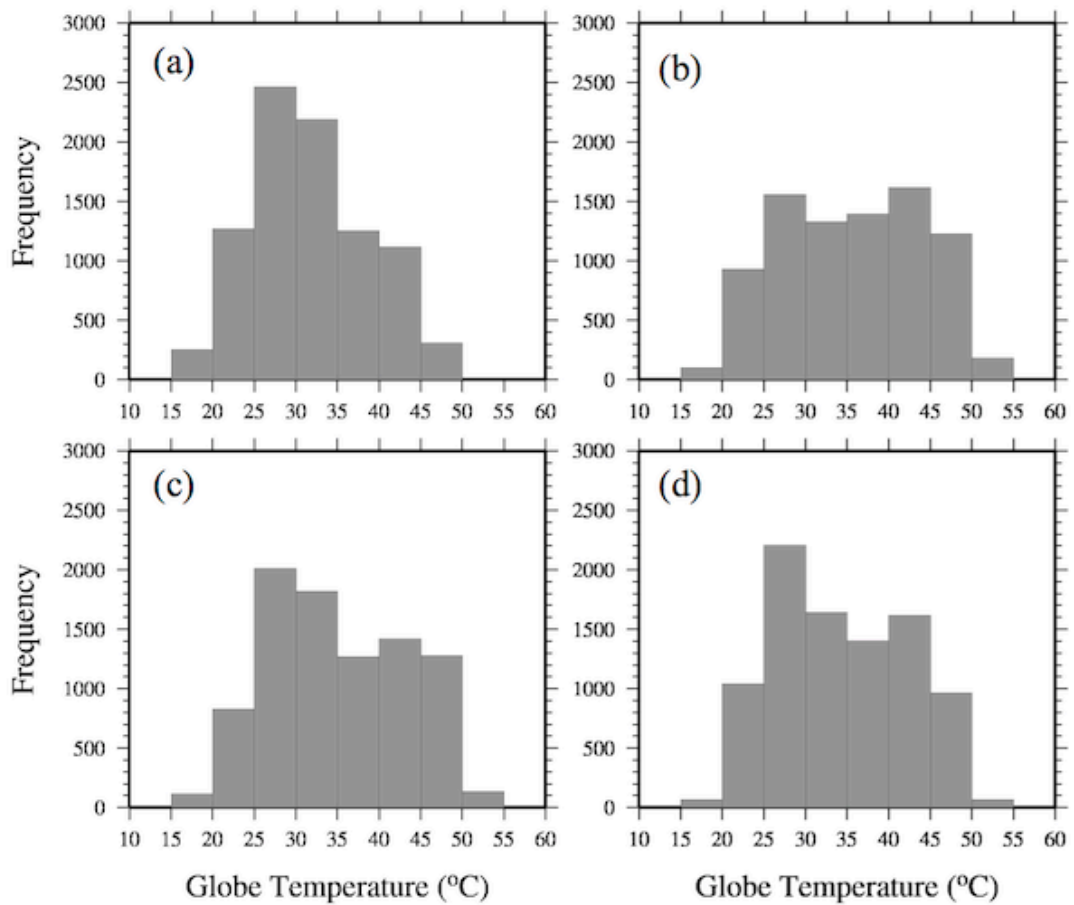
Fig. 2.20. Histogram of of globe temperature in Tokyo (a), Nagoya (b), Osaka (c), and Fukuoka (d). Globe temperature was measured using a Vernon type globe. The globe was placed at a height of 1.5m above the grass field in the meteorological station.
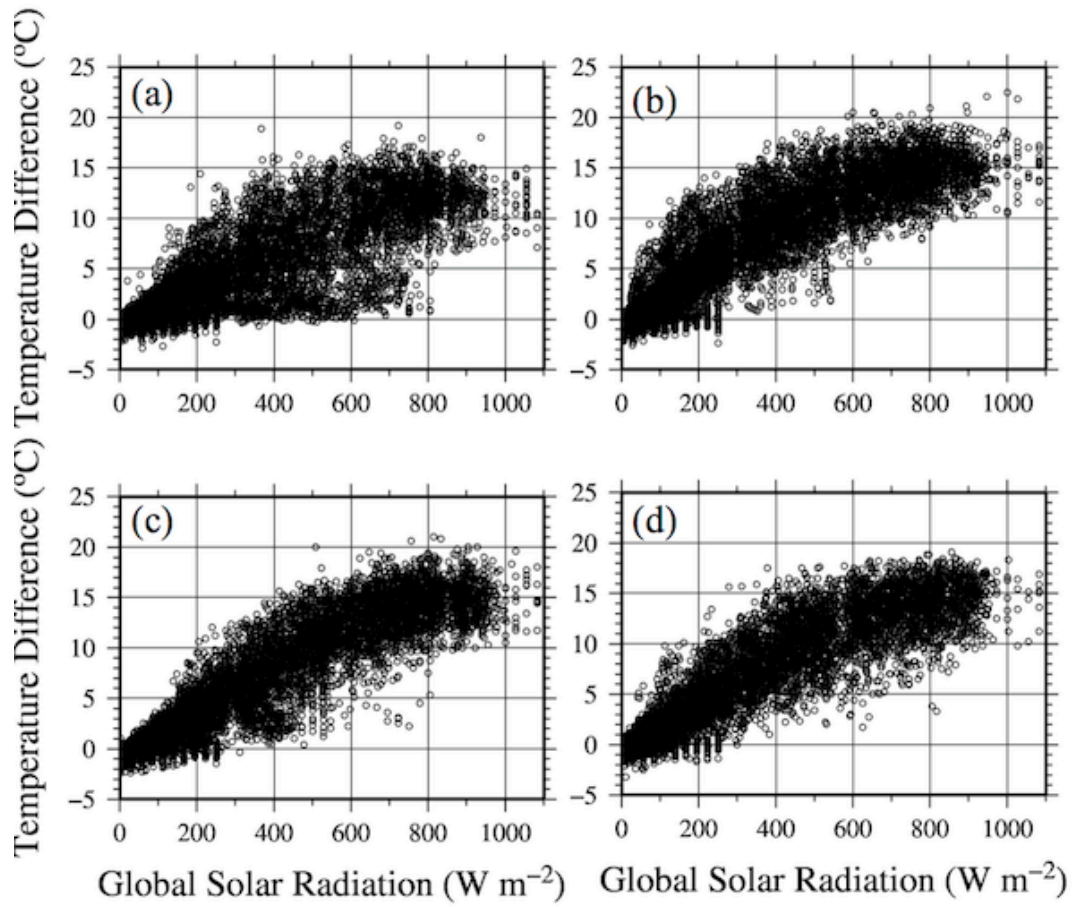
Fig. 2.21. Dependence of the temperature difference, T_g - T_a, on global solar radiation in Tokyo

(a), Nagoya (b), Osaka (c) and Fukuoka (d). Globe temperature, T_g, is estimated using the

observed air temperature, solar radiation, and wind speed by **Eq. 2.22**.
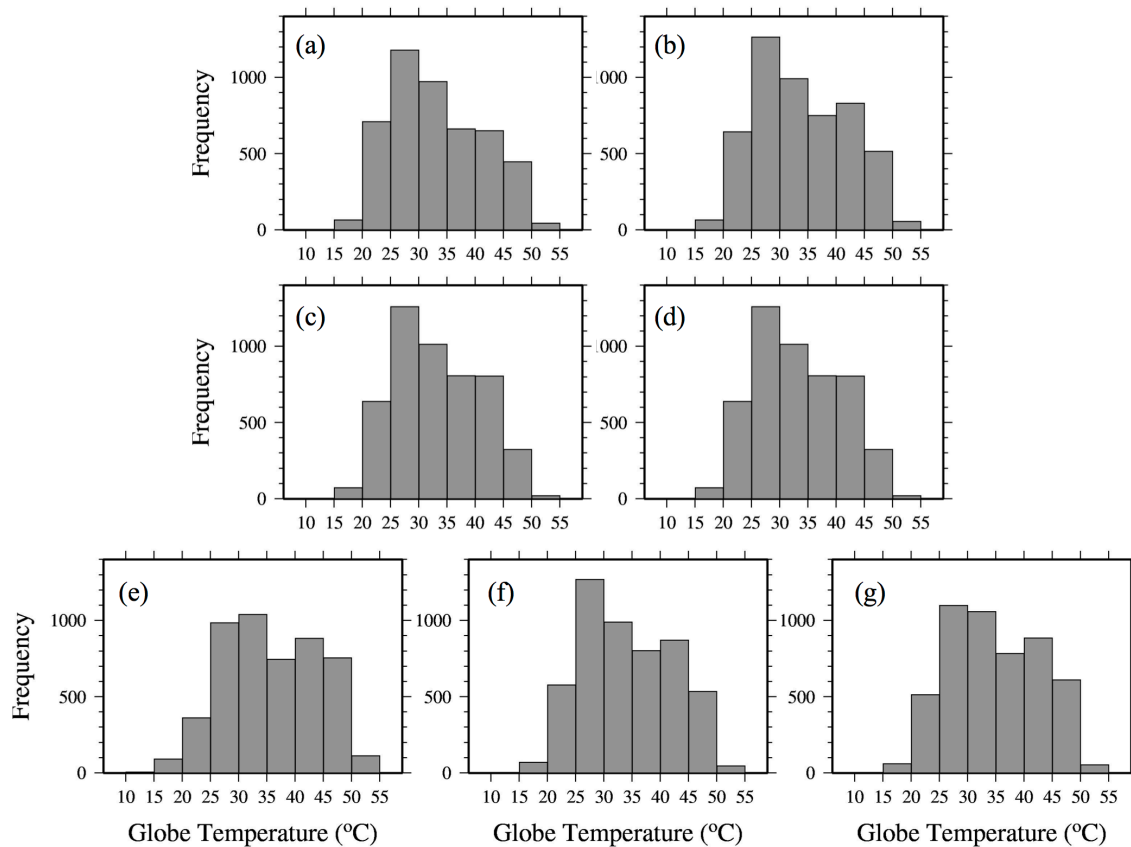
Fig. 2.22. Histogram of globe temperature in 2006 (a), 2007 (b), 2008 (c), 2009 (d), 2010 (e), 2011 (f) and 2012 (g). Globe temperature was measured using a Vernon type globe. The globe was placed at a height of 1.5m above the grass field in the meteorological station.

3. Development of the polyethylene chamber

3.1 Previous studies and objective

A wind tunnel is an effective tool to study convective heat transfer at vegetation surface. Hino and Kanda (1989) introduced the wind tunnel covered with acrylic panel to study the effects of evapotranspiration for cooling the atmosphere. Since the acrylic panel is transparent to shortwave (solar) radiation, the plants inside the tunnel receive shortwave radiation and are capable to transpire. Hence the plant surface temperature is lowered by transpiration. Contrary to shortwave radiation, the acrylic panel is opaque to longwave radiation. Hence, the plant temperature is not lowered under radiative cooling at night. Our interest of this study particularly lies on heat exchange process between the vegetation surface and its surrounding air in the nighttime. However, it is difficult to conduct a wind tunnel experiment for nocturnal heat exchange, and the satisfaction of similarity law during the nighttime is the hardest task. A ventilated chamber is also an effective tool to study transpiration from vegetation surface. Leuning and Foster (1990) used the ventilated chamber and determined the transpiration rate from single trees in the daytime. The heat balance analysis in the chamber could evaluate convective heat transfer without similarity law. However, the material used in most ventilated chamber, including in Leuning and Foster (1990), was opaque to longwave radiation so that the plant temperature is not lowered under radiative cooling at night. To solve this problem we propose and develop a new chamber "polyethylene (PE) chamber" using a thin PE film as a covering material of the chamber.

The PE chamber is expected to investigate heat exchange between the vegetation surface and its surrounding air especially in the nighttime. In this chapter, we introduce the design and

related heat balance about the PE chamber. Also, preliminary experiments are conducted to confirm the performance of the PE chamber.

3.2 Material and methods

3.2.1 Design and construction of the PE chamber

Figure 3.1 and **3.2** show a photo and a schematic drawing of the PE chamber, respectively. A wood board (1820mm long, 400mm wide and 20mm thick) was used as a chamber base. Two wood rails, made from 30-mm rectangular timber pieces, were fixed along the long axis of the base board at a distance of 300mm apart from each other. The 300mm wide gap between the rails was filled with 30-mm thick extruded polystyrene foam panel (Styrofoam) that served as a chamber floor. The chamber structure was constructed on the rails and was composed of three sections; an inlet section, a PE film cover section (hereafter referred to as the PE section) and an outlet section. An inverted U-shape wood frame, made from a 30-mm-thick rectangular timber piece, was installed between the three sections and at two ends as a support structure. The outer dimensions of the inlet and the outlet sections were 280mm (length), 360mm (width), and 180mm (height). Also, those of the PE section were 910mm (length), 360mm (width), and 180mm (height). The sidewalls and the ceiling of the inlet and outlet sections were shielded by a 30-mm-thick extruded polystyrene foam panel leaving a cross section of 300-mm-wide and 150-mm-high cross section for air space inside the sections. On the other hand, the cross section for air space inside the PE section was 300mm wide and 180mm high. The sidewalls of the PE section were also shielded by a 30-mm-thick extruded polystyrene foam panel. Also, its ceiling was covered with a 0.02-mm-thick PE film that is commercially available as the mulch cover of horticultural crops. The polystyrene floor surface was covered with a 0.23-mm-thick, black Kent

paper, while the polystyrene sidewall and the ceiling surface were covered with a 0.012-mm-thick aluminium foil commercially available as cooking foil. Since the aluminium foil used for the sidewall surface has high reflectivity to both shortwave and longwave radiation, the aluminium surface work as a mirror with respect to the radiation. If the radiation incident on the sidewalls is mirrored perfectly, we can assume that, as a result of reflection from sidewalls, the radiation incident on the floor of the PE section is similar to the one that would be incident on an infinitely large surface.

The end of the outlet section was closed by a 5.0-mm-thick plywood board, and an exhaust fan (MD625-B12; Oriental Motor, Tokyo, Japan) was installed at the center of the end board. Air was ventilated by the exhaust fan in the longitudinal direction from the inlet section to the outlet section. Polypropylene non-woven fabric with the ratio of the area of interstices of approximately 45% was installed at the air inlet side of the inlet section and between the PE and the outlet section to regulate the airflow. To prevent unfavourable effects of outdoor wind, two end sections outside the inlet and the outlet were covered with a wind shelter made from polystyrene panel when the experiment was conducted outdoors (**Fig. 3.3**).

Thin PE film is a unique plastic material that transmits both shortwave and longwave radiation. Because of this feature, PE has been widely used as a shield of a net radiometer (Funk 1959). Thin PE film is used as the ceiling of the PE section (**Fig. 3.2**). Thus, the radiative environment in the PE section is similar to that outdoors.

Generally, the chambers do not have the air inlet and outlet. In the PE chamber, on the other hand, the air in the chamber is ventilated along its long axis by the exhaust fan. Therefore, there is an air temperature difference between the inlet and the outlet of the chamber. Using this temperature difference and some other heat balance components of the PE chamber, we can

evaluate heat exchange in the chamber. The structure, which the air flows in the tunnel, is similar to that of a wind tunnel. However, we do not take into consideration the similarity law relevant to a scale model experiment in the PE chamber developed here.

3.2.2 Measurements

Figure 3.4 shows the measurement points for air temperature, surface temperature, and the temperature difference between the inside and the outside surfaces of the extruded polystyrene foam panel at the floor or the sidewall. Copper-constantan thermocouples ($\varphi = 0.32$mm) were used for the measurements. The thermocouple for incoming air temperature was placed 75mm above the floor surface at the center of the inlet section (**Fig. 3.5a**). In the nighttime, temperature stratification developed when air passed through the PE section. Therefore, the outgoing air temperature was spatially non-uniform even at the position of the exhaust fan; e.g., the temperature was lower below the fan center and higher above it under cooling conditions at night. To obtain the average temperature of outgoing air, we used four copper-constantan thermocouples; each was placed at the left, right, top, and bottom of the windward cross section of the exhaust fan (**Fig. 3.5b**).

Four thermocouples were used for the floor surface temperature measurements (**Fig. 3.4a**, **3.5c**). The temperature difference between the inside and the outside surfaces of the extruded polystyrene foam panel at the floor or the sidewall was measured using a thermocouple to calculate conductive heat flux through the sidewalls and the floor (**Fig. 3.4b**, **3.5d**). All of the sensing junctions were connected to one common reference junction to minimize possible instrumental errors arising when individual separate thermocouples are used (**Fig. 3.3**).

Figure 3.6 shows a view of the outdoor experiment using the PE chamber. The outdoor

experiments were conducted on the building's roof because there were fewer objects preventing the nocturnal radiative cooling. The PE chamber was elevated at a height of 300mm above the building's roof using the plastic box. Net radiation was measured using a net radiometer (Q7, Radiation and Energy Balance Systems, Inc., Seattle, United States). Ventilating to the sensor of a net radiometer with the ventilator reduces the measurement error. However, setting the ventilator near the film might change locally the film surface temperature. This change of the film surface temperature results in the lack of the representative of the film surface temperature. Therefore, the ventilator of the net radiometer was not used in this study. The measurement error of a net radiometer changes with wind speeds, and its wind effect results in a reduction in the calculated net radiation with increasing wind speeds. This reduction during positive net flux conditions increases asymptotically from 0% at a wind speed of 0.0 m s^{-1} to approximately +5.9% at 7.0 m s^{-1}. The reduction during negative net flux conditions changes from -0.4% at a wind speed of 0.5 m s^{-1} to 1.0% at 7.0 m s^{-1}. In the outdoor experiment, a net radiometer was mainly placed next to the PE chamber and measured net radiation above the PE film (**Fig. 3.6**). All the sensor signals as well as the reference temperatures of the thermocouples were collected using a datalogger (CR-1000, Campbell Scientific, Logan, USA) with a sampling interval of 1 sec and an averaging interval of 1 min for recording data.

3.2.3 Wind speed and ventilation rate of the PE chamber

Before the experiment, we need to know wind speed inside the chamber. A non-directional hot wire anemometer (Hon Field Monitor Type SL-400, Honda Dynamics, Osaka, Japan) was used to measure wind speed inside the chamber. The measurement error of the hot wire anemometer is 2% of the full-scale for measurement. Since the full-scale of the hot wire

anemometer used in this section was 0.5 m s^{-1}, the measurement error of the hot wire anemometer was approximately 0.01 m s^{-1}. The anemometer was inserted horizontally into the chamber through the holes made on the sidewall panel (**Fig. 3.7a**). The sidewall panel with holes was used only when the wind speed inside the chamber was measured indoors. **Figure 3.7b** shows the cross-sectional wind speed profile at the center of the PE section. The measurement points of wind speed were segmented in the cross-section of the center of the PE section. Wind speed at each measured point ranged from 0.19 m s^{-1} to 0.25 m s^{-1}, and the wind speed averaged over fifteen points was 0.21 m s^{-1}. Two rather large values were obtained at the left side of the figure near the wall. These values might overestimate the real wind speed, because the reference temperature sensor of the anemometer was located close to the sidewall so that it did not reflect the air temperature accurately when those points were measured.

We need to determine the ventilation rate to calculate heat flux transported by ventilation. The air exhaust rate of the fan under working condition was estimated from the following observation. A 12.5-m-long flexible polyethylene tube of diameter 630mm was inflated by blowing the air exhausted from the fan. The tube, deflated in the beginning of the process, was promptly attached to the fan outlet and became inflated (**Fig. 3.8**). An air exhaust rate was calculated from the volume of the inflated tube and the time taken for full inflation. The ventilation rate thus estimated was 0.0074±0.0001 m^3 s^{-1}.

3.2.4 Longwave radiation characteristics of the materials used in the PE chamber

The emissivity of aluminium foil and black Kent paper was measured using an emission meter (Emissiometer AE1 RD1, Devices and Services Co., Dallas, USA) and its values were 0.02 and 0.89 for aluminium foil and black Kent paper, respectively. Unlike aluminium foil or

black Kent paper, a PE film is transparent to longwave radiation; thus, we need to know the emissivity, reflectivity and transmissivity. Okada (1983) introduced a method to measure the infrared properties of plastic films by a commercial emissivity measuring instrument. Using their method combined with a commercial emission meter (TSS-5X, Japan Sensor Cooperation, Tokyo, Japan), we measured and obtained a transmissivity of 0.85, reflectivity of 0.11, and emissivity of 0.04 for the PE film used in this study.

3.2.5 Heating experiment

A key point related to the PE chamber device is how accurately the convective heat flux generated at the surface inside the PE section can be evaluated from the inlet-outlet air temperature difference and some other heat balance components. As the first step toward the examination of the chamber performance, we installed a 2-m-long heating cable suspended approximately 70mm above the floor of the PE section (**Fig. 3.9**). Two chambers were used for the measurement and the heater was repeatedly switched at intervals of 30 min. The chambers were placed inside a calm room. The output of the cable heater was evaluated from the electronic current and voltage, and the resulting value was 23W.

3.2.6 Relationship between the net radiation inside and outside of the PE chamber

The outdoor experiment for nocturnal radiation balance measurement was conducted on the building's roof at the Faculty of Agriculture, Iwate University, Morioka, Japan (39°42'N, 141°8'E) on February 28th, 2013 with clear night sky. The chambers were placed on the building's roof at night, exposed to the sky for the radiation to take place (**Fig. 3.10a**). Also, the daytime outdoor experiment for radiation balance measurement was conducted on the building's

roof at Graduate School of Life and Environment Sciences, the University of Tsukuba, Japan (36.87°N, 141.7°E) on July 27th, 2013 with cloudy weather. The chambers were placed on the grass of the building's roof (**Fig. 3.10b**).

Two sets of the net radiometers were prepared to evaluate the extent to which the net radiation inside the chamber is reduced by a PE film, compared to the outside radiation. One of the radiometers was set above the PE section, while another one was set under the PE cover inside the PE section (**Fig. 3.10**). The inside radiometer was inserted from the air inlet of the chamber and was inserted to avoid colliding with the inside surfaces of the chamber (**Fig. 3.10c**). The non-woven fabric, installed at the air inlet, was temporarily removed during the radiation measurements. The data averaged over a 10-min-long sampling period were collected when the transit change of the net radiometer signal was considered to disappear 3 min after the instrument was settled.

To minimize the error between two net radiometers, a net radiometer was needed to correct to match another one. Therefore, two radiometers were compared by placing them next to each other on the building's roof. The model numbers of the net radiometers were different in the experiments in Iwate University and in the University of Tsukuba. Thus, the outdoor experiments were conducted in each measurement place to correct the error between two net radiometers (**Table 3.1**). The correction coefficient of the net radiometers shows the positive and negative values in the daytime and nighttime, respectively. Therefore, the correction experiments were distributed and conducted in the daytime and nighttime (**Table 3.1**). We first selected the standard net radiometer from one of the two net radiometers. Then, the correction coefficient of a net radiometer was reevaluated by averaging the net radiation proportion of a net radiometer to the standard one. **Figure 3.11** shows the correlation of net radiation between two sets of net

radiometer after the correction experiment. Each regression lines corresponded well to the line of $y = x$. The average error concentrated around 0.0 W m^{-2}, and root mean square errors in each experiment were small; 0.38 W m^{-2}, 0.04 W m^{-2} and 2.13 W m^{-2}, respectively (**Table3.1**).

3.3 Heat balance of the PE chamber

A structure that was similar to the PE chamber has been used as a temperature gradient chamber (hereafter referred to as TGC) to investigate plant responses to temperature (e.g., Rawson et al. 1995; Horie et al. 1995; Kim et al. 1996; Lee et al. 2001). For a TGC, Okada et al. (1995) introduced a simple heat balance equation to show the relationship between the inlet-outlet air temperature difference and solar heat gain or supplemental heat from heating devices. In their equation, heat transfer due to longwave radiation was included in the heat transmission term through a covering film together with convection at the film surface. This is because a large temperature difference was induced by solar heat gain during the daytime or by supplemental heat during the nighttime; thus, longwave radiation had only weakly contributed to the temperature difference in the TGC. Contrary to a TGC, the temperature difference between the inlet and outlet air in the PE chamber is as small as 1.0°C or less, particularly at night, so that small changes in radiation balance, including longwave radiation, are critical in our chamber study. Furthermore, the longwave radiation properties of the covering film are different between the TGC and the PE chamber; the transmissivity of a polyvinylchloride film used for the TGC was much smaller than that of the PE film. Therefore, in the sections that follow, we first describe the radiation balance of the PE chamber and then discuss the heat balance.

3.3.1 Radiation balance of the PE chamber

If the PE film is perfectly transparent to radiation, there should be no difference between the levels of net radiation above and below the film. The net radiation, however, should be different when measured above and below the film when the radiation is partially absorbed by the PE film. In the following sections, we assumed two very large surfaces of film and floor that are facing, and parallel to, each other. Thus, the radiation is exchanged one-dimensionally. These conditions could be simulated when the radiation was strongly reflected from the aluminium surfaces of the sidewalls.

In the following, the subscripts were defined as below:

About shortwave or longwave radiation; The subscript on the left side of hyphen indicate the heat exchange surface (above the PE film: a, below the PE film: b, floor: f, PE film: p, sky: *sky*). The subscript on the right side of hyphen indicate the direction of shortwave radiation (downward: *down*, upward: *up*). Asterisk indicate net radiation.

About radiative characteristics; The first subscript indicate the radiation's type (shortwave: s, longwave: l), the second subscript indicate the heat exchange surface (floor: f, Kent paper: k, polyethylene film: p), and the third subscript indicate the direction of shortwave radiation (downward: *down*, upward: *up*). The radiative characteristics for longwave radiation do not have the third subscript.

Radiative characteristics of the PE film, in particular its reflectivity, depend largely on the incident angle of radiation. The downward radiation incident on the outside film surface from the sun and the sky consists of direct beams and scattered radiation, whereas the upward radiation incident on the inside film surface usually consists of scattered radiation unless the floor surface is shiny. The characteristics are different for different directions of radiation; therefore, we

define transmissivity, reflectivity and absorptivity separately for downward and upward radiations (**Fig. 3.12**). The sum of absorptivity, reflectivity and transmissivity for each direction are written as below:

$$a_{s-p-down} + r_{s-p-down} + t_{s-p-down} = 1 \qquad (3.1)$$

$$a_{s-p-up} + r_{s-p-up} + t_{s-p-up} = 1 \qquad (3.2)$$

where $a_{s-p-down}$ is absorptivity of the PE film for downward shortwave radiation. $r_{s-p-down}$ is reflectivity of the PE film for downward shortwave radiation. $t_{s-p-down}$ is transimissivity of the PE film for downward shortwave radiation. a_{s-p-up} is absorptivity of the PE film for upward shortwave radiation. r_{s-p-up} is reflectivity of the PE film for upward shortwave radiation. t_{s-p-up} is transimissivity of the PE film for upward shortwave radiation.

Since floor surface is not transparent, the sum of absorptivity and reflectivity is unity; namely,

$$a_{s-f-down} + r_{s-f-down} = 1 \qquad (3.3)$$

where $a_{s-f-down}$ is absorptivity of the floor for downward shortwave radiation, and $r_{s-f-down}$ is reflectivity of the floor for downward shortwave radiation.

Figure 3.13 shows shortwave radiation balance inside and outside the chamber. Net shortwave radiation above and below the PE film S^{*}_{a} and S^{*}_{b} is given by **Eqs. 3.4** and **3.5**, respectively, by defining S as the outdoor shortwave radiation, S_{p-up} as the shortwave radiation at

the outside film surface directed upward, and $S_{p\text{-}down}$ as the shortwave radiation at the inside film

surface directed downward:

$$S_a^* = S - S_{p-up} \qquad (3.4)$$

$$S_b^* = S_{p-down} - S_{f-up} \qquad (3.5)$$

Upward directed shortwave radiation at the floor surface, $S_{f\text{-}up}$ is equal to the radiation

reflected by the floor surface (**Eq. 3.6**).

$$S_{f-up} = r_{s-f} S_{p-down} \qquad (3.6)$$

Shortwave radiation at the outside film surface directed upward, $S_{p\text{-}up}$, is expressed as the

sum of outdoor shortwave radiation, S, reflected by the upside of the PE film and upward

directed shortwave radiation at the floor surface, $S_{f\text{-}up}$, transmitted by the PE film (**Eq. 3.7**).

Shortwave radiation at the inside film surface directed downward, $S_{p\text{-}down}$, is expressed as the

sum of outdoor shortwave radiation, S, transmitted by the PE film and upward directed

shortwave radiation at the floor surface, $S_{f\text{-}up}$, reflected by the lower surface of the PE film (**Eq.**

3.8).

$$S_{p-up} = r_{s-down} S + t_{s-up} S_{f-up} \qquad (3.7)$$

$$S_{p-down} = t_{s-down} S + r_{s-up} S_{f-up} \qquad (3.8)$$

72

Substituting **Eqs. 3.7** and **3.8** into **Eqs. 3.4** and **3.5**, we obtain:

$$S_a^* = S - r_{s-p-down}S - t_{s-p-up}S_{f-up} \tag{3.9}$$

$$S_b^* = t_{s-down}S + r_{s-up}S_{f-up} - S_{f-up} \tag{3.10}$$

The difference between net shortwave radiation above and below the PE film is obtained by subtracting **Eq. 3.10** from **Eq. 3.9**:

$$\begin{aligned} S_a^* - S_b^* &= \left(1 - r_{s-p-down} - t_{s-p-down}\right)S - \left(1 - r_{s-p-up} - t_{s-p-up}\right)S_{f-up} \\ &= a_{s-p-down}S - a_{s-p-up}S_{f-up} \end{aligned} \tag{3.11}$$

Outdoor global shortwave radiation, S, is significantly larger than upward shortwave radiation at the floor surface, S_{f-up} ($S \gg S_{f-up}$). Therefore, net shortwave radiation below the PE film (inside the chamber) is reduced and the extent of reduction depends on outdoor shortwave radiation and the absorptivity of PE film for incoming shortwave radiation. The absorptivity of a transparent PE film is 5% or less when the film is as thin as 20μm.

Thin PE films are also transparent well to longwave radiation. As with shortwave radiation, thus, the sum of absorptivity, reflectivity and transmissivity is unity:

$$a_{l-p} + r_{l-p} + t_{l-p} = 1 \tag{3.12}$$

$$a_{l-f} + r_{l-f} = 1 \tag{3.13}$$

73

where a_{l-p} is absorptivity of the PE film for longwave radiation. r_{l-p} is reflectivity of the PE film for longwave radiation. t_{l-p} is transimissivity of the PE film for longwave radiation. a_{l-f} is absorptivity of the floor surface for longwave radiation. r_{l-f} is reflectivity of the floor surface for longwave radiation. Note that for longwave radiation, the absorptivity is considered to be identical to the emissivity.

Figure 3.14 shows longwave radiation balance inside and outside the chamber. The net longwave radiation flux density above and below the PE film (L^*_a and L^*_b) is given by **Eqs. 3.14** and **3.15**, respectively, by defining L_{p-up} as the longwave radiation flux density directed upward at the outside film surface, L_{p-down} as the longwave radiation flux density directed downward at the inside film surface, and L_{f-up} as the longwave radiation flux density directed upward at the floor surface:

$$L^*_a = L_{sky} - L_{p-up} \tag{3.14}$$

$$L^*_b = L_{p-down} - L_{f-up} \tag{3.15}$$

L_{f-up} is given by the sum of the longwave radiation emitted from and reflected by the floor surface (**Eq. 3.16**).

$$L_{f-up} = \varepsilon_f \sigma T_f^4 + r_{l-f} L_{p-down} \tag{3.16}$$

The upward longwave radiation flux density at the PE film surface, L_{p-up}, is expressed as the

sum of the longwave radiation emitted going upward from the PE film, $\varepsilon_p \sigma T_p^4$, the longwave radiation transmitted through the PE film, $t_{l\text{-}p}L_{f\text{-}up}$, and the sky longwave radiation reflected by the PE film, $r_{l\text{-}p}L_{sky}$ (**Eq. 3.17**). The downward longwave radiation flux density at the PE film surface, $L_{p\text{-}down}$, is expressed as the sum of the longwave radiation emitted going downward from the PE film, $\varepsilon_p \sigma T_p^4$, the sky longwave radiation transmitted through the PE film, $t_{l\text{-}p}L_{sky}$, and the longwave radiation reflected by the PE film, $r_{l\text{-}p}L_{f\text{-}up}$ (**Eq. 3.18**).

$$L_{p-up} = \varepsilon_p \sigma T_p^4 + t_{l-p}L_{f-up} + r_{l-p}L_{sky} \tag{3.17}$$

$$L_{p-down} = \varepsilon_p \sigma T_p^4 + t_{l-p}L_{sky} + r_{l-p}L_{f-up} \tag{3.18}$$

Substituting **Eqs. 3.17** and **3.18** into **Eqs. 3.14** and **3.15**, we obtain:

$$L_a^* = L_{sky} - \varepsilon_p \sigma T_p^4 - t_{l-p}L_{f-up} - r_{l-p}L_{sky} \tag{3.19}$$

$$L_b^* = \varepsilon_p \sigma T_p^4 + t_{l-p}L_{sky} + r_{l-p}L_{f-up} - L_{f-up} \tag{3.20}$$

The difference between the net longwave radiation flux densities above and below the PE film is given by subtracting **Eq. 3.20** from **Eq. 3.19**:

$$
\begin{aligned}
L_a^* - L_b^* &= \left(1 - r_{l-p} - t_{l-p}\right)L_{sky} + \left(1 - r_{l-p} - t_{l-p}\right)L_{f-up} - 2\varepsilon_p \sigma T_p^4 \\
&= \varepsilon_p \left(L_{sky} + L_{f-up} - 2\varepsilon_p \sigma T_p^4\right)
\end{aligned}
\tag{3.21}
$$

Suppose that the floor surface of the chamber is cooled by radiation in the nighttime. Then,

the term σT_p^4 is larger than the sky radiation term L_{sky} and the floor radiation term L_{f-up}, because both the sky and the floor surface temperature are usually lower than the PE film temperature. Note that the PE film negligibly cooled by the radiation because its emissivity is small. Hence, **Eq. 3.21** is usually negative, indicating that nocturnal radiative cooling is reduced below the PE film (inside the chamber). The degree of reduction, however, is small when the emissivity of the film ε_p is small. Similarly, the floor surface of the chamber is heated by solar radiation in the daytime. Then, the term σT_p^4 and the floor radiation term L_{f-up} are larger than the sky radiation term L_{sky}, because both the PE film temperature and the floor surface temperature are usually higher than the sky temperature. Hence, the difference between the radiation term emitted from the PE film and the floor radiation term determines a positive or a negative of **Eq. 3.21**.

Equations 3.19 and **3.20** give an important solution that enables to perform the estimation of the net longwave radiation inside the chamber. It is easy to install a net radiometer above the PE film, but it is often difficult to install it inside because of the limitation in space, particularly when black Kent papers are constructed in the chamber. When the net radiation above the PE film, L^*_a, the PE film surface temperature, T_p, and the floor surface temperature, T_f, are known, the longwave sky radiation, L_{sky}, and the net radiation below the PE film, L^*_b, are calculated by solving **Eqs. 3.16** through **3.20** simultaneously, as well as the upward longwave radiation at the floor surface, L_{f-up}.

In the following, we describe how to calculate L_{sky} and L^*_b by solving **Eqs. 3.16** through **3.20** simultaneously. First, L_{f-up} is expressed as substituting **Eq. 3.18** into **Eq. 3.16** as below:

$$L_{f-up} = \varepsilon_f \sigma T_f^4 + r_{l-f}\left(\varepsilon_p \sigma T_p^4 + t_{l-p}L_{sky} + r_{l-p}L_{f-up}\right) \qquad (3.22)$$

Eq. 3.22 is transformed as follows:

$$L_{f-up} = \left(\varepsilon_f \sigma T_f^4 + r_{l-f}\varepsilon_p \sigma T_p^4 + r_{l-f}t_{l-p}L_{sky}\right)\Big/\left(1 - r_{l-f}r_{l-p}\right) \tag{3.23}$$

Substituting **Eq. 3.23** into **Eq. 3.19**, we obtain:

$$L_a^* = \left(1 - r_{l-p} - \frac{r_{l-f}t_{l-p}^2}{1 - r_{l-f}r_{l-p}}\right)L_{sky} - \left(\varepsilon_p + \frac{t_{l-p}r_{l-f}\varepsilon_p}{1 - r_{l-f}r_{l-p}}\right)\sigma T_p^4 - \frac{t_{l-p}\varepsilon_f}{1 - r_{l-f}r_{l-p}}\sigma T_f^4 \tag{3.24}$$

When L_a^*, T_p and T_f, are known, L_{sky} is given from **Eq. 3.24**. Hence, Then, L_{sky} is obtained as a residual of radiation balance equation in the PE chamber. Then, L_b^* is also given from **Eq. 3.20**. Here, the quantities L_a^* and T_f are measurable, but it is difficult to measure T_p accurately because PE is transparent to longwave radiation. Sticking a non-transparent temperature sensor to a point on the PE film surface will disturb the temperature at that point and the thermography technique is not effective on a transparent material. We can therefore use an average of the inside and the outside air temperatures. The average is usually a good estimate of T_p, because the temperature of the PE film is less affected by radiation and is balanced by convection at the inside and outside surfaces.

3.3.2 Heat balance of the PE chamber

In the outdoor experiment, we will examine the dependency of convective heat exchange on the vegetation morphology (see the chapter 4). In this study, a black Kent paper is used instead of a real leaf. Heat exchange occurs at the surface of a black Kent paper like a real leaf because

heat capacities of a paper and a leaf are negligibly small. In this section, we discussed the heat balance in the chamber with and without a black Kent paper.

First, heat balance of the PE chamber without a black Kent paper is discussed in the following paragraphs. Note that in the present section, the heat transfer components are expressed as a flux on a total area basis, whereas in the previous section, the components in radiation balance were expressed as a flux density on a unit area basis.

In the following, the subscripts of fluxes, Q, were defined as: the subscript on the left side of hyphen indicate the heat exchange type (convection: c, conduction: g, radiation: r), The subscript on the right side of hyphen indicate the heat exchange surface (above the PE film: a, below the PE film: b, floor: f, paper: k, PE film: p, sidewall: w). Asterisk indicates net flux.

Also, in the following, we assumed as below:

1) Evaporation nor condensation of water occurred at the surfaces in the chamber were not considered.

2) Heat capacity of the chamber materials were negligibly small; thus, we considered a steady state heat transfer.

3) Radiative cooling of the air was negligibly small.

4) The chamber was elevated on the ground surface; thus, we could consider that there was the insulating layer under the chamber.

5) There was not the temperature stratification in the chamber.

The net radiation flux at the floor surface, Q^*_{r-f}, is equivalent to the net radiation flux below the PE film, Q^*_{r-b}, and is expressed as,

$$Q^*_{r-f} = Q^*_{r-b} = A_f L^*_b \qquad (3.25)$$

where A_f is the area of the floor surface, L^*_b is the net radiation below the PE film.

The heat balance of net radiation, convection with inside air and conduction at the floor surface is given by **Eq. 3.26**:

$$Q^*_{r-f} = Q_{c-f} + Q_{g-f}$$

(3.26)

where Q_{c-f} is convective heat flux at the floor surface, Q_{g-f} is conductive heat flux through the floor. **Equation 3.26** gives an approach to evaluate the convective heat flux, Q_{c-f}, when the values of Q^*_{r-f} and Q_{g-f} are known. This equation is also valid at an outdoor ground surface, which is not covered with the film.

Figure 3.15 shows the schematic of heat balance of a volume. The sidewall surface is covered with aluminium foil. Thus, the radiative heat flux at the sidewall surface could be assumed to be negligibly small. Temporal change of air temperature inside the chamber, $\rho c_p (\partial T_a / \partial t)$, is divided into five heat balance components (**Eq. 3.27**).

$$\rho c_p \frac{\partial T_a}{\partial t} = -Q_{c-f} + Q_v + Q_p + Q_{g-w} + Q_{r-a}$$

(3.27)

where Q_v is heat flux due to ventilation, Q_p is heat transmission flux through the PE film, Q_{g-w} is conductive heat flux through sidewalls and Q_{r-a} is radiative cooling of the air. By the assumption 2, temporal change is neglected ($\rho c_p (\partial T_a / \partial t)=0$). By the assumption 3, the radiative cooling of the air is negligibly small ($Q_{r-a}=0$). Hence, the convective heat flux transferred from the floor

surface to the inside air is distributed into Q_v, Q_p and Q_{g-w} (**Eq. 3.28**).

$$Q_{c-f} = Q_v + Q_p + Q_{g-w} \tag{3.28}$$

Equation 3.28 offers an approach, unique to the PE chamber, to evaluate the convective heat flux, Q_{c-f}, when the values of Q_v, Q_p and Q_{g-w} are known. Substituting **Eq. 3.28** into **Eq. 3.26** gives the heat balance of the chamber that only has floor surface but no black Kent papers (**Eq. 3.29**).

$$Q^*_{r-f} = Q_v + Q_p + Q_{g-w} + Q_{g-f} \tag{3.29}$$

Figure 3.16a shows the schematic of the heat balance equation (**Eq. 3.29**). In **Fig. 3.16**, conductive heat flux through the sidewall, Q_{g-w}, is omitted because the projection is the elevation.

The conductive heat components, Q_{g-w} and Q_{g-f} are calculated from the following equations with the temperature difference between the inside and the outside surface of the sidewall ΔT_w or floor panel ΔT_f, the heat conductivity λ and the thickness d of extruded polystyrene foam panel:

$$Q_{g-w} = A_w \frac{\lambda}{d} \Delta T_w \tag{3.30}$$

$$Q_{g-f} = A_f \frac{\lambda}{d} \Delta T_f \tag{3.31}$$

The heat flux due to ventilation, Q_v, is calculated from **Eq. 3.32** with the air temperature

80

difference between the inlet and the outlet of the chamber, ΔT_a, and the ventilation rate, V.

$$Q_v = \rho c_p V \Delta T_a \qquad (3.32)$$

When the net radiation at the floor surface, $Q^*_{r\text{-}f}$, is directly measured or estimated from outside net radiation using the radiation balance equations described in the previous section and the conductive heat flux at the floor, $Q_{g\text{-}f}$, is calculated from **Eq. 3.31**, the convective heat flux at the floor surface, $Q_{c\text{-}f}$, is obtained from **Eq. 3.26**. Alternatively, $Q_{c\text{-}f}$ can be calculated from **Eq. 3.28**.

In this study, the heat transfer through the PE film is considered as the heat transmission. The heat transmission is often used in the architecture or agricultural meteorology field. **Fig. 3.17** shows the heat transfer of inside and outside of the plastic film in the chamber. Radiative heat, $Q_{r\text{-}in}$, and convective heat, $Q_{c\text{-}in}$, are transferred from the inside of the chamber to the surface inside of the plastic film. This total heat is transferred through the plastic film as the conductive heat, $Q_{g\text{-}p}$. At the surface outside of the plastic film, $Q_{g\text{-}p}$ is divided into radiative heat, $Q_{r\text{-}out}$, and convective heat, $Q_{c\text{-}out}$. Since net heat at each surface must correspond in the steady state, heat balance of the plastic film is expressed as,

$$Q_{r-in} + Q_{c-in} = Q_{g-p} \qquad (3.33a)$$

$$Q_{g-p} = Q_{r-out} + Q_{c-out} \qquad (3.33b)$$

Since it is difficult to measure surface temperature inside and outside of the plastic film, heat

81

transfer from the inside to the outside of chamber is considered together as heat transmission through a plastic film, Q_p. In general, Q_p is defined to be proportional to the inside and the outside air temperature difference as below,

$$Q_p = A_p h_t \left(T_{in} - T_{out} \right) \tag{3.34}$$

where A_p is the area of the PE film cover. h_t is heat transmission coefficient. T_{in} and T_{out} are air temperature inside and outside of the chamber, respectively.

$Q_{r\text{-}in}$ and $Q_{r\text{-}out}$ in **Eq. 3.33** are often expressed by the linearization of temperature and radiative heat transfer coefficient (Kimura 1970):

$$Q_{r-in(out)} = h_{r-in(out)} \Delta T_{in(out)} \tag{3.35}$$

where $h_{r\text{-}in}$ and $h_{r\text{-}out}$ are the radiative heat transfer coefficient at the inside and outside film surface, respectively. ΔT_{in} is the temperature difference between the inside of the chamber and the inside surface of the PE film. ΔT_{out} is the temperature difference between the outside surface of the PE film and the outside of the chamber.

$Q_{c\text{-}in}$ and $Q_{c\text{-}out}$ in **Eq. 3.33** are expressed by convective heat coefficient and the temperature difference inside and outside of the chamber (**Eq. 3.36**).

$$Q_{c-in(out)} = h_{c-in(out)} \Delta T_{in(out)} \tag{3.36}$$

82

where $h_{c\text{-}in}$ and $h_{c\text{-}out}$ are the convective heat transfer coefficient at the inside and outside film surface, respectively.

$Q_{g\text{-}p}$ in **Eq. 3.33** is expressed by heat conductivity of the plastic film and the surface temperature difference at the inside and outside the plastic film, ΔT_p (**Eq. 3.37**).

$$Q_{g\text{-}p} = \frac{\lambda}{d} \Delta T_p \qquad (3.37)$$

Then, **Eq. 3.33a** and **b** are expressed as, respectively:

$$Q_{r\text{-}in} + Q_{c\text{-}in} = \left(h_{r\text{-}in} + h_{c\text{-}in} \right) \Delta T_{in} \qquad (3.38)$$

$$Q_{r\text{-}out} + Q_{c\text{-}out} = \left(h_{r\text{-}out} h_{c\text{-}out} \right) \Delta T_{out} \qquad (3.39)$$

Suppose that heat transmission is equal to each term in **Eq. 3.33**, heat transmission coefficient, h_t, is obtained by substituting **Eqs. 3.35 ~ 3.37** to **Eq. 3.34**.

$$\begin{aligned}
\frac{Q_p}{h_t} &= T_{in} - T_{out} \\
&= \Delta T_{in} + \Delta T_p + \Delta T_{out} = \frac{Q_{r\text{-}in} + Q_{c\text{-}in}}{h_{r\text{-}in} + h_{c\text{-}in}} + \frac{Q_{g\text{-}p} d}{\lambda} + \frac{Q_{r\text{-}out} + Q_{c\text{-}out}}{h_{r\text{-}out} + h_{c\text{-}out}} \\
&= Q_p \left(\frac{1}{h_{r\text{-}in} + h_{c\text{-}in}} + \frac{d}{\lambda} + \frac{1}{h_{r\text{-}out} + h_{c\text{-}out}} \right)
\end{aligned} \qquad (3.40)$$

Thickness of the PE film is negligibly thin ($d = 0$). Such thin PE film transfers well shortwave and longwave radiation. Thus, it can be assumed that radiative heat transferred

without absorbing by the PE film ($h_{r-in(out)} = 0$). Hence, heat transmission coefficient can be calculated from **Eq. 3.41** by providing appropriate estimates of convective heat transfer coefficients at the inside and outside film surfaces.

$$h_t = \frac{1}{\dfrac{1}{h_{c-in}} + \dfrac{1}{h_{c-out}}}$$

(3.41)

Heat balance of the PE chamber with a black Kent paper is discussed in the following paragraphs. We assumed that the paper surface was suspended in the air and covered fully the floor surface (**Fig. 3.16b**); e.g., the view factor of the floor surface to the paper surface is one and the view factor of the floor surface to the PE film surface is zero. Hence, the area of the black Kent paper is same as that of the floor. By the assumption 5, in addition, we assumed that there was not temperature stratification above and below the black Kent paper.

Under the surface layout mentioned above, the paper upper surface of the black Kent paper receives an amount of radiation equivalent to the net radiation below the PE film, Q^{*}_{r-b}, whereas the lower surface of the black Kent paper loses the amount of radiation equivalent to the net radiation at the floor surface, Q^{*}_{r-f}. Hence, the heat balance at the paper surface is given by **Eq. 3.42** assuming no conductive component of the paper surface.

$$Q^{*}_{r-k} - Q^{*}_{r-f} = Q_{c-k}$$

(3.42)

where, Q^{*}_{r-k} is the net radiation flux at the paper upper surface and Q_{c-k} is the convective heat flux at the paper surface. Similarly to **Eq. 3.26**, **Eq. 3.42** offers an approach to evaluate Q_{c-k}

when $Q^*_{r\text{-}k}$ and $Q^*_{r\text{-}f}$ are known. The parameter $Q^*_{r\text{-}k}$ is equivalent to the net radiation flux below the PE film. Thus,

$$Q^*_{r-k} = Q^*_{r-b} = A_f\left(S^*_b + L^*_b\right) \tag{3.43}$$

$$Q^*_{r-k} = Q^*_{r-b} = A_f L^*_b \tag{3.44}$$

Equations 3.43 and **3.44** are the case in the daytime and nighttime, respectively. In both case, the net longwave radiation below the PE film is calculated from the relationship between net radiation above and below the film by substituting the paper surface temperature, T_k, into **Eq. 3.16** instead of the floor surface temperature, T_f.

At the floor surface, the expression for the heat balance is the same as in **Eq. 3.26**; however, the net longwave radiation at the floor surface, $Q^*_{r\text{-}f}$, is calculated from the black Kent paper and the floor surface temperatures as

$$Q^*_{r-f} = \varepsilon_f \varepsilon_k \sigma\left(T^4_k - T^4_f\right) \tag{3.45}$$

In the chamber with a black Kent paper, the heat balance equation in a volume is given by:

$$\rho c_p \frac{\partial T_a}{\partial t} = -Q_{c-f} - Q_{c-k} + Q_v + Q_p + Q_{g-w} + Q_{r-a} \tag{3.46}$$

By the assumption 2, temporal change is neglected ($\rho c_p(\partial T_a/\partial t)=0$). By the assumption 3, the radiative cooling of the air is negligibly small ($Q_{r\text{-}a}=0$). Hence, the sum of the convective heat

fluxes at the black Kent paper surface, Q_{c-k}, and at the floor surface, Q_{c-f}, is distributed between three components; 1) heat flux due to ventilation, Q_v; 2) heat transmission through the PE film, Q_p; and 3) conductive heat flux through sidewall, Q_{g-w}. Thus,

$$Q_{c-f} + Q_{c-k} = Q_v + Q_p + Q_{g-w} \tag{3.47}$$

Equation 3.47 offers an approach unique to the PE chamber, to evaluate Q_{c-k} when the values of Q_v, Q_p, Q_{g-w} and Q_{c-k} are known. Substituting **Eqs. 3.42** and **3.26** into **Eq. 3.47** yields the heat balance of the chamber with a black Kent paper (**Eq. 3.48**) as;

$$Q_{r-k}^{*} = Q_v + Q_p + Q_{g-w} + Q_{g-f} \tag{3.48}$$

Figure 3.16b shows the schematic of the heat balance equation in the chamber with a black Kent paper (**Eq. 3.48**). In this figure, conductive heat flux through the sidewall, Q_{g-w}, is omitted because the projection is the elevation.

3.4 The performance of the PE chamber

3.4.1 Heat balance in the heating experiment

The goal of the heating experiment was to observe how the temperatures and the heat balance components in the PE chamber respond to the heat supply from the heating cable. Heat balance of the chamber with a heater is similar to that of the chamber with a black Kent paper, but differs with respect to an additional heat gain.

Both convective and radiative heat is supplied from the heating cable as,

$$Q_h = Q_{c-h} + Q_{r-h}$$

(3.49)

where Q_h is the external heat supplied from the heater, Q_{c-h} is the convective heat flux at the heater surface, and Q_{r-h} is the radiative heat flux at the heater surface.

The portion of the radiative heat is small in comparison with that of the convective heat because the diameter of the heating cable is as small as 3mm. We measured the cable surface temperature using a thermocouple. The surface temperature was approximately 20°C higher than the temperatures of the surrounding air or surrounding surfaces under the wind speed of approximately 0.2 m s^{-1}. Using this temperature increase and a cable diameter, we estimated the radiative heat output of the cable as approximately 2W.

Similarly to **Eq. 3.48**, the sum of the convective heat from the cable, Q_{c-h}, and from the floor is distributed between three components as,

$$Q_{c-h} + Q_{c-f} = Q_v + Q_p + Q_{g-w}$$

(3.50)

Figure 3.18 shows the temporal changes of the difference between the inlet and the outlet air temperature in the PE chamber when the heater was turned on and off. As the temperature of the two chambers behaved similarly, the result of one chamber was shown in the figure. When the electrical heat of 23W was supplied into the chamber, the outlet air temperature increased about 2°C.

Heat balance components were calculated by the data collected during the two 10-min-long periods; 11:43 to 11:53 LST for no heating, and 12:20 to 12:30 LST for heating. When heated, the heat transfer values due to ventilation, Q_v, conduction through the sidewalls, Q_{g-w}, and through the floor panel, Q_{g-f}, were 19.2±0.4W, 0.25±0.05W and 0.55±0.05W (mean ± standard error over the two chambers), respectively, whereas these components were nearly zero in the absence of heating. As mentioned above, the values of Q_{r-h} is approximately 2W, such that Q_{c-h} in **Eq. 3.50** is approximately 21W. Because the experiment was conducted indoors, radiation loss from the chamber floor surface to the outside of the chamber (such as the wall surfaces in the experimental room) through the PE film was very small, but positive. When the floor surface is assumed to receive a half of Q_{r-h}, the values of Q^*_{r-f} in **Eq. 3.26** is at most 1W. Hence, convection at the floor surface Q_{c-f} is estimated at least about 0.45W. Consequently the left hand of **Eq. 3.50** is estimated about 21.5W at most. These results indicate that approximately 90% of the convective heat flux coming out inside the chamber, defined by **Eq. 3.50**, was transported to the outside of the chamber by ventilation. It means that the heat flux due to ventilation, Q_v, is the most important measure for evaluating heat exchange processes occurring in the PE chamber.

3.4.2 Relationship between net radiation inside and outside of the PE chamber

As clearly demonstrated in **Eq. 3.21**, the net longwave radiation below the PE film is smaller than that above the film during the nighttime. In **Table 3.2**, the net radiation flux densities above and below the PE film are compared; one of the densities was measured using the net radiometer in the chamber without a black Kent paper, whereas the other was calculated from **Eqs. 3.16** through **3.20** and the processes explained in Section 3.3. The results listed in **Table 3.2** reveal a close agreement between the measured and calculated values of net radiation

below the film between the measured and calculated values. These results also confirm that the net radiation flux density below the PE film can be estimated accurately by **Eqs. 3.16** through **3.20** when the inside surface temperature is known. Both measured and calculated fluxes indicate that the net radiation below the PE film was reduced by approximately 10% compared to that above the PE film.

In the daytime, as with the nighttime, net radiation below the PE film is guessed to become smaller than that above the PE film because a portion of shortwave radiation is absorbed or reflected by the polyethylene film (**Eq. 3.11**). To examine the attenuation of net radiation by the PE film in the daytime, two net radiometers were placed next to each other for 15 min on the building's roof of Graduate School of Life and Environment Sciences, the University of Tsukuba on July 30th, 2013. Thus, it could be considered that two net radiometer received the same upward shortwave and longwave radiation from the ground surface because both net radiometer were placed at the same roof surface. We prepared the PE film that was cut in 250cm^2, and compared two net radiometers; one was covered with the PE film and another one was covered with nothing. As a result, it was shown that 15-min averaged net radiation attenuate approximately 10% when the PE film covered the net radiometer. This attenuation of net radiation indicated that the PE film absorbed or reflected shortwave and longwave radiation during the daytime.

However, when net radiometers placed above and below the PE film of the PE chamber, the difference of the net radiation above and below the PE film did not reach 10% in the daytime. The chamber's floor under the net radiometer was shadowed by the net radiometer in the daytime. Therefore, net radiation below the PE film become larger since the upward longwave radiation decreased most locally. In addition, the area projected from the under surface of two

net radiometers were different because the height of each net radiometer was different. The under surface of the net radiometer above the PE cover projected the floor surface and the sidewalls of the chamber, while the under surface of the net radiometer below the PE cover projected the floor surface only. More shortwave radiation which was reflected by the aluminium of the sidewalls irradiated on the under surface of the net radiometer above the PE film. Therefore, net radiation below the PE cover was almost the same or little larger than that above the PE cover in the daytime (**Fig. 3.19**). In the nighttime, on the other hand, the input and output energy values were smaller than that in the daytime. Thus, the difference of net radiation between above and below the cover does not possibly appear during the nighttime. Contrary to the nighttime, it was difficult to measure directly the net radiation below the film during the daytime.

3.5 Summary

An approach to investigate heat exchange between vegetation surface and surrounding air under nocturnal radiative cooling has been serious problem. In case of wind tunnel, it is extremely difficult to satisfy the physical similarity law for stable atmospheric condition. In case of ventilated chamber, the material used in most ventilated chamber, which was opaque to longwave radiation, is an obstacle to investigate heat exchange under nocturnal radiative cooling. Hence, we proposed and developed a new apparatus, the polyethylene (PE) chamber, to investigate heat exchange process between vegetation surface and surrounding air. The PE chamber has two ends serving as an air inlet and an air outlet, and it was ventilated in the longitudinal direction using an exhaust fan. Therefore, there is an air temperature difference between the inlet and the outlet of the chamber. Using the air temperature difference between the

inlet and the outlet and other heat balance components, we could evaluate heat exchange process. The measurement section of the PE chamber and was covered with thin PE film. Thin PE film has a transmittance as high as 85% or larger for not only shortwave radiation but also longwave radiation. Therefore, the radiative environment in the PE chamber was similar to outdoor that. Hence, the PE chamber was applicable to evaluate heat exchange under nocturnal radiative cooling.

We derived the radiation and heat balance equations of the PE chamber and proposed two approaches to evaluate the convective heat flux at the floor or the Kent paper surface under the radiative cooling; one approach was based on net radiation inside the chamber, while another approach was based on the heat balance of the PE chamber.

Preliminary experiments were performed to evaluate the performance of the PE chamber. From the heating experiment, it was found that more than 90% of convective heat generated inside the chamber was transported to the outside of the chamber by ventilation. The relationship of the longwave radiation between above and below the PE film was examined using two net radiometers. The net radiation below the PE film was reduced by about 10% compared to that above the PE film. Therefore, the errors in the estimation of additional components, such as heat conduction through the sidewalls and heat transmission through the PE film, did not significantly affect the evaluation of the convective heat flux.

The design and related heat balance about the PE chamber were explained in this chapter. In the following section, we shall investigate heat exchange process installing the PE chamber in the outdoors.

Table 3.1. Date, time and place of the calibration experiments for the net radiometers. Correction coefficients of the net radiometer are the positive and negative values in the daytime and nighttime, respectively. Average error was calculated from the difference of two net radiometers.

	For negative values		For positive values
Date	2013.02.28	2013.08.15	2013.07.31
Time (LST)	17:04 – 17:24	20:30 – 20:55	09:50 – 10:30
Place	Iwate University	University of Tsukuba	
Average Error (W m^{-2})	0.1	0.0	-0.1
RMSE (W m^{-2})	0.38	0.04	2.13

Table 3.2. Comparison of the measured and the calculated net longwave radiation below the PE film, Q^*_{r-b}, and longwave radiation fluxes inside and outside the chamber. The 10-min average data were collected when the transit change of the net radiometer signal was considered to disappear 3 minutes after settling the instrument. The longwave radiation from the sky, L_{sky}, was calculated from **Eq. 3.24**. The upward longwave radiation flux density at the PE film surface, L_{p-up}, is calculated from **Eq. 3.17**. The downward longwave radiation flux density at the PE film surface, L_{p-down}, was calculated from **Eq. 3.18**. The longwave radiation from the floor surface, L_{f-up}, was calculated from **Eq. 3.23**. The calculated net radiation flux below the PE film, Q^*_{r-b}, was calculated from **Eq. 3.25** and **3.15**.

	Q^*_{r-a} [W m^{-2}]	Q^*_{r-b} [W m^{-2}]	L^*_a/L^*_b	L_{sky} [W m^{-2}]	L_{p-up} [W m^{-2}]	L_{p-down} [W m^{-2}]	L_{f-up} [W m^{-2}]
Measured	-39.5	-35.0	0.89	-	-	-	-
Calculated	-	-35.7	0.90	267.3	306.8	274.8	310.5
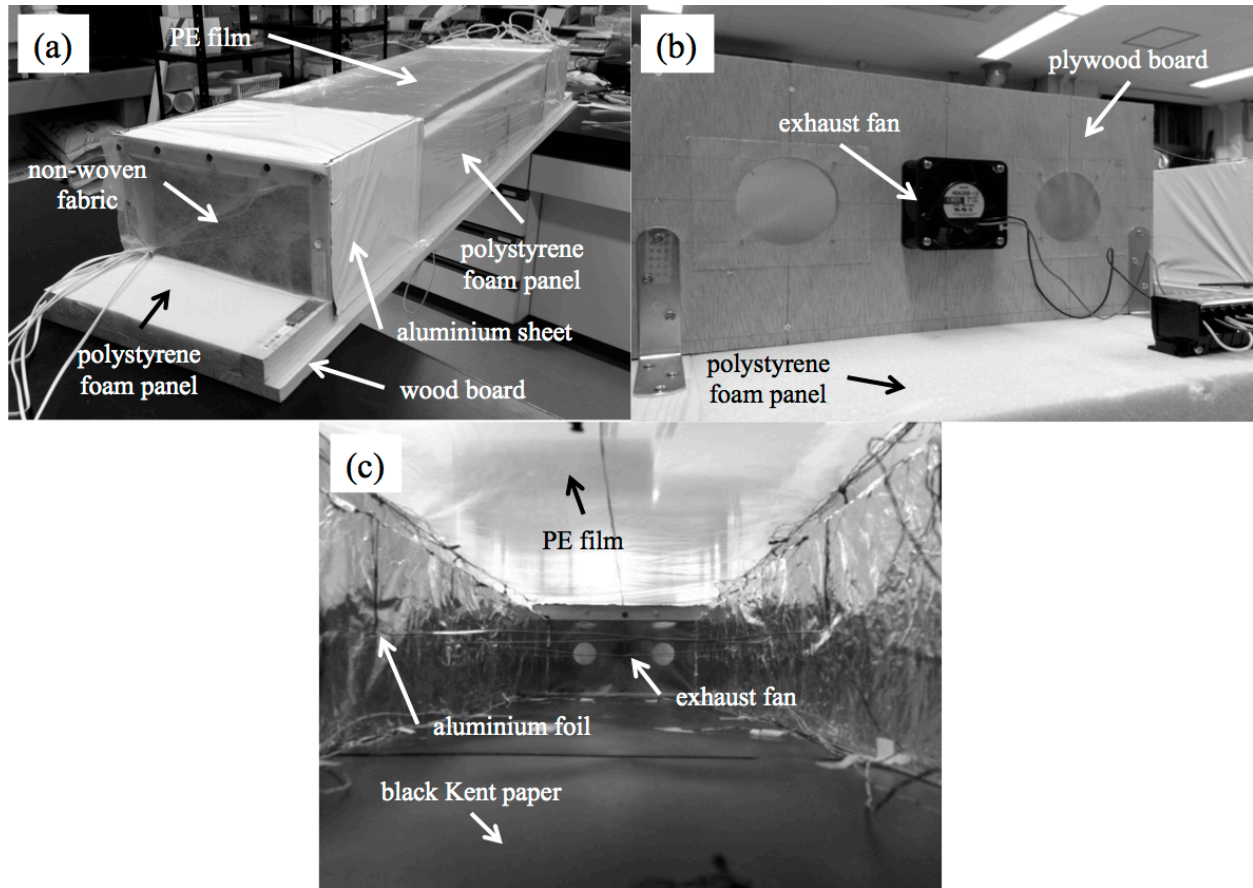
Fig. 3.1. View of the PE chamber at the air inlet (a), at the air outlet (b) and of the inside of PE section (c). The chamber was a 1.51 m-long tube with its two ends serving as an air inlet and an air outlet, and it was ventilated in the longitudinal direction using an exhaust fan. A wood board was used as a chamber base. An extruded polystyrene foam panel was used as a chamber floor, sidewalls and ceiling of the inlet and outlet sections. A PE film was used as ceiling of the PE section. An aluminum foil was used as sidewall surfaces. A black Kent paper was attached on the floor surface.
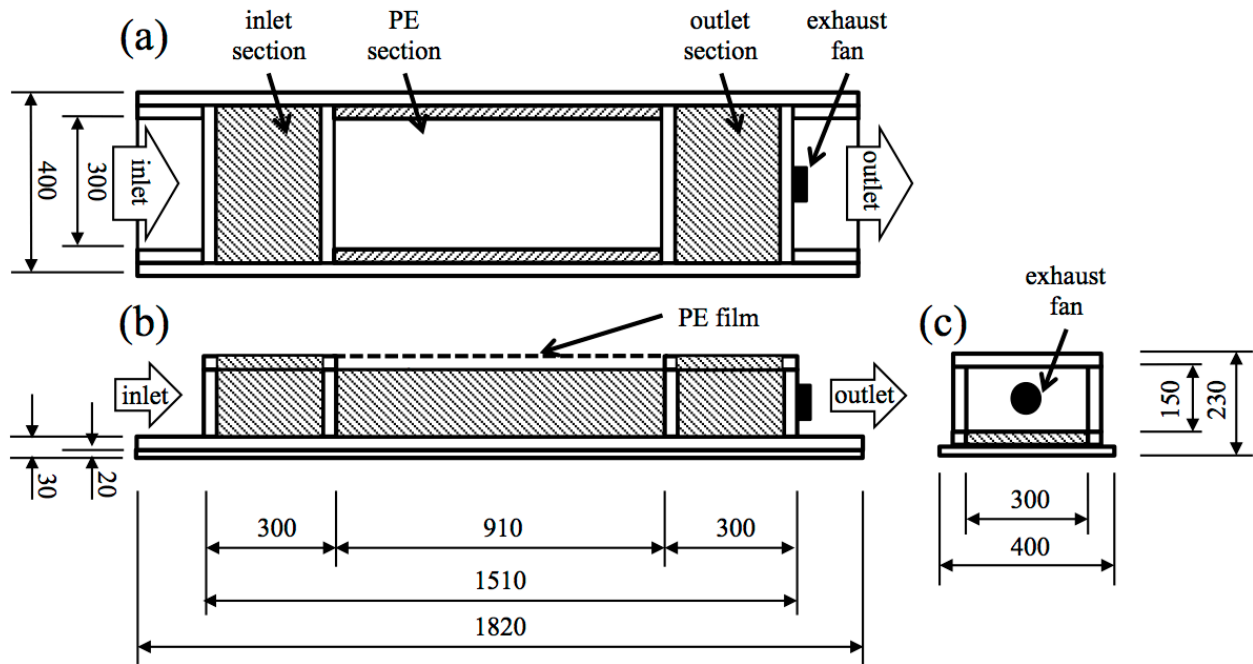
Fig. 3.2. Design of the PE chamber. (a) Plane view. (b) Elevation view. (c) A cross section view at the air outlet. Values written in the figures are length in mm. Shadowed areas indicate an extruded polystyrene foam panel. The chamber was a 1.51 m-long tube that consisted of the inlet, outlet, and PE section. The chamber had two ends serving as an air inlet and an air outlet, and it was ventilated in the longitudinal direction using an exhaust fan. A wood board was used as a chamber base. An extruded polystyrene foam panel was used as a chamber floor, sidewalls and ceiling of the inlet and outlet sections. A PE film was used as ceiling of the PE section.
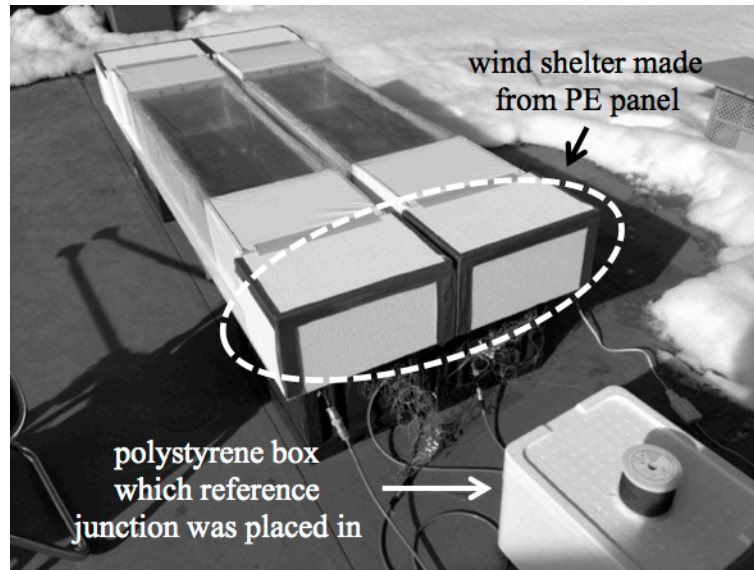
Fig. 3.3. Location of the outdoor experiment using the PE chamber. To prevent unfavourable effects of outdoor wind, two end sections outside the inlet and the outlet were covered with a wind shelter made from polystyrene panel. All of the sensing junctions were connected to one common reference junction to minimize possible instrumental errors arising when individual separate thermocouples are used. The reference junction was placed in a polystyrene box during the experiment.
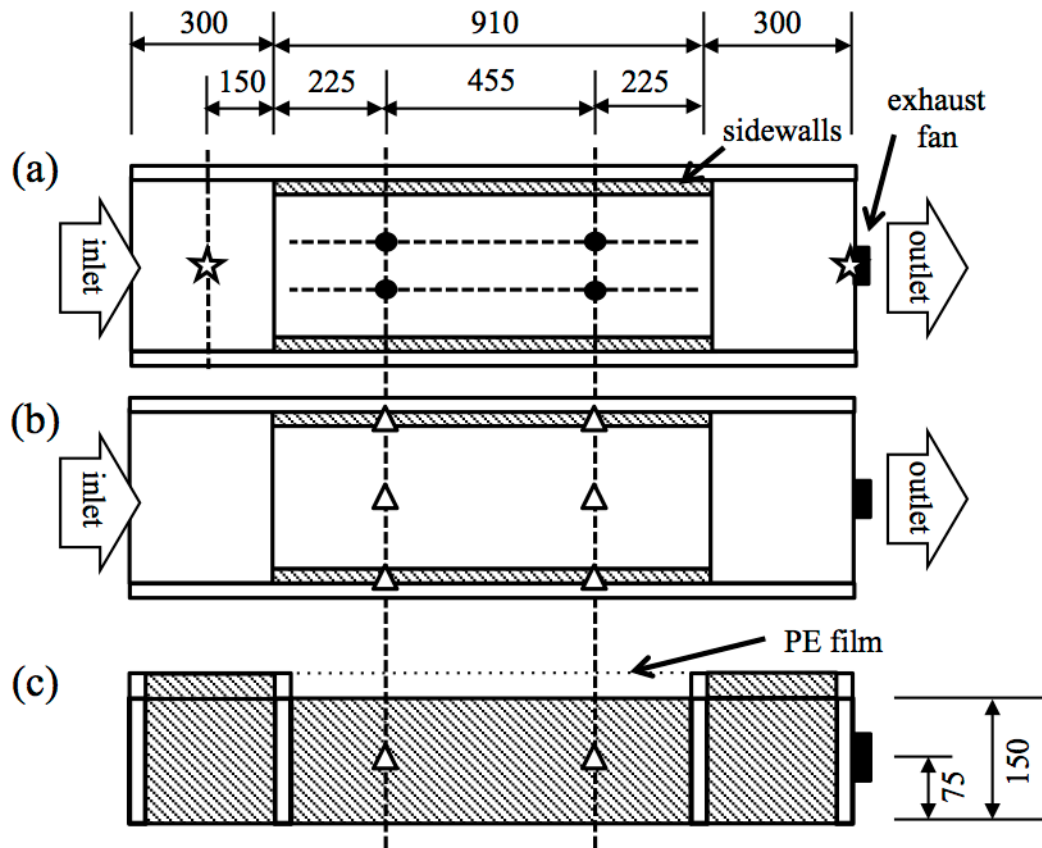
Fig. 3.4. Temperature measurement locations in the chamber without a black Kent paper (length in mm). Shadowed areas indicate an extruded polystyrene foam panel. A wood board as a chamber base is omitted in this figure. (a) Plane view of the measurement locations for air temperature and floor surface temperature. Stars indicate incoming and outgoing air temperature and circles indicate floor surface temperature. (b) Plane view of the measurement locations for the temperature difference between the inside and outside surfaces of the extruded polystyrene foam panel. (c) Elevation view of the measurement locations for the temperature difference between the inside and outside surfaces of the extruded polystyrene foam panel. Triangles indicate the locations which conductive heat flux was calculated by measuring the temperature difference between the inside and outside surfaces of the extruded polystyrene foam panel.

97
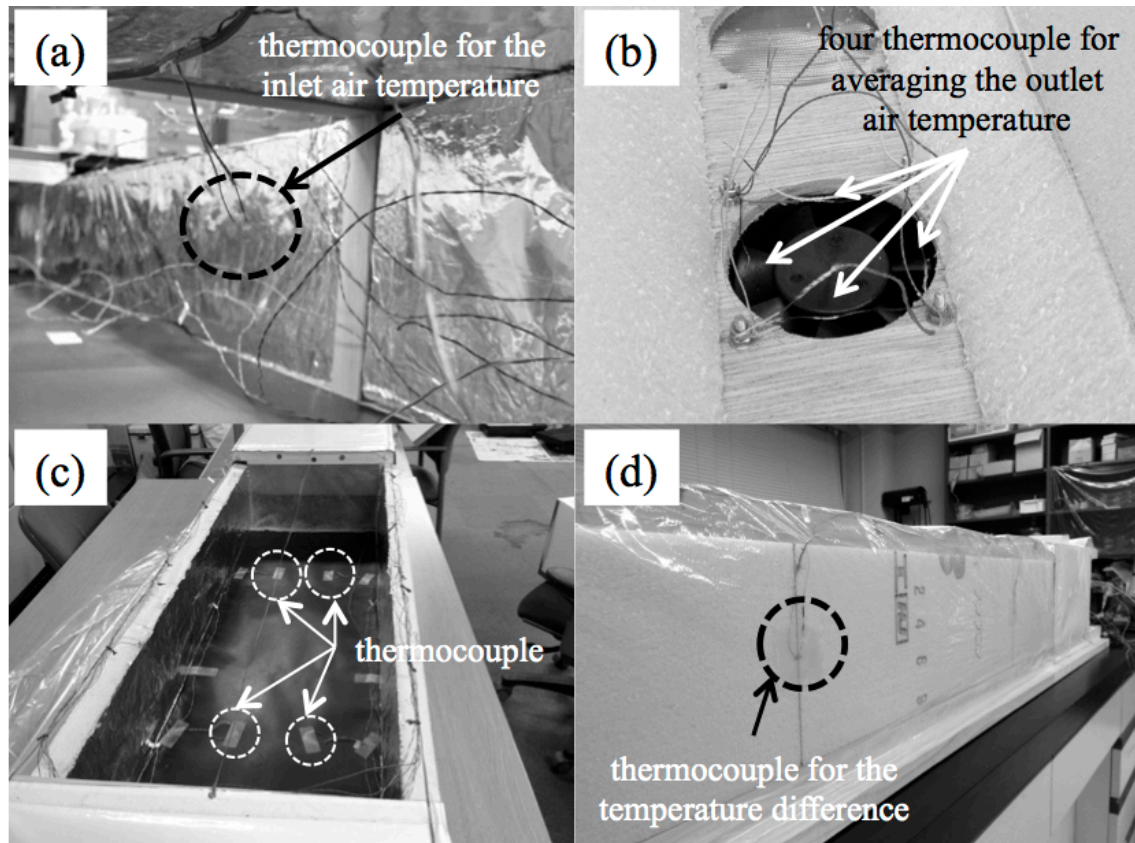
Fig. 3.5 View of thermocouples for the inlet air temperature (a), the outlet air temperature (b), the floor surface temperature (c), temperature difference between the inside and the outside surfaces of the extruded polystyrene foam panel at the floor or the sidewall (d). Four thermocouples were used to obtain the average outlet air temperature. Each thermocouple was placed at the left, right, top, and bottom of the windward cross section of the exhaust fan.
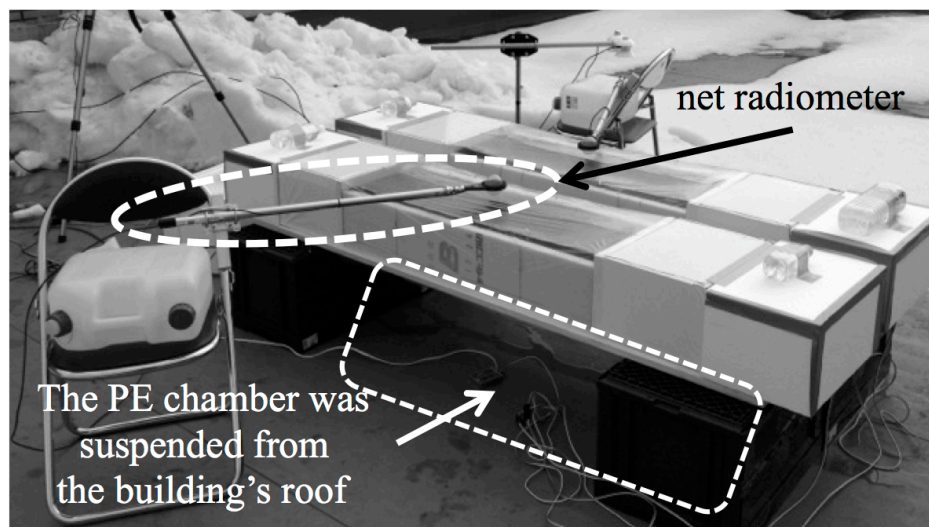
Fig. 3.6. View of the outdoor experiment using the PE chamber. Net radiometer was placed next to the PE chamber and measured net radiation above the PE film. The PE chamber was suspended at a height of 300mm above the building's roof using the plastic box. The sensor of a net radiometer was set on the center of the PE section above the PE film.
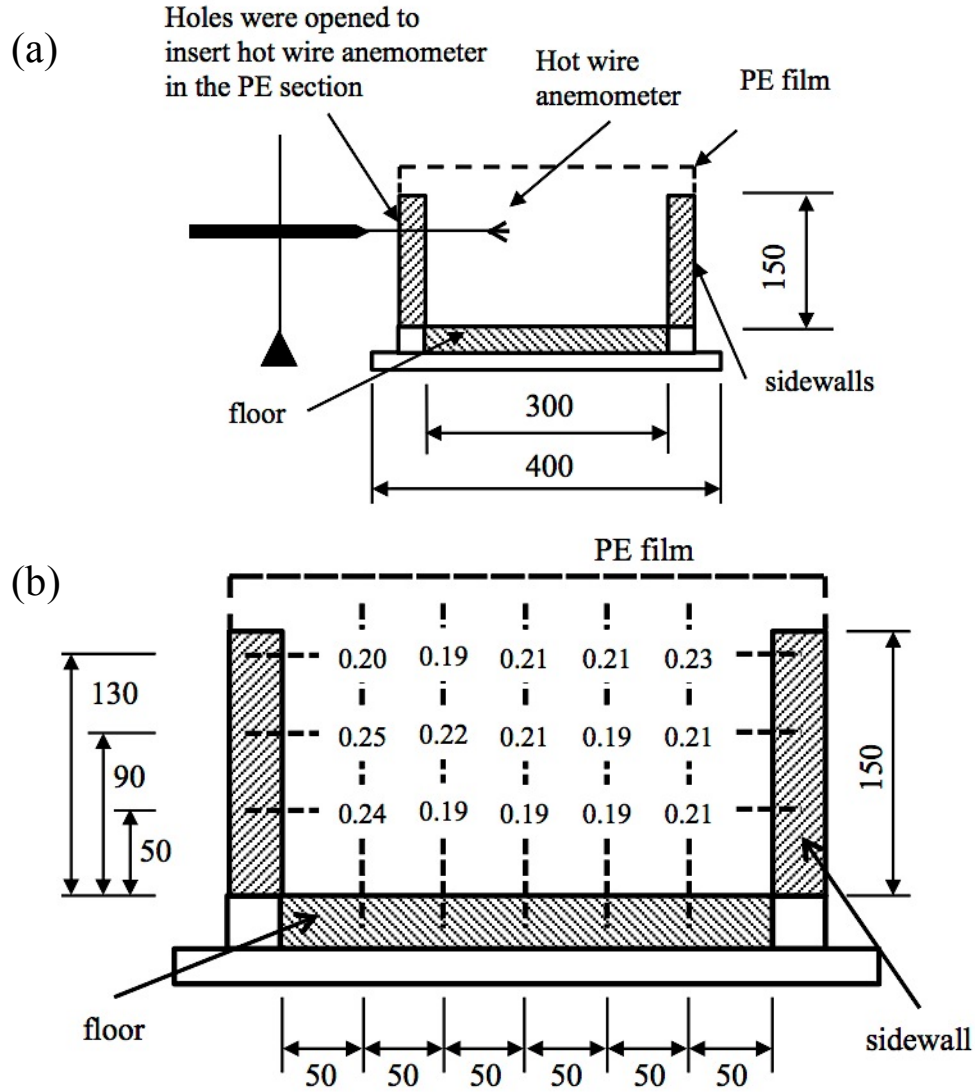
Fig. 3.7. (a) Cross-section schematic of the measurement for wind speed of the inside chamber using the non-dimensional hot wire anemometer (length in mm). A hole, which an anemometer pierced through, was opened in the sidewall only during the measurement. The anemometer was fixed by a stand. (b) Cross-section profile of wind speed at the PE section of a chamber (wind speed in m s^{-1}, length in mm). Values written in the chamber are wind speed (m s^{-1}). Value written on the right side of the chamber is the height of the sidewall (mm). Values written below the chamber are the horizontal distance for measuring wind speed (mm). Values written on the left side of the chamber are the height for measuring wind speed (mm). Shadowed areas indicate an extruded polystyrene foam panel.
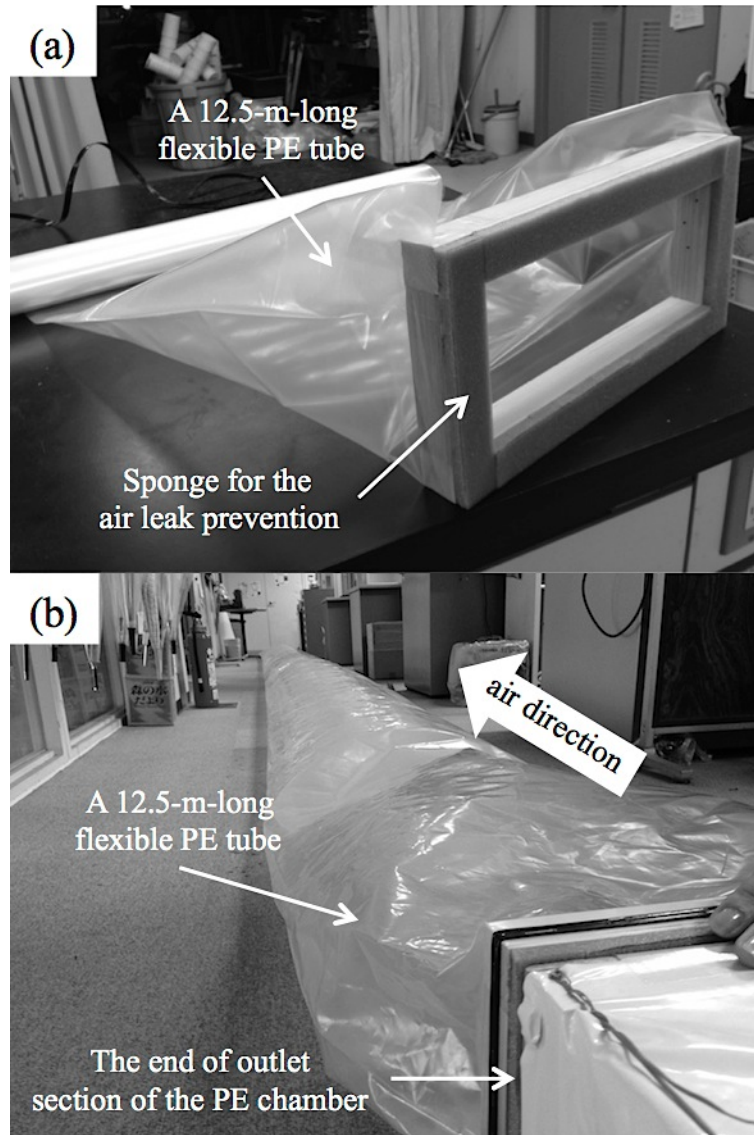
Fig. 3.8. (a) View of the flexible PE tube. (b) View of the measurement for the volumetric flow. An air exhaust rate was calculated from the time passed until full inflation and the volume of the flexible PE tube.
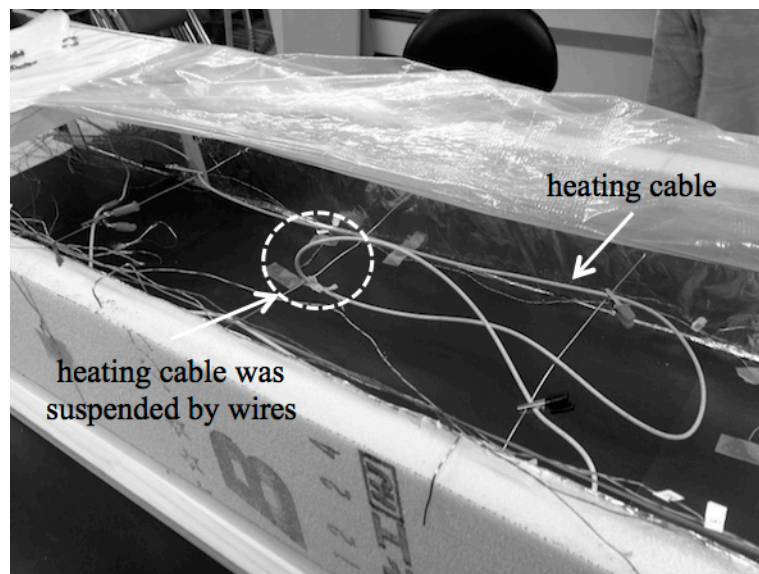
Fig. 3.9. View of the cable heater installed in the chamber. A 2-m long heating cable was suspended about 70mm above the floor of the PE section. The output of the cable heater was 23W. Two chambers were used for the measurement and the heater was repeatedly switched at intervals of 30 min. The chambers were placed inside a calm room.
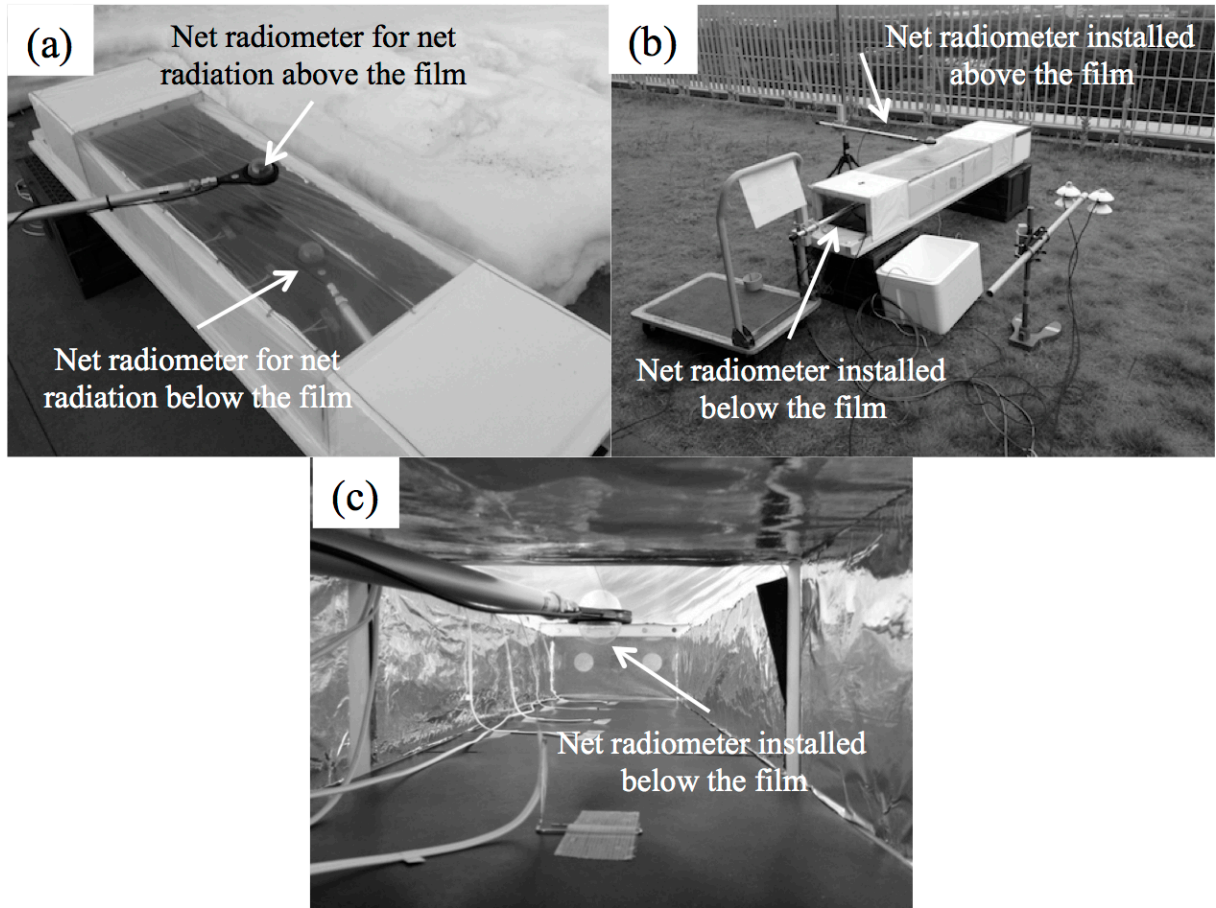
Fig. 3.10. View of the outdoor measurement for radiation balance inside and outside of the PE-chamber in Iwate University (a), in the University of Tsukuba (b). (c) View of installing a net radiometer to the inside of the PE chamber. Two sets of the net radiometers were prepared. One of the radiometers was set above the PE section, while another one was set under the PE cover inside the PE section. The inside radiometer was inserted from the air inlet of the chamber. The net radiometer inside the chamber was installed to avoid colliding with the inside surfaces of the chamber.
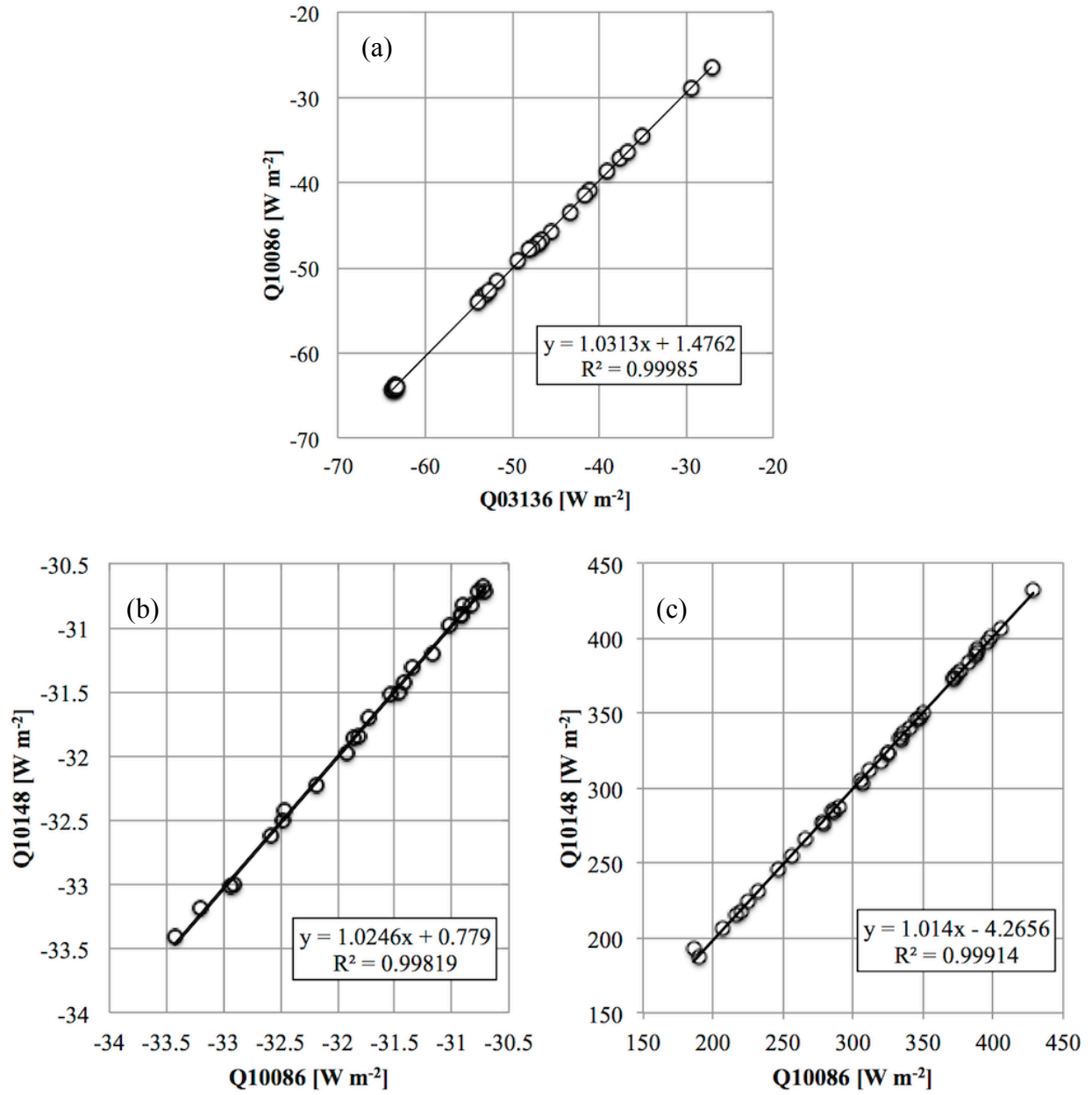
Fig. 3.11. Correlation of net radiation between two sets of net radiometer after the correction experiments. The correction experiments were conducted in Iwate University from 17:04 to 17:24 LST of February 28th (a), in the University of Tsukuba from 20:30 to 20:55 LST of August 15th (b), in the University of Tsukuba from 09:50 to 10:30 LST of July 31th (c). The standard net radiometer is the vertical axis.
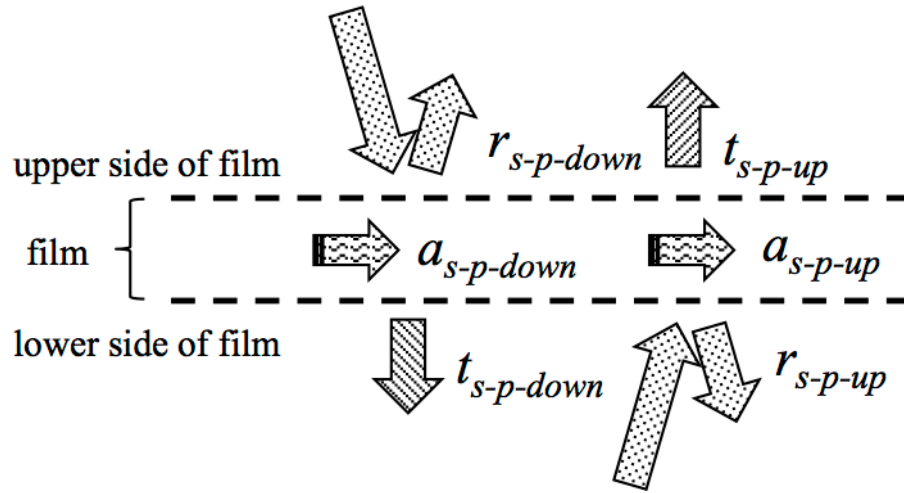
Fig. 3.12. Cross-section schematic of the difference of the characteristic for upward and downward shortwave radiation of the PE film. Dashed lines indicate the PE film surface. Area between two dashed lines indicates the PE film. Arrows filled with dot pattern indicate the reflective characteristic. Arrows filled with slanted lines indicate the transmissive characteristic. Arrows filled with wavy pattern indicate the absorptive characteristic. $r_{s\text{-}p\text{-}down}$ is reflectivity of the PE film for downward shortwave radiation. $a_{s\text{-}p\text{-}down}$ is absorptivity of the PE film for downward shortwave radiation. $t_{s\text{-}p\text{-}down}$ is transimissivity of the PE film for downward shortwave radiation. $r_{s\text{-}p\text{-}up}$ is reflectivity of the PE film for upward shortwave radiation. $a_{s\text{-}p\text{-}up}$ is absorptivity of the PE film for upward shortwave radiation. $t_{s\text{-}p\text{-}up}$ is transimissivity of the PE film for upward shortwave radiation.
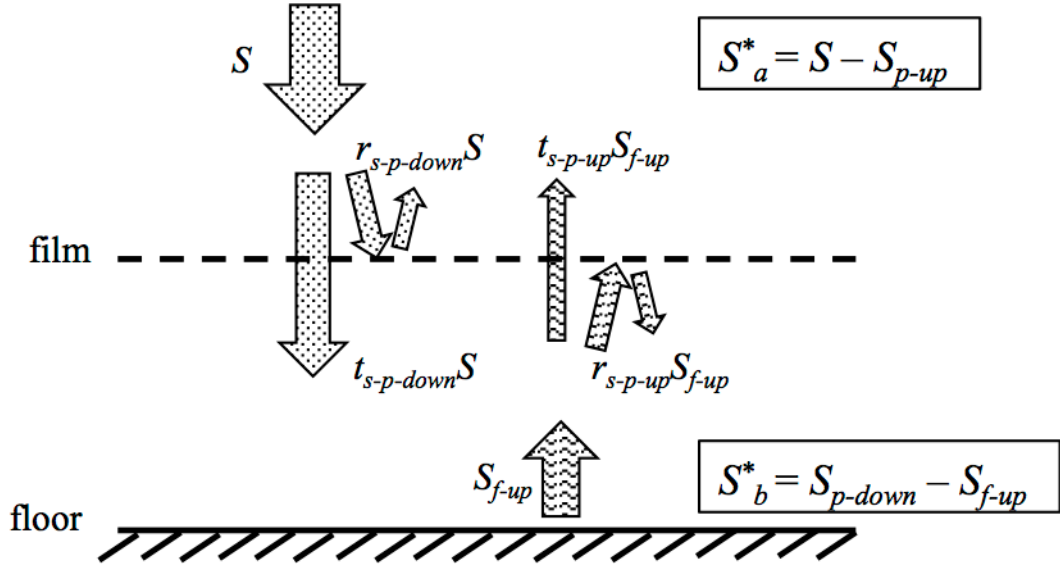
Fig. 3.13. Cross-section schematic of shortwave radiation balance above and below the PE film and at the floor surface in the PE chamber. Dashed and solid line indicate the PE film and floor, respectively. Arrows filled with dot pattern indicate radiative components of outdoor shortwave radiation flux density, S, origin. Arrows filled with wavy pattern indicate radiative components of shortwave radiation flux density going upward at the floor surface, $S_{f\text{-}up}$, origin. Shortwave radiation flux density going upward at the outside film surface, $S_{p\text{-}up}$, is expressed as the sum of outdoor shortwave radiation reflected by the upside of the PE film, $r_{s\text{-}p\text{-}down}S$, and upward directed shortwave radiation at the floor surface transmitted by the PE film, $t_{s\text{-}p\text{-}up}S_{f\text{-}up}$. Shortwave radiation flux density going downward at the inside film surface, $S_{p\text{-}down}$, is expressed as the sum of outdoor shortwave radiation transmitted by the PE film, $t_{s\text{-}p\text{-}down}S$, and upward directed shortwave radiation at the floor surface reflected by the lower surface of the PE film, $r_{s\text{-}p\text{-}up}S_{f\text{-}up}$. S^{*}_{a} is net shortwave radiation flux density above the PE film. S^{*}_{b} is net shortwave radiation flux density below the PE film.

106

$$L^*_a = L_{sky} - L_{p\text{-}up}$$

$$L^*_b = L_{p\text{-}down} - L_{f\text{-}up}$$
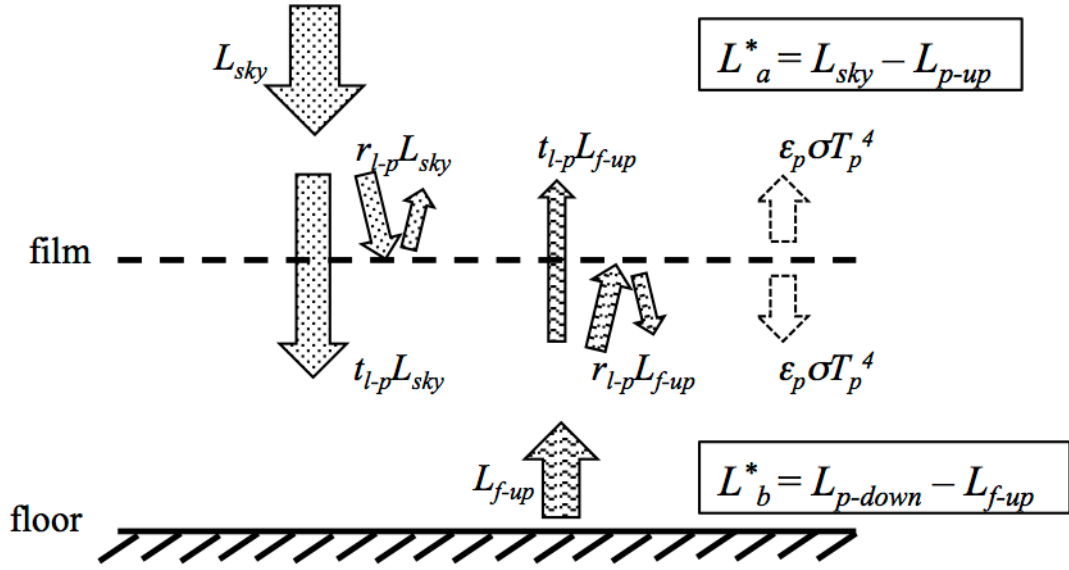
Fig. 3.14. Cross-section schematic of longwave radiation balance above and below the PE film and at the floor surface in the PE chamber. Dashed and solid line indicate the PE film and floor, respectively. Arrows filled with dot pattern indicate radiative components of sky longwave radiation flux density, L_{sky}, origin. Arrows filled with wavy pattern indicate radiative components of longwave radiation flux density going upward at the floor surface, $L_{f\text{-}up}$, origin. Dashed arrows indicate the longwave radiation emitted from the PE film, $\varepsilon_p\sigma T_p^4$. Longwave radiation flux density going upward at the outside film surface, $L_{p\text{-}up}$, is expressed as the sum of the longwave radiation emitted going upward from the PE film, $\varepsilon_p\sigma T_p^4$, the longwave radiation transmitted through the PE film, $t_{l\text{-}p}L_{f\text{-}up}$, and the sky longwave radiation reflected by the PE film, $r_{l\text{-}p}L_{sky}$. Longwave radiation flux density going downward at the inside film surface, $L_{p\text{-}down}$, is expressed as the sum of the longwave radiation emitted going downward from the PE film, $\varepsilon_p\sigma T_p^4$, the sky longwave radiation transmitted through the PE film, $t_{l\text{-}p}L_{sky}$, and the longwave radiation reflected by the PE film, $r_{l\text{-}p}L_{f\text{-}up}$. $L_{n\text{-}a}$ is net longwave radiation flux density above the PE film. $L_{n\text{-}b}$ is net longwave radiation flux density below the PE film.
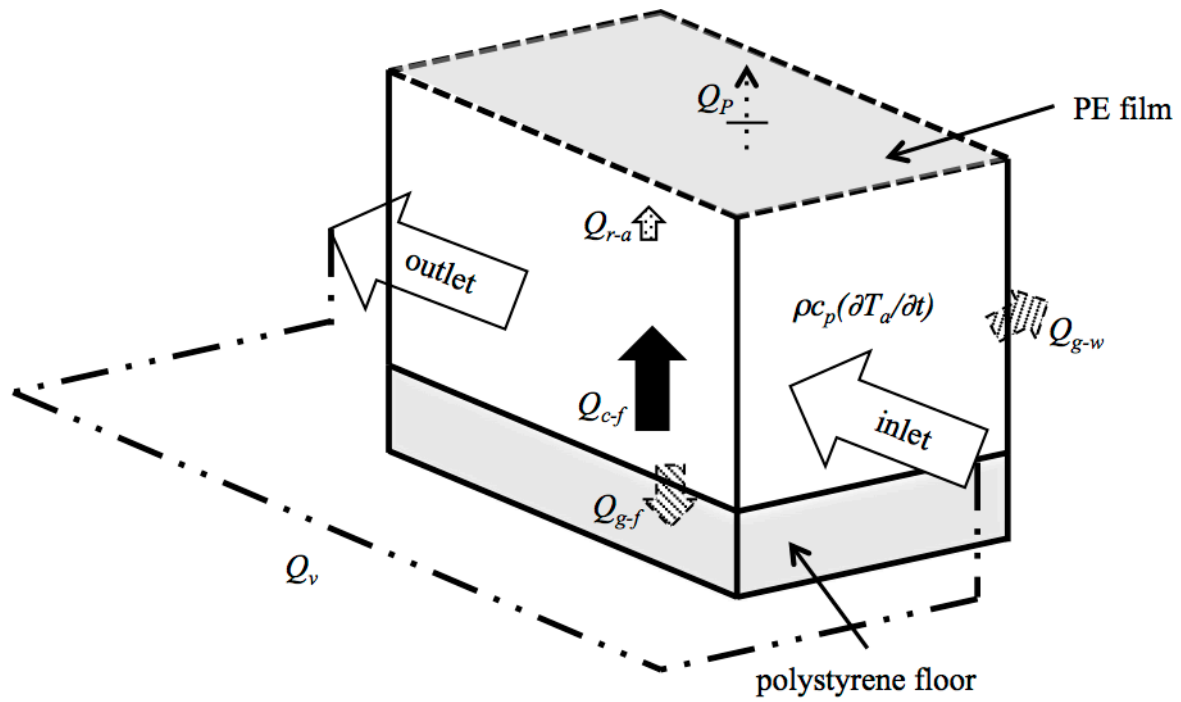
Fig. 3.15. 3-D schematic of fluxes involved in the energy balance of an air volume in the PE chamber. PE film and polystyrene floor were filled with gray color. Temporal change of air temperature inside the chamber, $\rho c_p(\partial T_a/\partial t)$, is divided by five heat balance components. White arrows are heat transfer due to ventilation, Q_v. Black Arrow is convective heat flux at the floor surface, Q_{c-f}. Arrows filled with slanted lines are conductive heat flux through sidewalls and floor, Q_{g-w} and Q_{g-f}. Dotted arrow is heat transmission through the PE film, Q_p. Arrow filled with dots is radiative cooling of the air, Q_{r-a}.
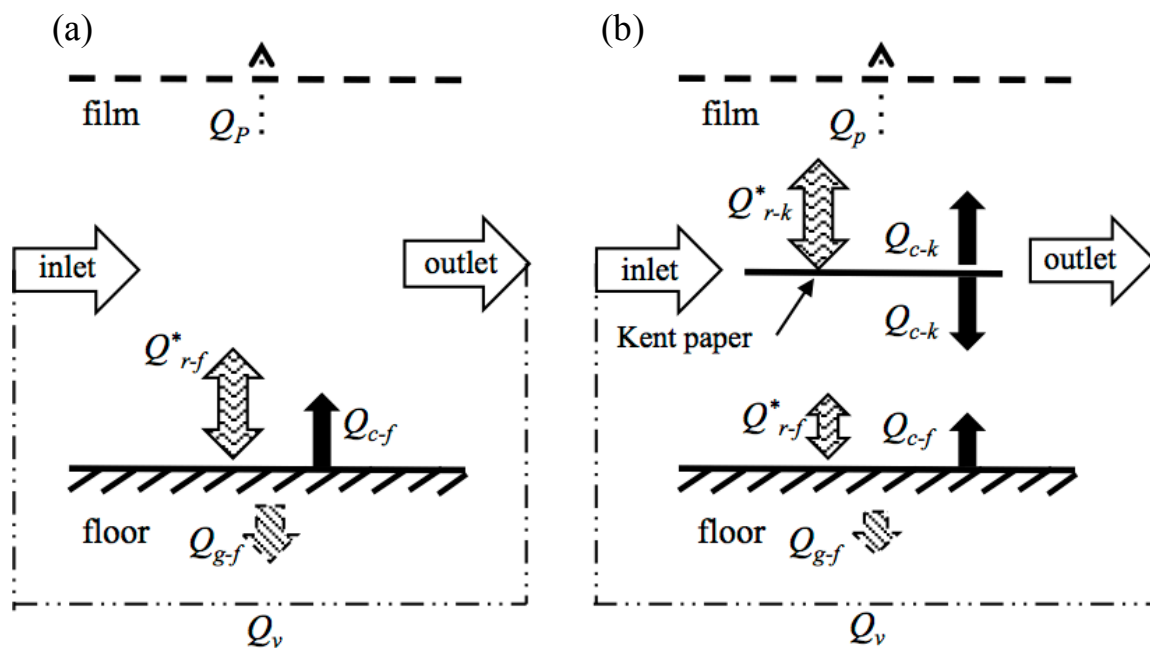
Fig. 3.16. Cross-section schematic of heat balance in the PE chamber without a black Kent paper (a) and with a black Kent paper (b). Q_{c-f} is convective heat flux at the floor surface. Q_{c-k} is convective heat flux at the Kent paper surface. Q_p is the heat transmission through the PE film. Q_v is the sensible heat flux due to ventilation. Q^*_{r-f} is net radiation at the floor surface. Q^*_{r-k} is net radiation at the Kent paper surface. In this figure, conductive heat flux through the sidewalls, Q_{g-w}, is neglected because the figure's projection is the elevation.
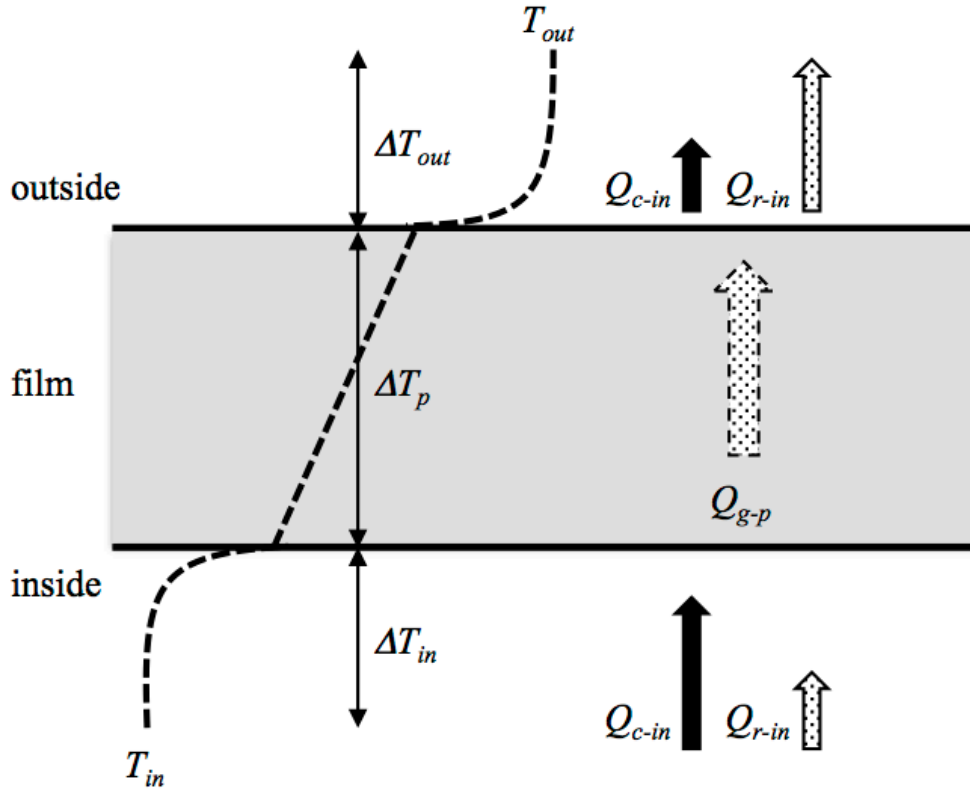
Fig. 3.17. Schematic of heat transfer through the plastic film: e.g., a PE film. Since it is difficult to measure surface temperature inside and outside of the plastic film, heat transfer from the inside to the outside of chamber is considered as heat transmission through a plastic film, Q_p. Q_{c-in} is convective heat transfer from the inside of the chamber to the surface inside of the plastic film, Q_{c-out} is convective heat transfer from the surface outside of the plastic film to the outside of the chamber, Q_{g-p} is conductive heat transfer through the plastic film, Q_{r-in} is radiative heat transfer from the inside of the chamber to the surface inside of the plastic film and convective heat, and Q_{r-out} is radiative heat transfer from the surface outside of the plastic film to the outside of the chamber. ΔT_{in} is the temperature difference between the inside of the chamber and the inside surface of the polyethylene film. ΔT_{out} is the temperature difference between the outside surface of the polyethylene film and the outside of the chamber. ΔT_p is the surface temperature difference at the inside and outside the plastic film.
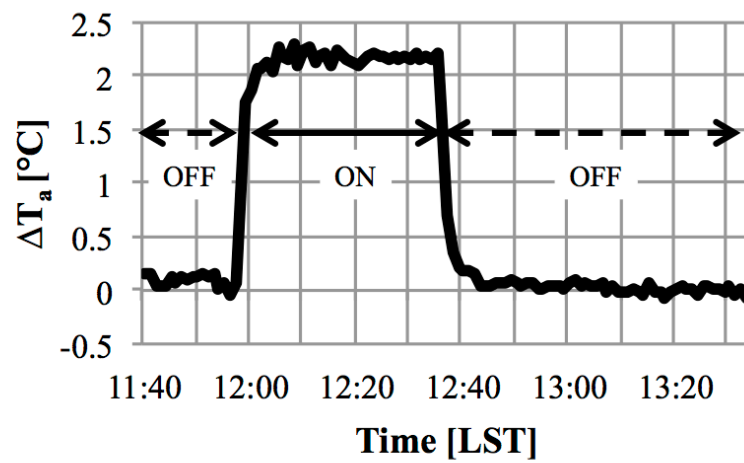
Fig. 3.18. Temporal changes of the difference between the inlet and the outlet air temperature in the PE chamber. Arrows indicate the on/off periods of the heater.
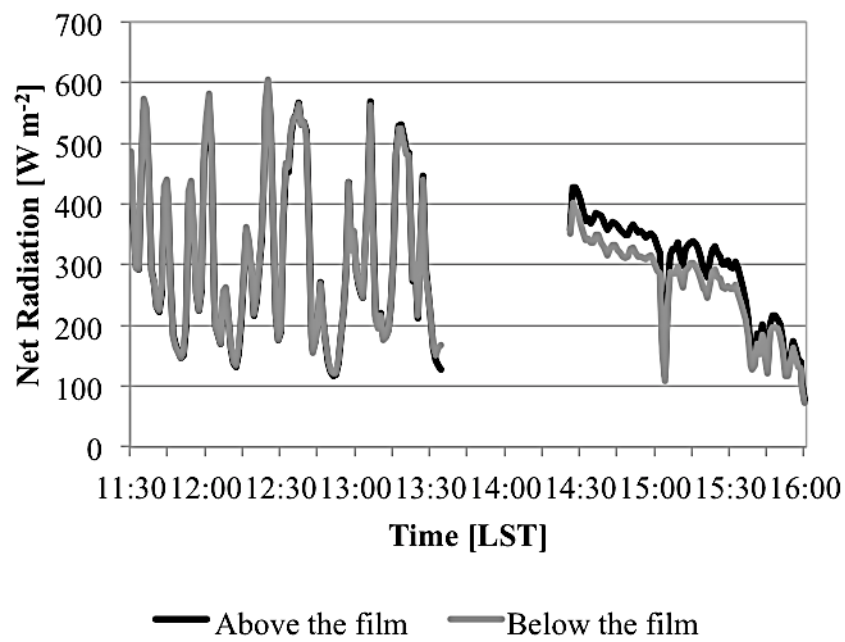
Fig. 3.19. Temporal changes of the daytime net radiation above and below the PE film. The measurement was conducted on the building's roof at Graduate School of Life and Environment Sciences, the University of Tsukuba on July 26th, 2013. Black and gray solid lines indicate the net radiation above and below the PE film, respectively.

4. Heat exchange between vegetation surface and surrounding air using the PE chamber

4.1 Previous studies and objective

Convective heat exchange at leaf surfaces depends on the leaf morphology. Sinclair (1970) examined convective heat exchange using artificial leaves in a wind tunnel and revealed that the convective heat exchange at the leaf surface increased as the leaf area decreased. The depth of the thermal boundary layer at the leaf surface decreases as the characteristic length of the leaf area decreases. Hence, the thinner thermal boundary layer enhances convective heat exchange at the leaf surface.

The dependence of convective heat exchange on the vegetation morphology was applied to vegetation canopies. Kondo and Watanabe (1992) developed a multilayer energy balance model of the vegetation canopy to describe the fluxes of sensible and latent heat transferred between the vegetation surface and the atmosphere. The values of the bulk transfer coefficients in their model depended on the vegetation parameters, i.e., vegetation types and density. Using their model, Watanabe (1994) revealed that a dense vegetation canopy exhibited a higher sensible heat flux. Thus, the area of the heat exchange surface of vegetation, that is, the vegetation size, affects the heat exchange at vegetation surfaces.

As with the vegetation size, the vegetation allocation (e.g., the allocation of an urban park) also affects the heat exchange at vegetation surfaces. A larger park is more isolated from the surrounding built-up area in terms of heat transfer. Therefore, heat exchange between the park and the surrounding built-up area is less enhanced for a large park. Kanda and Hino (1990a, b)

demonstrated this effect of isolation on daytime air cooling by vegetation well using simulation studies. They compared an aggregated vegetation area to a sparsely scattered one and concluded that the scattered vegetation area cooled the surrounding urban atmosphere more effectively.

Many studies have examined the daytime dependence of the heat exchange on the vegetation morphology. Their results might contribute to the improvement of the daytime urban thermal environment. On the other hand, the nocturnal dependence of the heat exchange on the vegetation morphology is not well known, although nocturnal heat stroke in urban areas has recently become a concern. To investigate the nocturnal heat exchange processes between the vegetation surfaces and the surrounding air, Okada et al. (2013b) proposed and developed the polyethylene (PE) chamber. Because a thin PE film has a high transmittance for longwave radiation, the chamber enables the evaluation of heat exchange under nocturnal radiative cooling.

The purpose of this chapter is to experimentally examine the heat exchange for various vegetation sizes and allocations using the PE chamber.

4.2 Methods

4.2.1 Concept of experiments using the PE chamber

In this chapter, heat exchange at vegetation surfaces is investigated by inserting black Kent papers into the PE chamber instead of real vegetation. A black Kent paper allows heat exchange at both the upper and lower surfaces, like a real leaf, because the thermal capacity of a real leaf is negligibly small. Therefore, the problems with using a black Kent paper for investigating heat exchange between vegetation surfaces and the surrounding air are relatively minor.

This chapter explains two experiments: 1) preliminary experiments that evaluate the performance of the PE chamber and 2) experiments that evaluate the dependence of the heat

exchange on the vegetation morphology.

First, two preliminary experiments were conducted to examine the performance of the PE chamber in the evaluation of 1) the heat exchange and 2) the cooling effect on evaporative surfaces such as those of real leaves.

Second, two experiments were conducted to examine the dependence of the heat exchange on the vegetation morphology in terms of 1) the area of the heat exchange surface and 2) its characteristic length.

4.2.2 Measurements

In the experiments, two PE chambers were installed on the roofs of buildings at the Faculty of Agriculture, Iwate University, Morioka, Japan (39°42′N, 141°8′E) (hereafter referred to as Iwate University) and the Graduate School of Life and Environment Sciences, University of Tsukuba, Tsukuba, Japan (36.87°N, 141.7°E) (hereafter referred to as the University of Tsukuba) (**Fig. 4.1**). The roof surfaces at Iwate University and the University of Tsukuba were covered with a waterproof rubber sheet and grass, respectively. The average wind speed inside the PE chamber was 2.1 m s^{-1} (see Section 3.2.2 and **Fig. 3.7**).

The measurement system in the outdoor experiments was the same as that explained in Chapter 3. Copper-constantan thermocouples were used to obtain the temperatures in the PE chamber (**Fig. 3.4**). All of the sensing junctions for the thermocouples were connected to one common reference junction. The net radiation was measured using a net radiometer (Q7, Radiation and Energy Balance Systems, Inc., Seattle, United States). The downward and upward shortwave (longwave) radiation were measured using a four-component net radiometer (NR01, Hukseflux, Delftechpark, Netherlands). All the sensor signals as well as the reference

temperatures of the thermocouples were collected using a datalogger (CR-1000, Campbell Scientific, Logan, USA) with a sampling interval of 1 s and an averaging interval of 1 min for recording data. The time necessary for one experiment was 30 min (**Fig. 4.2**). The first 15 min were a spin-up period during which the air and surface temperatures were considered to become stable. The averaged values recorded during the second 15 min were used for the analysis.

The heat flux due to ventilation was calculated from the temperature difference between the inlet and outlet air (ΔT_a) and accounted for the major part of the heat balance components in the PE chamber (see Section 3.4.1). Thus, it is necessary to know the error in ΔT_a between two PE chambers. Thus, two PE chambers with no black Kent paper inserted were placed on the roof at the University of Tsukuba. The daytime data were collected from 09:45 to 17:00 LST on August 7 under both fine and cloudy skies. On the other hand, the nocturnal data were collected from 18:20 to 20:55 LST on August 15, from 18:00 to 19:28 LST on September 26, and from 20:15 to 20:30 LST on September 27, 2013 under clear skies. **Figure 4.3** compares ΔT_a for chambers A and B. The regression line corresponds well to the line of $y = x$. The difference in ΔT_a between the two chambers was concentrated between -0.2°C and +0.2°C (**Fig. 4.4a**), and the root-mean-square error was 0.22°C. In the daytime, the ΔT_a value of chamber A was often -0.2°C to 0°C smaller than that of chamber B (**Fig. 4.4b**). A large difference in ΔT_a between the two chambers appeared under strong downward shortwave radiation (**Fig. 4.5**). The greater variation in the difference in ΔT_a was particularly obvious for downward shortwave radiation of more than 600 W m^{-2}. Okada et al. (1995) measured the vertical profiles of the air temperature and wind speed in a temperature gradient chamber during sunny weather (see Section 3.3). The air temperature increased and the wind speed decreased with height in the chamber under sunny conditions in their measurement. They explained that the incoming cooler air tends to flow near

the ground surface, but once it is heated at the surface, it tends to ascend because of buoyancy. They concluded that the warmer upper air layer flowed backward when the wind speed in the chamber was small. In the PE chamber, the daytime inlet air temperature was also uneven (**Fig. 4.6**). This suggested that backflow might be occurring, and the disturbance in air flow inside the PE chamber was considered to increase under strong solar radiation. Thus, it was preferable to conduct the outdoor experiments in the daytime in cloudy weather, avoiding sunny weather. In the nighttime, on the other hand, the ΔT_a value of chamber A was always bigger than that of chamber B. Its values were very small (less than +0.2°C) (**Fig. 4.4c**).

The daytime experiments described below were conducted during cloudy weather, whereas the nocturnal experiments were conducted on clear nights.

4.2.3 Heat exchange between black Kent paper and surrounding air

To examine the performance of the PE chamber in the evaluation of the heat exchange between a black Kent paper and the surrounding air, two chambers were installed: one with a black Kent paper inside the PE section, and the other without a black Kent paper. The paper was folded in a triangular shape 150 mm wide at its base and 130 mm high (**Fig. 4.7e**). Two papers were placed in parallel inside the PE section, producing a leaf area index (LAI) of 2 for the paper. The paper surface temperatures were measured by copper-constantan thermocouples at the center of each side of the triangle (**Figs. 4.7b**, **e**). The experimental nocturnal heat balance measurements were conducted at Iwate University on March 4, 2013. Further, the experimental daytime heat balance measurements were conducted at the University of Tsukuba on August 2, 2013.

4.2.4 Convective heat exchange at an evaporation surface

The experimental examination of the performance of the PE chamber in the evaluation of the cooling effect of vaporization heat was conducted at the University of Tsukuba on September 10, 11, and 12, 2013 during fine weather. It was very difficult to obtain uniform growth of real vegetation in the PE section. Therefore, instead of real vegetation, we prepared two types of non-woven fabric: wet and dry. We considered the wet non-woven fabric to represent a leaf with all the stomata open, whereas the dry non-woven fabric represented a leaf with all stomata closed. The flat non-woven fabric 450 mm in length and 300 mm in width were suspended at a height of 75 mm with thin wire ($\varphi = 1.0$ mm) and placed in parallel to the floor in the PE section, like the black Kent paper of LAI = 1 (**Fig. 4.8a**). The upper and lower sides of the non-woven fabric were black and white, respectively. At the beginning of the experiment, we supplied water to the wet non-woven fabric and weighed the wet and dry fabrics using an electronic balance (EJ-4100, A&D, Tokyo, Japan). The fabrics were then inserted into each outdoor PE chamber. Both chambers were exposed to the natural atmosphere for about 30 min. Then, we weighed the wet non-woven fabric again and returned it to the PE chamber. This procedure was repeated until the weight of the wet non-woven fabric became the same as that of the dry one (**Fig. 4.9**). To evaluate the latent heat flux at the wet non-woven fabric surface, the evaporation from the wet non-woven fabric was calculated from the difference in the weight of the wet non-woven fabric in the weight before and after the 30 min exposure to air.

4.2.5 Dependence of heat exchange on morphology of heat exchange surface

To examine the dependence of the heat exchange on the area of the heat exchange surface, two chambers for different LAI values were placed on the roof of the building at the University

118

of Tsukuba and compared with each other. **Table 4.1** lists the date, time, and LAI combination compared in each chamber. In this chapter, three different Kent papers were prepared: LAI = 1, 2, and 4 (**Figs. 4.7**, **4.8**). For LAI = 1, flat black Kent papers 450 mm in length and 300 mm in width were suspended at a height of 75 mm with thin wire (φ = 1.0 mm) and placed in parallel to the floor in the PE section (**Fig. 4.8a**). For LAI = 2, black Kent papers were folded in a triangular shape 150 mm wide at its base and 130 mm high and placed in parallel to the floor in the PE section (**Fig. 4.8b**). For LAI = 4, black Kent papers were folded in a triangular shape 75 mm wide at its base and 145 mm high and placed in parallel to the floor in the PE section (**Fig. 4.8c**). The Kent papers with LAI = 1, 2, and 4 were inserted into the PE section near the floor and were not visible from the top. **Figure 4.7** shows the measurement points for the paper surface temperature. The paper surface temperatures for LAI = 2 and 4 were measured by eight thermocouples (φ = 0.3 mm) at the center of each side of the triangle (**Figs. 4.7e**, **f**).

To examine the dependence of the heat exchange on the plant allocation, we prepared gathered and scattered Kent papers. The gathered Kent paper was the same as the Kent paper with LAI = 1 (**Fig. 4.8a**). The scattered Kent paper consisted of 18 pieces of Kent paper 50 mm in length and 300 mm in width. The scattered Kent paper was inserted in two layers; the first and second layers were suspended at a height of 50 mm and 100 mm, respectively (**Fig. 4.10**). **Figure 4.11** shows the measurement points for the paper surface temperature of the scattered Kent paper. The nocturnal heat exchange was measured from 18:50 to 19:04 LST on August 28, 2013 under a clear night sky. The daytime heat exchange was measured from 10:45 to 10:59 LST on August 26, 2013 under cloudy skies.

4.3 Evaluation of heat exchange using the PE chamber

4.3.1 Heat exchange between black Kent paper and surrounding air

In this section, we examine the performance of the PE chamber in the evaluation of the heat exchange between the Kent paper and the surrounding air. Two chambers were installed, one with black Kent paper inside the PE section (LAI = 2, chamber A) and the other without black Kent paper (LAI = 0, chamber B).

First, we examine the temperatures in the PE chamber. **Table 4.2** lists the 15-min averaged values of the air temperature, surface temperature, and temperature differences between the inlet and outlet air in the nighttime and daytime.

In the nighttime, the temperature difference between the inlet and outlet air, ΔT_a, in chamber A was 1.5 times that in chamber B. This indicates clearly that the air was cooled more significantly when the Kent paper was present. Radiative heat was converted to convection at the Kent paper surface in chamber A but at the floor surface in chamber B. The paper surface temperature in chamber A was higher than the floor surface temperature in chamber B, but air cooling was accelerated in chamber A. This trend in the relationship between ΔT_a and the surface temperature was reversed in the daytime. ΔT_a in chamber A was larger than that in chamber B in the daytime. The paper surface temperature in chamber B was lower than the floor surface temperature in chamber A. However, the air passing through chamber A was heated more than that in chamber B. To explain these results physically, the heat balance components in the PE chamber are analyzed below.

Second, we explain how to calculate the heat components in the PE chamber. **Table 4.3** shows the heat balance components in the chamber with and without a Kent paper. The net longwave radiation above the PE film, L^*_a, was measured using a net radiometer. The net

radiation flux at the floor surface, $Q^*_{r\text{-}f}$, in the chamber without a Kent paper and the net radiation flux at the paper surface, $Q^*_{r\text{-}k}$, in the chamber with a Kent paper were obtained from the net radiation flux below the PE film, $Q^*_{r\text{-}b}$, in **Eq. 3.25** or **3.44**. Here, **Eqs. 3.25** and **3.44** are shown again:

$$Q^*_{r-f} = Q^*_{r-b} = A_f L^*_b \tag{3.25}$$

$$Q^*_{r-k} = Q^*_{r-b} = A_f L^*_b \tag{3.44}$$

$Q^*_{r\text{-}b}$ was calculated from **Eqs. 3.29** and **3.48**, which are shown again below:

$$Q^*_{r-f} = Q_v + Q_p + Q_{g-w} + Q_{g-f} \tag{3.29}$$

$$Q^*_{r-k} = Q_v + Q_p + Q_{g-w} + Q_{g-f} \tag{3.48}$$

$Q^*_{r\text{-}f}$ in the chamber with a Kent paper was calculated from **Eq. 3.45**, which is shown again below:

$$Q^*_{r-f} = \varepsilon_f \varepsilon_k \sigma \left(T_k^4 - T_f^4 \right) \tag{3.45}$$

The heat flux due to ventilation, Q_v, conductive heat flux through the sidewalls, $Q_{g\text{-}w}$, and conductive heat flux through the floor, $Q_{g\text{-}f}$, were calculated from **Eqs. 3.32**, **3.30**, and **3.31**, respectively. Here, **Eqs. 3.32**, **3.30**, and **3.31** are shown again:

$$Q_v = \rho c_p V \Delta T_a \tag{3.32}$$

$$Q_{g-w} = A_w \frac{\lambda}{d} \Delta T_w \tag{3.30}$$

$$Q_{g-f} = A_f \frac{\lambda}{d} \Delta T_f \tag{3.31}$$

The heat transmission through the PE film, Q_p, was calculated from **Eq. 3.34** using the heat transmission coefficient, h_t, given by **Eq. 3.41**. Here, **Eqs. 3.34** and **3.41** are shown again:

$$Q_p = A_p h_t \left(T_{in} - T_{out} \right) \tag{3.34}$$

$$h_t = \frac{1}{1/h_{c-in} + 1/h_{c-out}} \tag{3.41}$$

Okada and Hayashi (1983) applied the equation of McAdams (1954) to the convective heat transfer coefficient at the outside surface of a greenhouse's plastic cover and confirmed that this equation was applicable to the evaluation of the heat transmission coefficient. We applied this equation to the convective heat transfer coefficient at the outside surface of the PE cover; namely, $h_{c-out} = 4.2 v_{out} + 6.0$. We also used the coefficient obtained at the Kent paper and/or floor surface for the coefficient h_{c-in} at the inside surface of the PE cover (3.3 W m^{-2} °C^{-1}; see the later part of this section). Substituting an outside wind speed ranging from 1.0 m s^{-1} to 5.0 m s^{-1} into h_{c-out}, we obtained values of the heat transmission coefficient h_t ranging from 4.1 to 5.5 W m^{-2} °C^{-1}. Because h_t did not vary greatly for a wide range of outside wind speeds, we used the value of 4.8 as the heat transmission coefficient.

Third, we compare two approaches to evaluating the convective components Q_{c-f} and Q_{c-k} in

Table 4.3. The first approach is to calculate Q_{c-f} or Q_{c-k} from the heat balance components of the

PE chamber using **Eq. 3.28** or **3.47**, which are shown again below:

$$Q_{c-f} = Q_v + Q_p + Q_{g-w} \tag{3.28}$$

$$Q_{c-f} + Q_{c-k} = Q_v + Q_p + Q_{g-w} \tag{3.47}$$

This approach is unique to the PE chamber technique. The second approach is to calculate

Q_{c-f} or Q_{c-k} as a residual from **Eq. 3.26** or **3.42**, which are shown again below:

$$Q_{r-f}^* = Q_{c-f} + Q_{g-f} \tag{3.26}$$

$$Q_{r-k}^* - Q_{r-f}^* = Q_{c-k} \tag{3.42}$$

The latter values are listed in parentheses in **Table 4.3**. This approach is simple and can be

used outdoors, but it requires the net longwave radiation at the paper or floor surface. In this

study, this approach was not used in the daytime because we could not measure the shortwave

radiation inside and outside of the PE film. Although two different approaches were examined to

evaluate the convective components Q_{c-f} and Q_{c-k}, the results did not differ greatly at night

(**Table 4.3**). The difference between the two approaches arises from the estimation error of the

heat transmission through the film, Q_p. **Figure 4.12** shows a 100% stacked bar chart of Q_v, Q_p,

Q_{g-w}, and Q_{g-f}. Among the convective heat components in **Eqs. 3.28** and **3.48**, the heat flux due

to ventilation, Q_v, amounts to approximately 90% or more of the convective heat components at

the surface, whereas Q_p is 10% or less. The estimation error in the heat transmission component, therefore, does not strongly affect the analysis of the heat exchange at the Kent paper surface in the PE chamber as long as the ventilation component is adequately evaluated.

Fourth, we examine the difference between the heat exchange in the PE chambers with and without a Kent paper. As clearly seen in **Table 4.3**, the radiation loss from the chamber to the sky was larger in chamber A than in chamber B in the nighttime. This is a reasonable consequence of the surface temperature difference inside the two chambers. Namely, in the nighttime, the paper surface temperature in chamber A was higher than the floor surface temperature in chamber B. Hence, the radiation loss caused the heat exchange to switch to convection at the inside surface, thus cooling the inside air. In the daytime, on the other hand, the radiation loss from the chamber to the sky was smaller in chamber B than in chamber A. The paper surface temperature in chamber A was smaller than the floor surface temperature in chamber B. Because the conductive heat flux in the chamber was smaller than that at the inside surface, radiative heat transfer was converted into convection at the inside surface of the chamber. Thus, the decrease in the radiation loss caused the heat exchange to switch to convection at the inside surface, thus heating the inside air. The convective heat flux $Q_{c-f} + Q_{c-k}$ in chamber A was about 1.5 and 1.7 times Q_{c-f} in chamber B in the nighttime and daytime, respectively. This increase is reflected in ΔT_a, as shown in **Table 4.2**.

Finally, we tried to evaluate the convective heat transfer coefficient at the Kent paper surface and floor surface using the following equations. The heterogeneity of the surface temperature in the PE section is lower in the nighttime than in the daytime. Therefore, the convective heat transfer coefficients at the Kent paper surface and floor surface were evaluated only at night.

$$h_{c-k} = Q_{c-k} \Big/ \left\{ \left(T_k - T_a \right) \cdot 4A_f \right\} \tag{4.1}$$

$$h_{c-f} = Q_{c-f} \Big/ \left\{ \left(T_f - T_a \right) \cdot A_f \right\} \tag{4.2}$$

The factor of four appears in **Eq. 4.1** because the paper surface area is twice the floor surface area (e.g., LAI = 2), and both sides of the paper are effective for convective heat exchange. Q_{c-k} and Q_{c-f} were calculated from **Eqs. 3.42** and **3.29** here. The convective heat transfer coefficients calculated for the Kent paper surface and floor surface had the same value of 3.3 W m^{-2} °C^{-1} at night. We used a flat large plate for the leaf model, so it presumably yielded a convective heat transfer coefficient similar to that at the flat floor surface.

4.3.2 Convective heat exchange at an evaporation surface

Hino and Kanda (1989) investigated the effect of plant transpiration using a wind tunnel covered with an acrylic panel. Because the acrylic panel was transparent to shortwave (solar) radiation, the plants inside the tunnel received solar radiation and could transpire. A thin PE film is also transparent to shortwave radiation. Thus, we confirmed whether the PE chamber could evaluate the air cooling effect of vaporization heat.

First, as an example of the measurement results, we show the results obtained on September 11. **Table 4.4** shows the weight of and amount of evaporation from the wet non-woven fabric. The maximum evaporation was 100.7 g when the fabric was supplied with water first. **Table 4.4** indicates that the evaporation decreased as time went on.

Table 4.5 lists the 15-min averaged values of the air temperature, surface temperature, and

temperature difference. The temperature difference between the inlet and outlet air, ΔT_a, in the chamber containing the wet non-woven fabric was smaller than that in the chamber containing the dry non-woven fabric. This indicates that the air traveling in the chamber containing wet non-woven fabric was cooled more. The surface temperature of the wet non-woven fabric was lower than that of the dry non-woven fabric owing to evaporation.

The heat balance equation for the PE chamber containing the wet non-woven fabric, which is similar to **Eq. 3.48**, is written as

$$Q_{r-n}^* = Q_v + Q_p + Q_{g-w} + Q_{g-f} + Q_{e-n} \tag{4.3}$$

where Q_{r-n}^* is the net radiation flux at the non-woven fabric surface, and Q_{e-n} is the latent heat flux at the non-woven fabric surface. Here, the subscript n indicates the non-woven fabric.

Table 4.6 shows the heat balance components in the chambers containing the wet (chamber A) and dry (chamber B) non-woven fabrics. The heat balance components, except for the latent heat flux at the non-woven fabric surface Q_{e-n}, were calculated in the same way as in section 4.3.1 or **Table 4.3**. The latent heat flux at the wet non-woven fabric surface was calculated using the evaporation and latent heat. The latent heat l is given by **Eq. 4.4** (Kondo 1994):

$$l = 2.50 \times 10^6 - 2400 T_{in} \tag{4.4}$$

where T_{in} is the average air temperature in the PE chamber and was calculated using the outlet and inlet temperatures.

The radiation loss from the chamber to the sky was smaller in chamber A than in chamber B (**Table 4.6**). The reduction in the radiation loss is expected to consist of the reduction in the sensible heat flux and the increase in the latent heat flux. The convective heat flux at the non-woven fabric surface, $Q_{c-n} + Q_{c-f}$, was also smaller in chamber A than in chamber B. However, the net radiation above the PE film, L^*_a, differed greatly from that below the film, Q^*_{r-b}, in chamber A. In chamber A, L^*_a was 109.7 W m^{-2}, and Q^*_{r-b} was 64.9 W m^{-2}. During the experiment, condensation below the PE film was often observed in chamber A. This condensation seems to have increased the radiation loss from the chamber.

Next, we examined the cooling effect of the wet non-woven fabric using all the measurement data. **Figure 4.13** shows the relationship between the evaporation from the wet non-woven fabric and the downward shortwave radiation. Strong downward shortwave radiation enhanced the evaporation from the fabric surface. In addition, ΔT_a increased with increasing downward shortwave radiation (**Fig. 4.14**). **Figure 4.15** shows the relationship between the extent of evaporative cooling and the evaporation. The extent of evaporative cooling was calculated by subtracting ΔT_a in the chamber containing the dry non-woven fabric from that in the chamber containing the wet non-woven fabric. Hence, the evaporative cooling was enhanced with increasing evaporation. This indicated that the PE chamber could be used to evaluate the evaporative cooling by weighing a wet object.

4.3.3 Dependence of heat exchange on morphology of heat exchange surface
–4.3.3a Effect of area of heat exchange surface

To examine the dependence of the heat exchange on the area of the heat exchange surface, three experiments were conducted. Namely, we compared the heat exchange in PE chambers

containing Kent papers of LAI = 2 and 1, LAI = 4 and 1, and LAI = 4 and 2 (hereafter referred to as LAI 2–1, LAI 4–1, and LAI 4–2, respectively). We discuss the difference in the heat exchange in the PE chamber using representative results. In the following, the results in the nighttime and daytime are shown, in that order.

Table 4.7 shows the 15-min averaged values of the air temperature, surface temperature, and temperature differences in the nighttime. Comparative experiments with LAI 2–1, LAI 4–1, and LAI 4–2 were conducted on September 27, August 15, and September 27, respectively.

In the comparative experiments with LAI 2–1 and LAI 4–1, the temperature difference between the inlet and outlet air, ΔT_a, in the chamber containing LAI = 4 or 2 was larger than that in the chamber containing LAI = 1. Radiative cooling occurred at the upper surface of the Kent paper, whereas the floor surface did not radiate to the sky. Therefore, the Kent paper surface temperature T_k was smaller than the floor surface temperature T_f in all the comparisons. In addition, T_k in the chamber containing LAI = 4 or 2 was higher than that in the chamber containing LAI = 1. **Table 4.7** indicates that the surface temperature in the chamber containing a larger surface area for heat exchange approached the air temperature in the chamber.

On the other hand, for LAI 4–2, the Kent paper surface temperature for LAI = 4 was also smaller than that for LAI = 2. However, ΔT_a had the same value, -1.0°C, in both chambers. Thus, the increase in the LAI is thought to have gradually decelerated the cooling effect.

Next, we examine these results in terms of the heat balance components in the chamber (**Table 4.8**). Each component in **Table 4.8** was calculated using the procedure described in section 4.3.1. As in section 4.3.1, two approaches were used to calculate the convective heat components Q_{c-f} and Q_{c-k}. The first approach is to calculate Q_{c-f} or Q_{c-k} from the heat balance components of the PE chamber using **Eq. 3.28** or **3.47**. The second approach is to calculate Q_{c-f}

or Q_{c-k} as a residual from **Eq. 3.26** or **3.42**. The values of $Q_{c-f} + Q_{c-k}$ differed to some extent, but their relationship did not change.

For the LAI 2–1 and LAI 4–1 experiments, **Table 4.8** shows that the convective heat transfer by radiation loss increased with increasing area of the heat exchange surface. For example, the net radiation above the PE film, L^*_a, in the chamber containing LAI = 2 was smaller than that in the chamber with LAI = 1. Then, the convective heat flux, $Q_{c-f} + Q_{c-k}$, in the chamber containing LAI = 2 increased to about 1.2 times that in the chamber containing LAI = 1. This increase was reflected in ΔT_a (**Table 4.7**).

On the other hand, in the comparative experiment with LAI 4–2, L^*_a and Q_{c-k} in the chamber containing LAI = 4 were almost the same as those in the chamber containing LAI = 2. However, the paper surface temperature for LAI = 4 was larger than that for LAI = 2 (**Table 4.7**). The upper surfaces of the Kent papers turned gradually toward the sidewall and the neighboring paper's surface and away from the sky as the LAI increased. This difference in the direction of the paper surface is believed to cause an absence of radiative cooling at the paper surface because of multiple reflections of the longwave radiation.

These results indicated that the extended paper surface works like a convector fin installed in an air-conditioning device and enhances convection between the air and the surface (the so-called fin effect). However, the result of the comparative experiment with LAI 4–2 indicated that the fin effect did not increase linearly.

In the daytime, in contrast to the nighttime, the paper surface temperature was increased by solar radiation, becoming greater than the floor surface temperature in each chamber (**Table 4.9**). The paper surface temperature in the chamber containing LAI = 4 or 2 was smaller than that in the chamber containing LAI = 1. On the other hand, ΔT_a in the chamber containing LAI = 4 or 2

was larger than that in the chamber containing LAI = 1. However, there was no substantial change in ΔT_a in the LAI 4–2 comparison. As with the comparison in the nighttime, we speculate that heat exchange gradually slowed as the area of the heat exchange surface increased. **Table 4.10** indicates that the convective heat flux at the paper surface, $Q_{c-f} + Q_{c-k}$, in the chamber containing LAI = 4 or 2 was larger than that in the chamber containing LAI = 1. As in the nighttime, there was no substantial change in ΔT_a in the LAI 4–2 comparison.

Table 4.11 shows the averaged ratios of ΔT_a, T_k, and Q_{c-k} from all the measurement data (**Table 4.1**). The ratios were calculated by dividing the values in the chamber containing the larger LAI by those in the chamber containing the smaller LAI. As with the representative results, ΔT_a in the chamber containing the larger LAI was larger than that in the chamber containing the smaller LAI in both the nighttime and the daytime. In addition, **Table 4.11** shows a similar relationship between the paper surface temperature and the LAI to that from the representative results. In the nighttime, the paper surface temperature of larger-LAI paper was higher than that of smaller-LAI paper. In the daytime, on the other hand, the paper surface temperature of larger-LAI paper was smaller than that of smaller-LAI paper. The change in the radiation loss was a driving force of convective heat transfer at the paper surface, thus accelerating the cooling of air in the nighttime and heating of air in the daytime. **Table 4.11** also indicated that there was no substantial difference between ΔT_a in the chambers containing LAI = 2 and 4. This indicates that the fin effect decreased gradually as the area of the heat exchange surface increased.

–4.3.3b Effect of characteristic length

To examine the dependence of the heat exchange on the plant allocation, we installed two chambers with different allocations: gathered Kent paper and scattered Kent paper. The characteristic length of the scattered Kent paper was shorter than that of the gathered Kent paper.

Table 4.12 shows the results for the air temperature, surface temperature, and temperature difference. In the daytime, the scattered Kent paper exhibited a lower paper surface temperature and higher ΔT_a. The convective heat flux, $Q_{c\text{-}f} + Q_{c\text{-}k}$, in the chamber containing the scattered Kent paper was larger than that in the chamber containing the gathered Kent paper in the daytime (**Table 4.13**). These results were similar to those for the dependence of the heat exchange on the LAI (**Tables 4.7–4.11**). On the other hand, in the nighttime, there were smaller differences in ΔT_a and the convective heat flux between the chambers containing the scattered and gathered Kent paper.

As in section 4.3.1, we tried to evaluate the convective heat transfer coefficient $h_{c\text{-}k}$ at the surfaces of the scattered and gathered Kent paper. In the daytime, $h_{c\text{-}k}$ at the surfaces of the scattered and gathered Kent paper was 8.5 W m^{-2} °C^{-1} and 6.2 W m^{-2} °C^{-1}, respectively. In the nighttime, on the other hand, $h_{c\text{-}k}$ for the scattered and gathered Kent paper was 1.6 W m^{-2} °C^{-1} and 1.4 W m^{-2} °C^{-1}, respectively. The thermal boundary layer is thinner at a surface with a shorter characteristic length. This thinner thermal boundary layer enhances the convective heat transfer at the Kent paper surface. Hence, the scattered heat exchange surface heightens the fin effect as well as a large heat exchange surface does. In the experiments in the PE chamber, the fin effect caused by the scattered heat exchange surface appeared more clearly in the daytime than in the nighttime. The net energy in the chamber is believed to have differed between the daytime and the nighttime.

4.4 Discussion

The advantage of the PE chamber is its applicability for evaluating nocturnal heat exchange systems. The radiation level in the PE chamber is almost equivalent to that outdoors because the

thin PE film transmits shortwave and longwave radiation well. The results demonstrated that the change in the radiation loss from the inside surface of the chamber to the sky caused a switch to convective heat exchange. Here, let us consider the extreme case. The paper surface temperature approaches the air temperature infinitely when the convective heat transfer is ultimately enhanced. The air surrounding the paper is thus not cooled under this condition. However, the results shown in this chapter indicated that the fin effect of the Kent paper increased nonlinearly with increasing area of the heat exchange surface. In the following, we discuss the nocturnal heat exchange system in terms of the vegetation size and allocation using a simple equation for the heat balance in the PE chamber.

First, we explain the simple heat balance equation. Here, we assume that a flat Kent paper is inserted into the PE chamber (**Fig. 3.16**). The heat exchange system at the Kent paper surface in the PE chamber is expressed by three equations: the heat balance in a volume (**Eq. 3.47**), the radiation balance at the Kent paper surface (**Eq. 3.42**), and the radiation balance at the floor surface (**Eq. 3.26**).

The PE chamber is elevated above the ground surface (assumption 3, described in section 3.3). Thus, the conductive heat flux at the floor surface, $Q_{g\text{-}f}$, can be assumed to be negligibly small in **Eq. 3.26**, and is actually very small compared to the other heat components (e.g., **Tables 4.3**, **4.8**). The net radiation at the floor surface, $Q^{*}_{r\text{-}f}$, was also negligibly small. Therefore, the convective heat flux at the floor surface, $Q_{c\text{-}f}$, can be considered to be small. Next, we consider the convective heat exchange at the flat Kent paper surface. The convective heat flux at the paper surface, $Q_{c\text{-}k}$, is calculated using **Eq. 3.47**. As seen in **Table 4.3**, $Q_{c\text{-}f}$, Q_{p}, and $Q_{g\text{-}w}$ are smaller than $Q_{c\text{-}k}$ and Q_{v}. Thus, it can be assumed that the convective heat flux at the paper surface balances the heat flux due to ventilation (**Eq. 4.5**).

$$g_H \left(T_{in} - T_k \right) = g_V \left(T_{inlet} - T_{outlet} \right) \tag{4.5}$$

where g_H is the convective heat transfer conductance, which is obtained by multiplying the convective heat transfer coefficient and the heat exchange surface area, that is, the LAI (**Eq. 4.6**). Further, g_V is the ventilation heat transfer conductance, which is obtained by multiplying the heat capacity and the ventilation rate per unit area (**Eq. 4.7**).

$$g_H = 2h_{c-k} \cdot LAI \tag{4.6}$$

$$g_V = \rho c_p V / A_f \tag{4.7}$$

The factor of two appears in **Eq. 4.6** because both sides of the Kent paper are effective for convective heat exchange.

In the radiation balance at the Kent paper surface (**Eq. 3.42**), Q^*_{r-f} is smaller than Q^*_{r-k} and Q_{c-k}, as seen in **Table 4.3**. Therefore, it can be assumed that the radiative heat transfer at the Kent paper surface balances the convective heat transfer at the Kent paper surface (**Eq. 4.8**). The radiative heat transfer is expressed by the linearization of the temperature, as in **Eq. 3.35**.

$$g_R \left(T_{sky} - T_k \right) = g_H \left(T_{in} - T_k \right) \tag{4.8}$$

where g_R is the radiative heat transfer conductance, which is given by the first term linearized by a Taylor expansion (**Eq. 4.9**).

$$g_R \approx 4\sigma T_{sky}^3 \qquad (4.9)$$

From **Eqs. 4.5** and **4.8**, the simple heat balance equation is expressed as a balance between the radiative heat transfer, convective heat transfer, and ventilation heat transfer (**Eq. 4.10**).

$$g_R\left(T_{sky} - T_k\right) = g_H\left(T_{in} - T_k\right) = g_V\left(T_{inlet} - T_{outlet}\right) \qquad (4.10)$$

In the derivation of **Eq. 4.10**, we assumed that the heat transmission through the PE film, Q_p, and conductive heat flux through the floor, Q_{g-f}, were negligibly small in **Eq. 3.47**. The convective heat transfer (and ventilation heat transfer) in **Eq. 4.5** were originally determined from Q_p and Q_{g-f}. Note that as a result, strictly speaking, the convective heat transfer in **Eq. 4.5** is not the same as that in **Eq. 4.8**.

Second, the difference in the convergence temperature between the paper and the air is discussed by rearranging the simple heat balance equation. We assume here that the air temperature in the chamber changes linearly from the inlet to the outlet [$T_{in} = (T_{inlet} + T_{outlet})/2$]. The paper surface temperature is obtained by rearranging the convective heat transfer and ventilation heat transfer terms in **Eq. 4.10**:

$$T_k = \frac{\left(g_H - 2g_V\right)T_{inlet} + \left(g_H + 2g_V\right)T_{outlet}}{2g_H} \qquad (4.11)$$

From the radiative heat transfer and convective heat transfer terms in **Eq. 4.10**, the Kent

paper surface temperature is obtained as follows:

$$T_k = \frac{g_V\left(T_{inlet} - T_{outlet}\right) + g_R T_{sky}}{g_R}$$

(4.12)

The outlet air temperature is obtained by substituting **Eq. 4.12** into **Eq. 4.11**.

$$T_{outlet} = \frac{\left(2g_V g_H + 2g_V g_R - g_H g_R\right)T_{inlet} + 2g_H g_R T_{sky}}{2g_V g_H + g_H g_R + 2g_V g_R}$$

(4.13)

Suppose that the convective heat transfer is infinite in **Eq. 4.13** ($g_H \rightarrow \infty$):

$$T_{outlet} = \frac{\left(2g_V - g_R\right)T_{inlet} + 2g_R T_{sky}}{2g_V + g_R}$$

(4.14)

Equation 4.14 indicates that the ventilation rate and sky temperature determine the convergence temperature of the outlet air. Hence, at a higher sky temperature, there was no substantial change in the temperature difference (**Tables 4.7**, **4.12**)

Next, we consider the convergence temperature of the Kent paper surface. The outlet air temperature is rearranged using the ventilation heat transfer and convective heat transfer terms in **Eq. 4.10** (**Eq. 4.15**).

$$T_{outlet} = \frac{\left(2g_V - g_H\right)T_{inlet} + 2g_H T_k}{2g_V + g_R}$$

(4.15)

From the radiative heat transfer and ventilation heat transfer terms in **Eq. 4.10**, the outlet air

135

temperature is obtained as follows:

$$T_{outlet} = \frac{g_V T_{inlet} + g_R \left(T_{sky} - T_k\right)}{g_V}$$

(4.16)

The Kent paper surface temperature is obtained by substituting **Eq. 4.15** into **Eq. 4.14**.

$$T_m = \frac{2g_V g_H T_{inlet} + \left(2g_V g_R + g_H g_R\right)T_{sky}}{2g_V g_H + 2g_V g_R + g_H g_R}$$

(4.17)

Suppose that the convective heat transfer is infinite in **Eq. 4.17** ($g_H \rightarrow \infty$):

$$T_k = \frac{2g_V T_{inlet} + g_R T_{sky}}{2g_V + g_R}$$

(4.18)

Equation 4.18 indicates that the ventilation rate and sky temperature also determine the convergence temperature of the Kent paper surface. A comparison with **Eq. 4.14** reveals that the dominant factors for the Kent paper surface temperature are the same as those for the outlet air temperature. However, the convergence temperatures of the outlet air and Kent paper surface differ slightly. If the ventilation heat transfer term in **Eq. 4.10** is removed, the Kent paper surface temperature equals the air temperature in the chamber, so the air in the chamber is not cooled. Thus, **Eq. 4.10** reveals the significance of the ventilation heat transfer for understanding heat exchange systems.

Third, we examine the dependence of the fin effect of the Kent paper on the LAI using the simple heat balance equation. Using the experimental results from September 27, 2013, the

outlet air temperature and Kent paper surface temperature were calculated from **Eqs. 4.14** and **4.18**, respectively. In the calculation, we varied the LAI from 0 to 10 in **Eq. 4.6**. **Figure 4.16** shows the dependence of the Kent paper surface temperature and outlet air temperature on the LAI. The outlet air temperature approached the Kent paper surface temperature nonlinearly with increasing LAI. This indicates that the Kent paper acts as a converter fin for cooling air because the inlet air temperature was a fixed value in the calculation. Additionally, **Fig. 4.16** indicates that the fin effect for cooling air decreased gradually as the area of the heat exchange surface increased. The air traveling in the chamber was cooled little beyond LAI = 2. In the results from the PE chamber, on the other hand, the fin effect of the Kent paper reached a plateau between LAI = 1 and LAI = 4 (**Table 4.11**). The LAI at which the fin effect decreased differed slightly between the simple heat balance equation and the results from the PE chamber. The assumption that Q_p and Q_{g-f} can be neglected in **Eq. 3.47** seems to affect this slight difference.

Finally, we examine the dependence of the fin effect of the Kent paper on the characteristic length using the simple heat balance equation. Using the same results mentioned above, the outlet air temperature and Kent paper surface temperature were calculated from **Eqs. 4.14** and **4.18**, respectively. The convective heat transfer varies inversely with the characteristic length, and its calculation requires the Reynolds number and Prandtl number (Campbell and Norman 1998). However, we could not obtain these dimensionless groups from the PE chamber, so we changed the convective heat transfer coefficient from 1.0 to 9.0 in **Eq. 4.6**. We considered here that an increase in the convective heat transfer coefficient represented a decrease in the characteristic length for certain dimensionless groups. **Figure 4.17** shows the dependence of the outlet air temperature on the convective heat transfer coefficient. The outlet air temperature decreased nonlinearly with increasing convective heat transfer coefficient. This indicates that the

fin effect for nocturnal cooling of air increased nonlinearly as the characteristic length decreased. In the thermal boundary layer theory, the thermal boundary layer on a smaller object is thinner than that on a larger object. Therefore, convective heat exchange between the small object's surface and the surrounding air is enhanced. Sakai et al. (2012) explained this effect well using black metal plates of different sizes. They installed five black metal plates horizontally at a height of approximately 1.5 m from a building's roof in the daytime and found that the temperature of the larger plate was always higher than that of the smaller one. In the PE chamber, scattering the Kent paper also decreased the Kent paper surface temperature (**Table 4.12**).

Here, we described the system of nocturnal heat exchange between the Kent paper surface and the surrounding air using a simple heat balance equation. This equation explained well the significance of the ventilation heat transfer for determining the convergence temperatures of the outlet air and Kent paper surface. In addition, it explained well the fin effect of the heat exchange surface morphology in cooling of air. These results from the simple heat balance equation indicate that the results from the PE chamber were reasonable.

4.5 Summary

In this chapter, we conducted two preliminary PE chamber experiments that evaluated 1) its performance in heat exchange evaluation and 2) its performance in evaluation of the cooling effect at the evaporation surface. Our findings are summarized as follows:

Preliminary experiment 1: Performance in heat exchange evaluation
- Two approaches could be used to evaluate the convective heat flux in the PE chamber. Both approaches yielded similar values of the convective heat flux at the inside surface of the PE

chamber under clear night skies.

- In the nighttime, the installation of Kent paper in the chamber increased the radiation loss from the surface of the chamber to the sky. This radiation loss increased the heat exchange between the air and the inside surface of the chamber. As a result, heat from the air was absorbed by the inside surface of the chamber via convective heat exchange. In other words, the air traveling in the chamber with the Kent paper was cooled more effectively than that in the chamber without it (**Fig. 4.18**). These results indicate that the colder surface did not necessarily produce greater cooling of the surrounding air.

- In the daytime, installation of the Kent paper in the chamber decreased the radiation loss from the surface of the chamber to the sky. The solar energy input to the chamber was divided into the decrease in the radiation loss and the increase in the convective heat exchange. As a result, the air traveling in the chamber with the paper was heated more effectively than that in the chamber without it.

Preliminary experiment 2: Performance in evaluation of the cooling effect at the evaporation surface

- Installation of wet non-woven fabric in the chamber decreased the heating of air.

- The wet non-woven fabric was weighed to evaluate the latent heat flux at its surface. A comparison of the wet and dry non-woven fabric indicated that the evaporative cooling was remarkable with increasing latent heat flux.

Next, to examine the dependence of the heat exchange on the vegetation morphology, we varied the area of the heat exchange surface and the characteristic length in the PE chamber. Our findings are summarized as follows:

139

Experiment 1: Varying the area of the heat exchange surface

- Increasing the area of the heat exchange surface (the LAI) increased (decreased) the radiation loss from the paper surface in the chamber during the nighttime (daytime). This change in the radiation loss caused the heat exchange to switch to convection at the paper surface. The enhanced convective heat transfer accelerated nighttime cooling or daytime heating of air. Hence, increasing the area of the heat exchange surface enhanced the fin effect.

- The fin effect was enhanced nonlinearly with an increase in the area of the heat exchange surface.

Experiment 2: Varying the characteristic length

- Decreasing the characteristic length increased the convective heat transfer coefficient at the Kent paper surface. This increase in the convective heat transfer coefficient indicated enhanced convective heat exchange at the Kent paper surface. The enhanced convective heat transfer accelerated nighttime cooling or daytime heating of air. Hence, decreasing the characteristic length enhanced the fin effect.

- A simple heat balance analysis of the PE chamber indicated that the fin effect caused by a scattered the heat exchange surface was nonlinearly enhanced.

Table 4.1. Experiment date and place, and the comparing comparison of LAI. The experiments were conducted in Graduate School of Life and Environmental Sciences, the University of Tsukuba, Tsukuba, Japan.

Date	Time (LST)	Comparison of LAI
2013.08.05	13:00 – 13:30	4 (chamber A), 1 (chamber B)
	14:00 – 14:30	1 (chamber A), 2 (chamber B)
	15:45 – 16:15	2 (chamber A), 4 (chamber B)
2013.08.09	13:10 – 13:40	4 (chamber A), 1 (chamber B)
	13:50 – 14:20	2 (chamber A), 1 (chamber B)
	14:35 – 15:00	4 (chamber A), 2 (chamber B)
2013.08.14	10:20 – 10:50	4 (chamber A), 2 (chamber B)
	12:40 – 13:10	4 (chamber A), 1 (chamber B)
	13:25 – 13:55	2 (chamber A), 1 (chamber B)
	19:35 – 20:05	1 (chamber A), 4 (chamber B)
2013.08.15	19:15 – 19:45	4 (chamber A), 2 (chamber B)
	19:55 – 20:25	4 (chamber A), 1 (chamber B)
2013.09.10	18:50 – 19:20	2 (chamber A), 1 (chamber B)
2013.09.20	18:00 – 18:30	2 (chamber A), 1 (chamber B)
2013.09.24	17:45 – 18:15	2 (chamber A), 4 (chamber B)
2013.09.27	18:45 – 19:15	2 (chamber A), 4 (chamber B)
	19:25 – 19:55	2 (chamber A), 1 (chamber B)

Table 4.2. Comparison of the air and surface temperatures and the temperature differences in each chamber with and without the black Kent paper. The temperature difference between the inlet and outlet air, ΔT_a, was calculated from subtracting the outlet air temperature, T_{outlet}, from the inlet air temperature, T_{inlet}. The temperature difference between the inside and the outside surfaces of the extruded polystyrene foam panel at the floor or the sidewall, ΔT_w and ΔT_f, was measured using a thermocouple. The alphabet in the parentheses means the chamber identification.

(°C)

	Nighttime (2013.03.04)		Daytime (2013.08.02)	
LAI	2 (A)	0 (B)	2 (B)	0 (A)
T_{outlet}	-0.79	-0.45	31.5	29.3
T_{inlet}	0.48	0.42	25.1	25.6
ΔT_a	-1.28	-0.87	6.38	3.68
T_f	-2.0	-9.0	32.8	49.1
T_k	-3.5		37.4	
ΔT_w	0.01	0.05	3.49	4.16
ΔT_f	-2.61	-7.67	4.82	19.2

Table 4.3. Comparison of the heat balance components in the chambers with and without a Kent paper in the nighttime and daytime. The values in the parentheses for Q_{c-f} or Q_{c-k} were calculated from **Eqs. 3.26** or **3.42** using the net longwave radiation Q^*_{r-f} and/or Q^*_{r-k}. The values in the parentheses for Q_p were calculated as a residual of **Eqs. 3.29** or **3.48**. Asterisks written with the values of L^*_a mean the measurement values. The alphabet in the parentheses means the chamber identification.

	Nighttime (2013.03.04)		Daytime (2013.08.02)	
LAI	2 (A)	0 (B)	2 (B)	0 (A)
L^*_a [W m^{-2}]	-57.6*	-45.4*	277.6*	236.4*
Q^*_{r-f} [W]	-1.9	-11.5	6.0	46.0
Q^*_{r-k} [W]	-13.7		67.3	
Q_{c-f} [W]	-1.0	-8.7(-8.1)	4.2	39.0
Q_{c-k} [W]	-11.8(-12.6)		61.3	
Q_v [W]	-11.6	-7.9	57.7	33.3
Q_p [W]	-1.2(-2.0)	-0.8(-0.2)	5.8	3.4
Q_{g-w} [W]	-0.03	-0.004	1.9	2.3
Q_{g-f} [W]	-1.0	-2.8	1.8	7.0

Table 4.4. Lsits of the weight of the wet fabric and the amount of evaporation. The evaporation was calculated from the difference of the weight of the wet non-woven fabric every 30 minutes.

Time (LST)	Weight of the wet non-woven fabric [g]	Evaporation [g]
10:10	438.3	
10:40 - 10:50	337.6	100.7
11:20 - 11:30	269.4	68.2
12:00 - 12:05	200.1	69.3
12:35 - 12:40	140.2	59.9
13:10 - 13:15	95.0	45.2
13:45 - 13:50	74.0	21.0
14:20	66.4	7.6

Table 4.5. Comparison of the air temperatures, surface temperatures and the temperature differences in the chamber with wet and dry non-woven fabric. The experiment was conducted from 10:10 to 10:40 LST on September 11th, 2013. The temperature difference between the inlet and outlet air, ΔT_a, was calculated from subtracting the outlet air temperature, T_{outlet}, from the inlet air temperature, T_{inlet}. The temperature difference between the inside and the outside surfaces of the extruded polystyrene foam panel at the floor or the sidewall, ΔT_w and ΔT_f, was measured using a thermocouple. The alphabet in the parentheses means the chamber identification.

(°C)

	wet non-woven fabric (A)	dry non-woven fabric (B)
T_{outlet}	30.7	35.1
T_{inlet}	28.2	28.8
ΔT_a	2.5	6.3
T_f	33.4	41.7
T_n	35.8	47.0
ΔT_w	3.04	8.73
ΔT_f	3.02	11.3

Table 4.6. Comparison of the heat balance components in the chambers with wet and dry non-woven fabric. The experiment was conducted from 10:10 to 10:40 LST on September 11th, 2013. Asterisks written with the values of L^{*}_{a} mean the measurement values. The alphabet in the parentheses means the chamber identification.

	wet non-woven fabric (A)	dry non-woven fabric (B)
L^{*}_{a} [W m^{-2}]	401.8*	329.7*
$Q^{*}_{r\text{-}f}$ [W]	9.5	23.7
$Q^{*}_{r\text{-}n}$ [W]	64.9	69.7
$Q_{c\text{-}f}$ [W]	-10.6	-27.8
$Q_{c\text{-}n}$ [W]	36.4	93.4
Q_{v} [W]	22.7	57.1
Q_{p} [W]	1.4	3.6
$Q_{g\text{-}w}$ [W]	1.7	4.9
$Q_{g\text{-}f}$ [W]	1.1	4.1
$Q_{e\text{-}n}$ [W]	37.1	

Table 4.7. Comparison of the air temperatures, surface temperatures and the temperature differences in the chamber at night. The experiments for LAI 2–1, LAI 4–1, and LAI 4–2 were conducted on September 27th, August 15th, September 27th, respectively. The temperature difference between the inlet and outlet air, ΔT_a, was calculated from subtracting the outlet air temperature, T_{outlet}, from the inlet air temperature, T_{inlet}. The temperature difference between the inside and the outside surfaces of the extruded polystyrene foam panel at the floor or the sidewall, ΔT_w and ΔT_f, was measured using a thermocouple. The alphabet in the parentheses means the chamber identification.

(°C)

Date	September 27th		August 15th		September 27th	
LAI	2 (A)	1 (B)	4 (A)	1 (B)	4 (B)	2 (A)
T_{outlet}	14.9	15.2	27.6	27.8	15.4	15.3
T_{inlet}	15.9	16.0	28.5	28.5	16.4	16.3
ΔT_a	-1.0	-0.8	-0.9	-0.7	-1.0	-1.0
T_f	13.8	13.9	27.8	27.0	15.2	14.4
T_k	12.5	12.2	27.5	25.8	14.6	13.0
ΔT_w	-0.4	-0.8	0.1	-0.4	-0.6	-0.4
ΔT_f	-2.6	-2.2	-0.6	-1.0	-1.4	-2.4

Table 4.8. Comparison of the heat balance components in the chamber at night. The experiments for LAI 2–1, LAI 4–1, and LAI 4–2 were conducted on September 27th, August 15th, September 27th, respectively. The values in the parentheses for $Q_{c\text{-}f}$ or $Q_{c\text{-}k}$ were calculated from **Eqs. 3.26** or **3.42** using the net longwave radiation $Q^{*}_{r\text{-}f}$ and/or $Q^{*}_{r\text{-}k}$. The values in the parentheses for Q_p were calculated as a residual of **Eqs. 3.29** or **3.48**. Asterisks written with the values of L^{*}_{a} mean the measurement values. The alphabet in the parentheses means the chamber identification.

Date	September 27th		August 15th		September 27th	
LAI	2 (A)	1 (B)	4 (A)	1 (B)	4 (B)	2 (A)
L^{*}_{a} [W m^{-2}]	-45.5*	-41.2*	-37.1*	-30.6*	-47.9*	-47.9*
$Q^{*}_{r\text{-}f}$ [W]	-2.0	-2.5	-1.5	-2.5	-1.1	-2.0
$Q^{*}_{r\text{-}k}$ [W]	-6.0	-5.0	-8.4	-7.9	-12.0	-12.0
$Q_{c\text{-}f}$ [W]	-1.1	-1.6	-1.3	-2.1	-1.3	-2.1
$Q_{c\text{-}k}$ [W]	-9.4(-9.6)	-6.9(-7.8)	-6.9(-8.0)	-5.5(-5.1)	-10.1(-10.9)	-10.0(-8.9)
Q_{v} [W]	-9.3	-7.4	-7.5	-6.7	-9.4	-8.9
Q_{p} [W]	-0.9(-1.2)	-0.7(-1.6)	-0.8(-1.8)	-0.7(-0.3)	-0.9(-1.7)	-0.9(-2.0)
$Q_{g\text{-}w}$ [W]	-0.2	-0.4	0.0	-0.2	0.0	-0.2
$Q_{g\text{-}f}$ [W]	-0.9	-0.8	-0.2	-0.4	-0.2	-0.4

Table 4.9. Comparison of the air temperatures, surface temperatures and the temperature differences in the chamber in the daytime. The experiments for LAI 2–1, LAI 4–1, and LAI 4–2 were conducted on August 14th, August 14th, August 9th, respectively. The temperature difference between the inlet and outlet air, ΔT_a, was calculated from subtracting the outlet air temperature, T_{outlet}, from the inlet air temperature, T_{inlet}. The temperature difference between the inside and the outside surfaces of the extruded polystyrene foam panel at the floor or the sidewall, ΔT_w and ΔT_f, was measured using a thermocouple. The alphabet in the parentheses means the chamber identification.

(°C)

Date	August 14th		August 14th		August 9th	
LAI	2 (A)	1 (B)	4 (A)	1 (B)	4 (A)	2 (B)
T_{outlet}	44.0	42.9	46.6	44.6	41.3	41.1
T_{inlet}	33.2	33.7	33.4	34.1	34.5	34.5
ΔT_a	10.8	9.2	13.2	10.5	6.8	6.6
T_f	46.6	48.9	42.5	52.6	39.7	42.2
T_k	54.1	55.2	50.1	60.6	41.6	46.2
ΔT_w	7.4	6.5	6.1	7.3	2.6	2.6
ΔT_f	9.8	12.1	7.0	15.0	2.8	5.3

Table 4.10. Comparison of the heat balance components in the chamber in the daytime. The experiments for LAI 2–1, LAI 4–1, and LAI 4–2 were conducted on August 14th, August 14th, August 9th, respectively. Asterisks written with the values of L^*_a mean the measurement values. The alphabet in the parentheses means the chamber identification.

Date	August 14th		August 14th		August 9th	
LAI	2 (A)	1 (B)	4 (A)	1 (B)	4 (A)	2 (B)
L^*_a [W m^{-2}]	454.0*	431.7*	569.4*	515.2*	236.8*	230.0*
$Q^*_{r\text{-}f}$ [W]	12.1	10.2	11.9	13.8	1.8	5.4
$Q^*_{r\text{-}k}$ [W]	115.5	100.2	137.4	114.4	143.6	138.4
$Q_{c\text{-}f}$ [W]	8.7	5.8	9.3	8.4	0.9	3.5
$Q_{c\text{-}k}$ [W]	103.2	90.1	125.5	100.6	68.3	64.1
Q_v [W]	97.9	83.7	119.3	95.2	61.5	60.0
Q_p [W]	9.9	8.5	12.1	9.6	6.2	6.1
$Q_{g\text{-}w}$ [W]	4.1	3.6	3.4	4.1	1.4	1.6
$Q_{g\text{-}f}$ [W]	3.6	4.4	2.6	5.5	1.0	1.9

Table 4.11. Average ratio of the temperature difference, ΔT_a, the paper surface temperature, T_k, and the convective heat transfer at the paper surface, $Q_{c\text{-}k}$, in the nighttime (a) and daytime (b). The ratios were calculated from dividing the values in the chamber with larger-LAI paper by those in the chamber with smaller-LAI paper.

(a)

	ΔT_a	T_k	$Q_{c\text{-}k}$
LAI 2 – 1	1.19	1.04	1.40
LAI 4 – 1	1.12	1.07	1.25
LAI 4 – 2	1.03	1.07	1.03

(b)

	ΔT_a	T_k	$Q_{c\text{-}k}$
LAI 2 – 1	1.15	0.94	1.12
LAI 4 – 1	1.28	0.80	1.30
LAI 4 – 2	1.05	0.88	1.15

Table 4.12. Comparison of the air temperatures, surface temperatures, and the temperature differences in each chamber with the scattered and gathered Kent paper. The measurement in the nighttime was conducted from 18:50 to 19:04 LST on August 28th. The measurement in the daytime was conducted from 10:45 to 10:59 LST on August 26th. The temperature difference between the inlet and outlet air, ΔT_a, was calculated from subtracting the outlet air temperature, T_{outlet}, from the inlet air temperature, T_{inlet}. The temperature difference between the inside and the outside surfaces of the extruded polystyrene foam panel at the floor or the sidewall, ΔT_w and ΔT_f, was measured using a thermocouple. The alphabet in the parentheses means the chamber identification.

(°C)

	Nighttime (2013.08.28)		Daytime (2013.08.26)	
	Scattered (A)	Gathered (B)	Scattered (B)	Gathered (A)
T_{outlet}	25.6	25.6	43.4	41.7
T_{inlet}	26.3	26.2	31.3	31.3
ΔT_a	-0.69	-0.59	12.1	10.4
T_f	24.8	24.7	49.6	53.2
T_k	24.1	23.3	60.6	65.9
ΔT_w	-0.41	-0.54	6.84	14.51
ΔT_f	-1.36	-1.55	11.03	16.46

Table 4.13. Comparison of the heat balance components in the chambers with the scattered and gathered Kent paper. The measurement in the nighttime was conducted from 18:50 to 19:04 LST on August 28th. The measurement in the daytime was conducted from 10:45 to 10:59 LST on August 26th. The values of Q^*_{r-b} were calculated from the sum of Q_v, Q_p, Q_{g-w} and Q_{g-f}. Asterisks written with the values of L^*_a mean the measurement values. The alphabet in the parentheses means the chamber identification.

	Nighttime (2013.08.28)		Daytime (2013.08.26)	
	Scattered (A)	Gathered (B)	Scattered (B)	Gathered (A)
L^*_a [W m^{-2}]	-26.2*	-24.8*	556.3*	519.7*
Q^*_{r-f} [W]	-0.8	-2.7	20.2	17.9
Q^*_{r-k} [W]	-7.6	-6.8	128.3	117.4
Q_{c-f} [W]	-0.3	-2.2	16.2	11.9
Q_{c-k} [W]	-6.8	-4.0	108.0	99.5
Q_v [W]	-6.2	-5.4	109.4	93.9
Q_p [W]	-0.6	-0.5	11.1	9.5
Q_{g-w} [W]	-0.2	-0.3	3.8	8.1
Q_{g-f} [W]	-0.5	-0.6	4.0	6.0
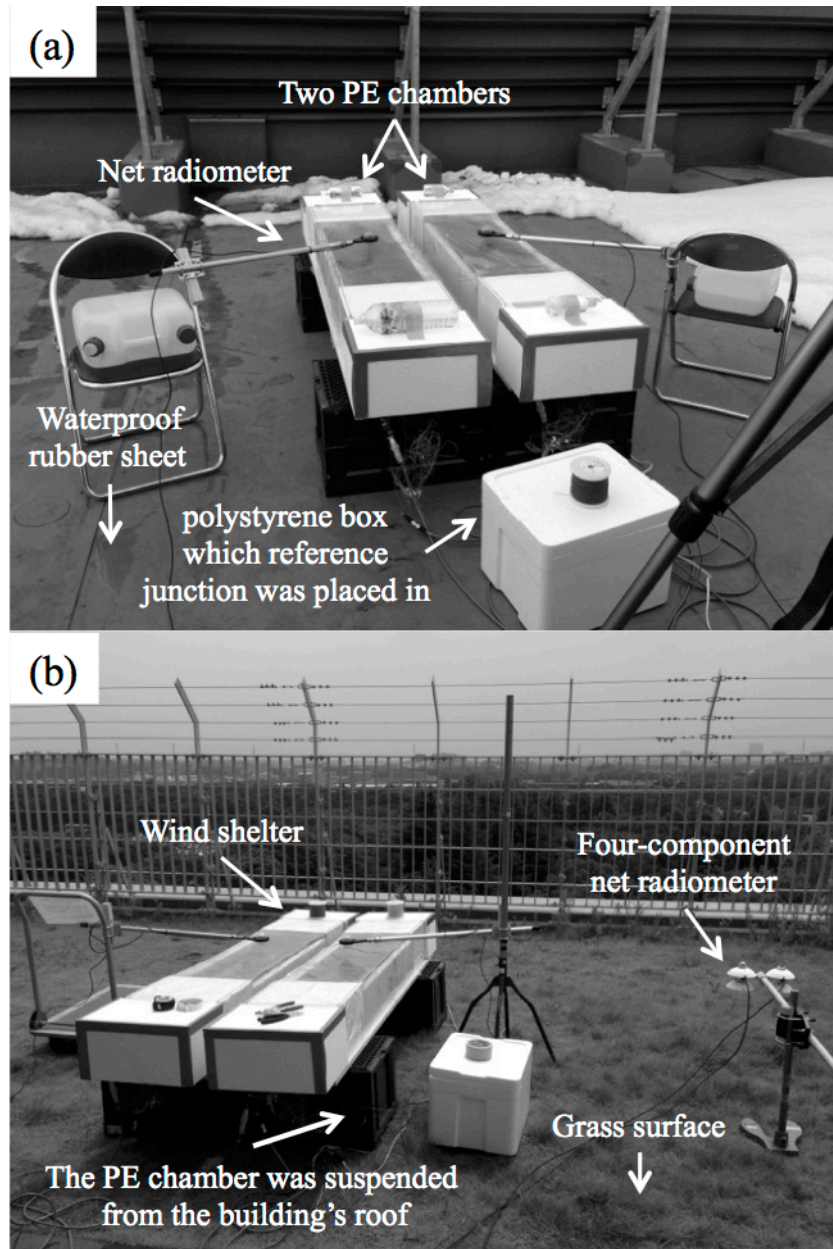
Fig. 4.1. View of the outdoor measurement for heat exchange using the PE chamber in Iwate University (a), in the University of Tsukuba (b). The roof surface was covered with the waterproof rubber sheet in Iwate University, and the grass in the University of Tsukuba, respectively. All of the sensing junctions for thermocouples were connected to one common reference junction. Net radiation above the PE film was measured by a net radiometer. Downward shortwave and longwave radiation were measured by four-component net radiometer.

154

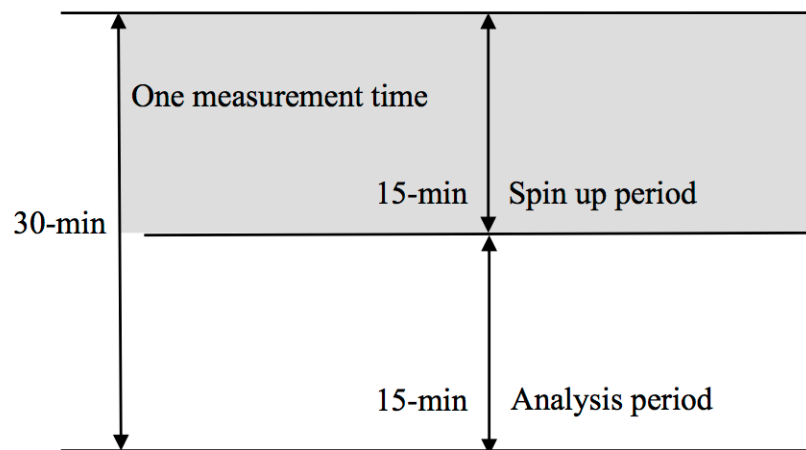Fig. 4.2. Schematic of the measurement period in the outdoor experiments using the PE chamber. One experiment period was 30-min. The former 15-min was the spin up period when the air and surface temperatures were considered to become stable. The latter 15-min was the analysis period. The 15-min averaged values were used in the analysis.
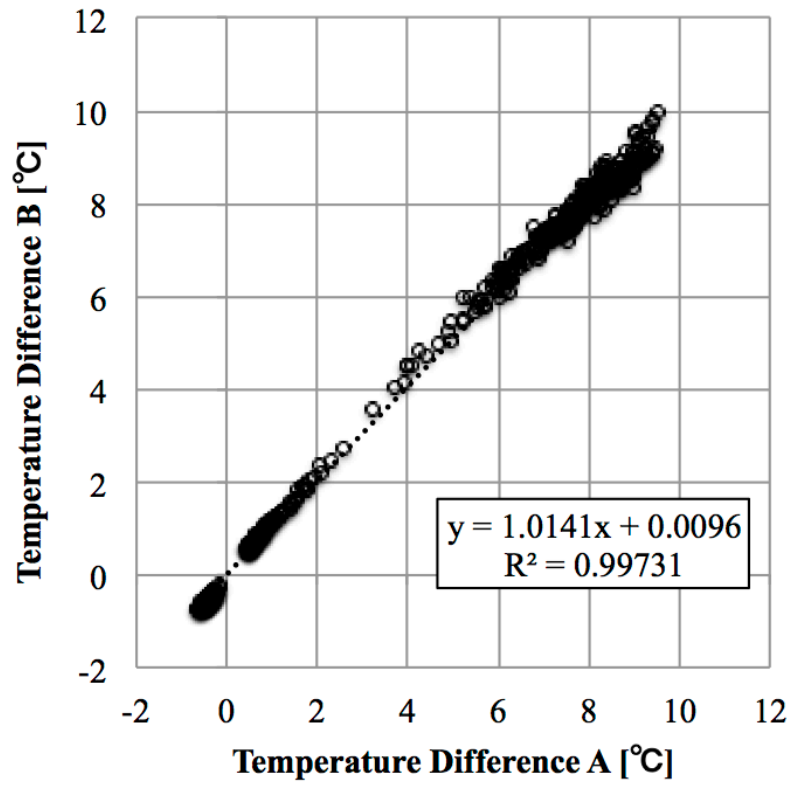
Fig. 4.3. Comparison of the temperature difference between the chamber A and the chamber B, ΔT_a. The comparing experiment was conducted on the building's roof of the University of Tsukuba. In the experiment, two PE chambers without inserting the black Kent paper were placed them on the building's roof. The temperature differences between the inlet and outlet air in each chamber were calculated from subtracting the inlet air temperature from the outlet air temperature.
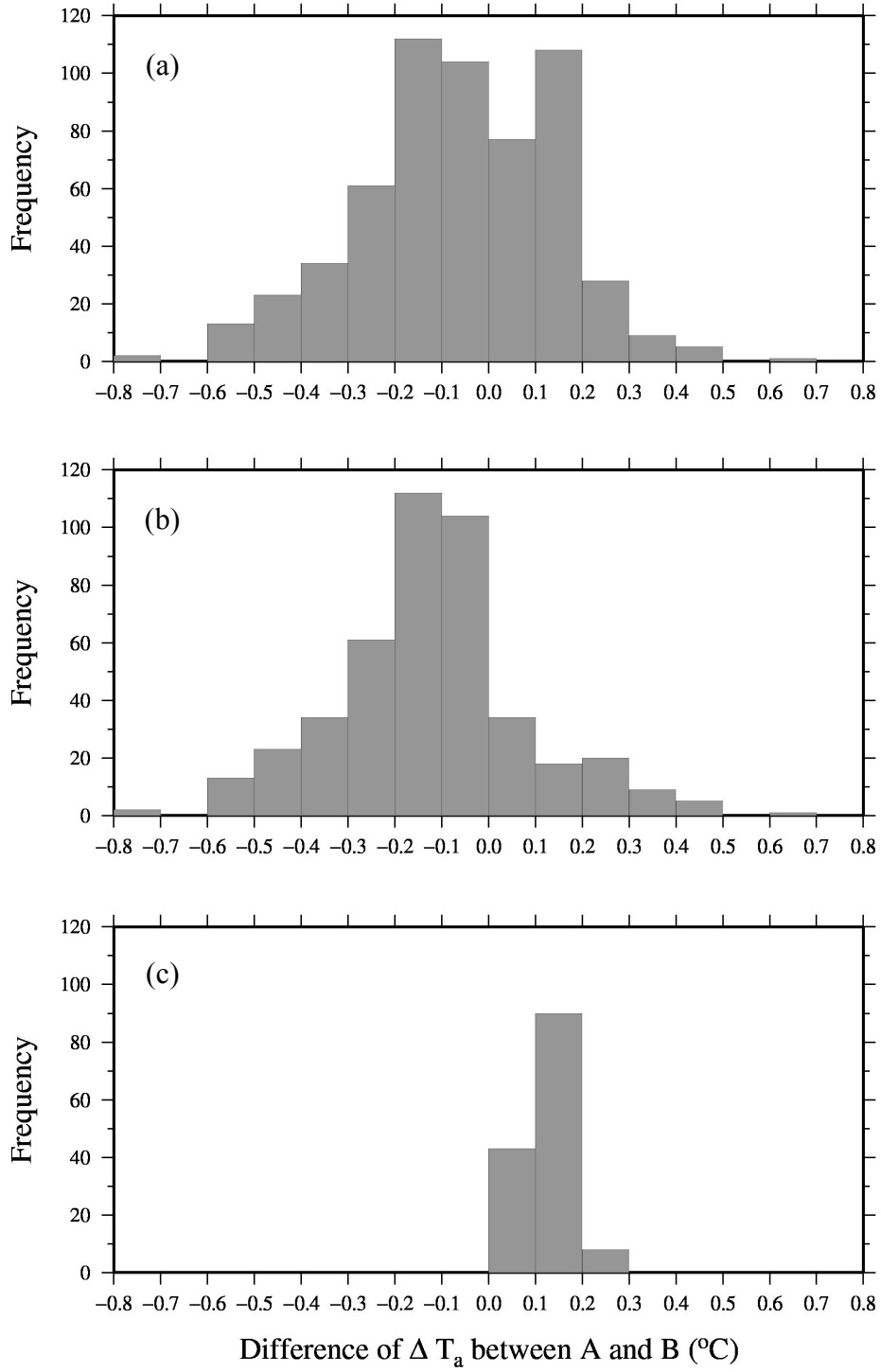
Fig. 4.4. Histogram of the difference between the temperature difference, ΔT_a, in the chamber A and the chamber B in all data (a), in the daytime (b), and in the nighttime (c). The difference of ΔT_a was calculated from subtracting ΔT_a in the chamber B from that in the chamber A.
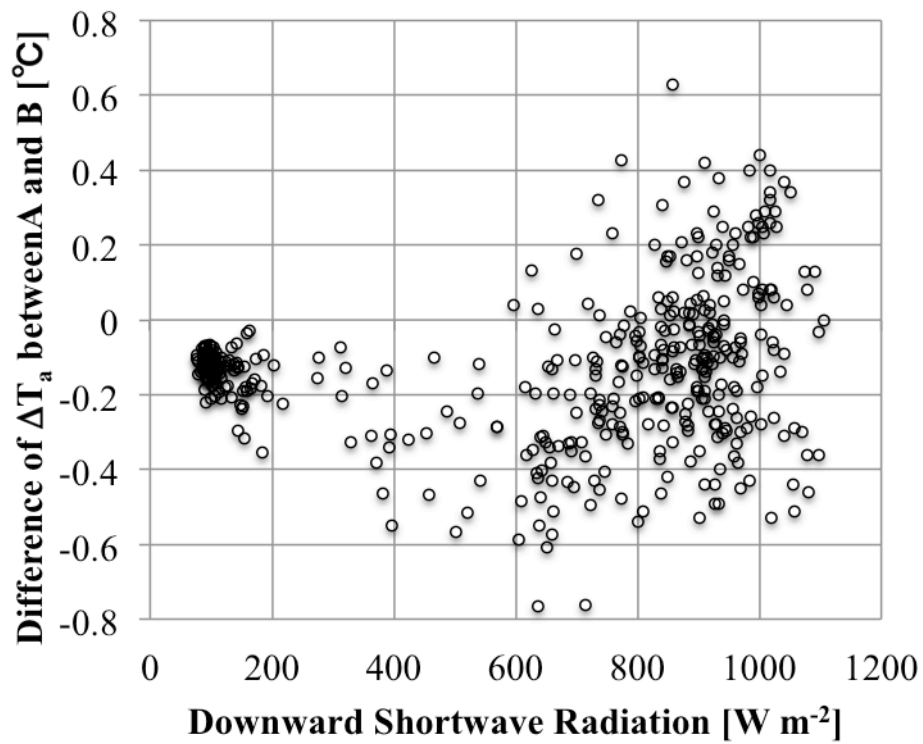
Fig. 4.5. Variation of the temperature difference between in the chamber A and chamber B on downward shortwave radiation. The difference of ΔT_a was calculated from subtracting ΔT_a in the chamber B from that in the chamber A.
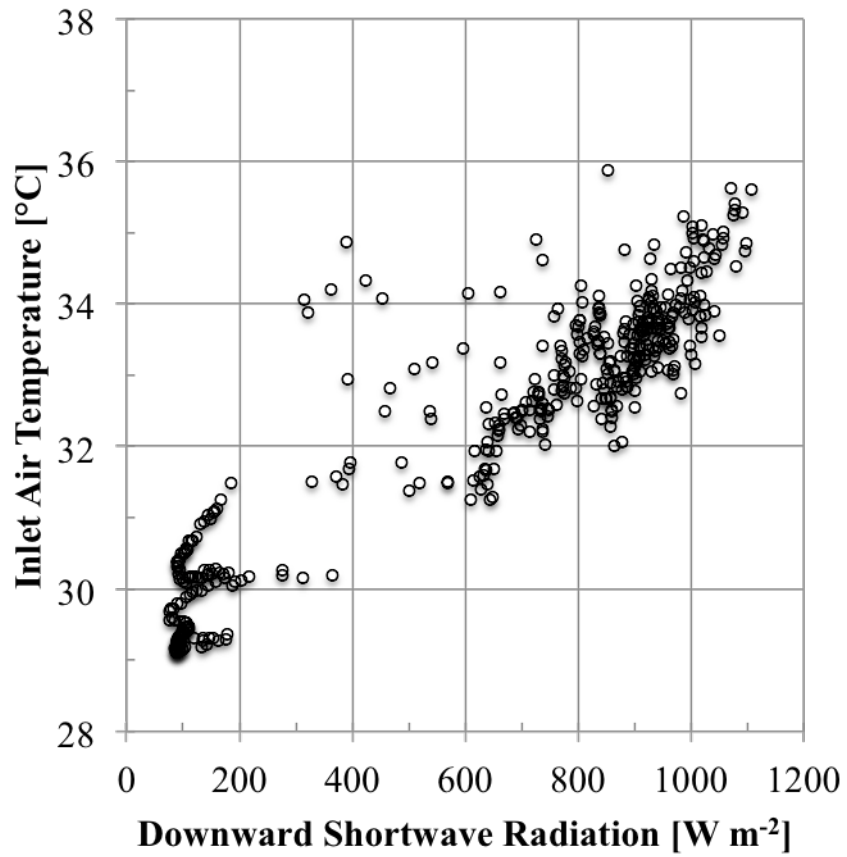
Fig. 4.6. Variation of inlet air temperature on downward shortwave radiation in the chamber A. The data in the chamber B were not shown because variation between inlet air temperature and downward shortwave radiation in the chamber B was approximately the same as that in the chamber A.
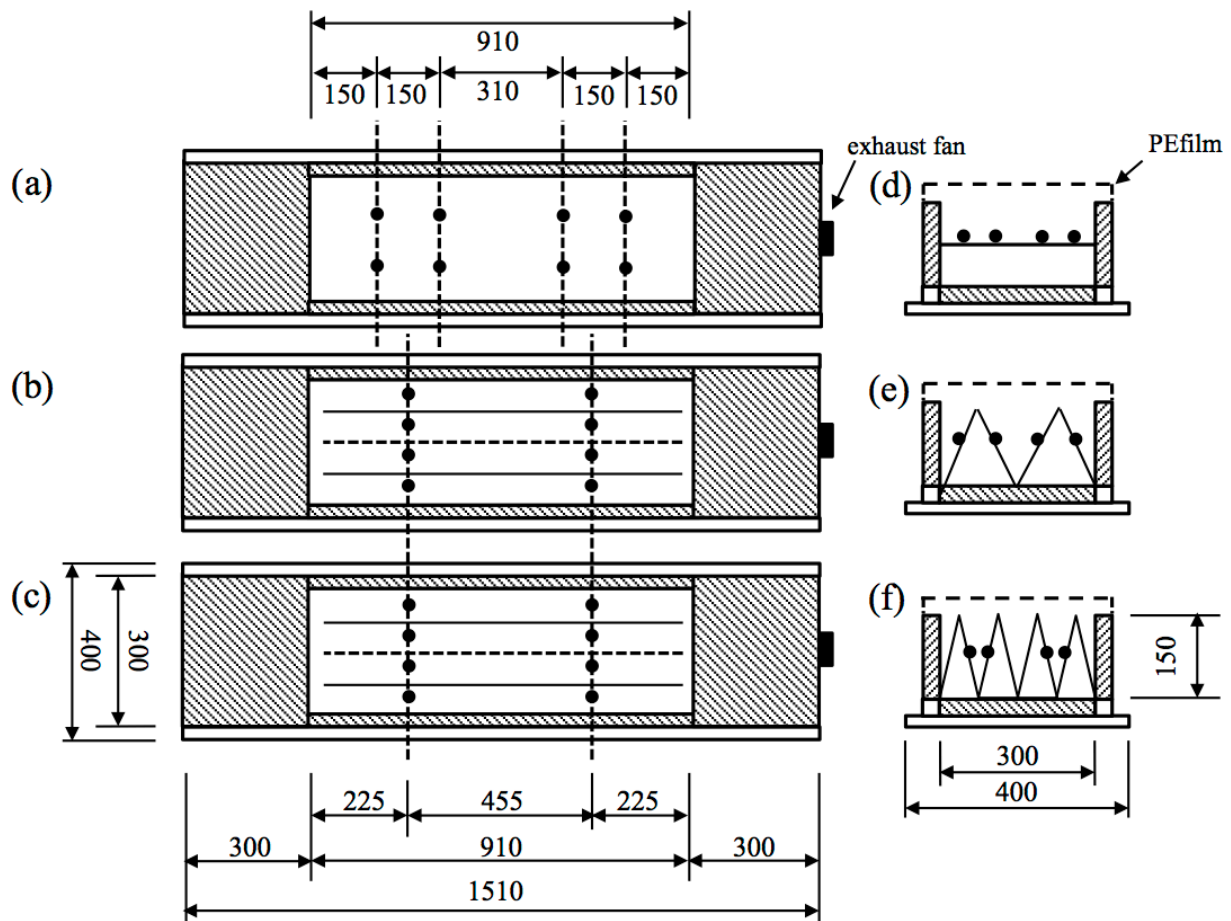
Fig. 4.7. Plane view of the measurement points for paper surface temperature of LAI = 1 (a), LAI = 2 (b), and LAI = 4 (c). Cross-section view of the measurement points for paper surface temperature of LAI = 1 (d), LAI = 2 (e), and LAI = 4 (f). Values written in the figures indicate length (mm). Shadowed areas indicate an extruded polystyrene foam panel. Circle symbols indicate each measurement point. The solid line and the dashed line in the PE section written in (a), (b), and (c) indicate the mountain fold and the valley fold, respectively.

Fig. 4.8. View of inside the PE-chamber with the Kent paper of LAI = 1 (a), LAI = 2 (b), and

LAI = 4 (c).
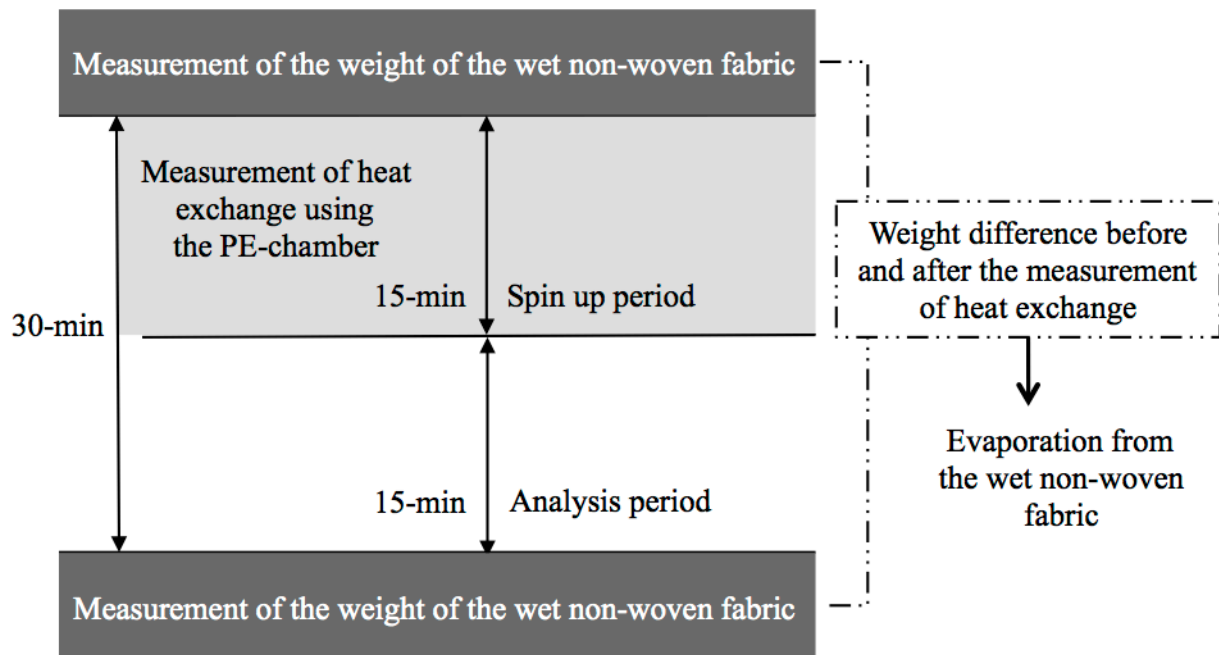
Fig. 4.9. Schematic of the experimental schedule for evaluating the cooling effect on the evaporation surface. The experiment went back and forth between the measurement of the weight and the measurement of heat exchange until the weight of the wet non-woven fabric became same as that of the dry one. Evaporation from the wet non-woven fabric was calculated from the weight difference before and after the measurement of heat exchange.
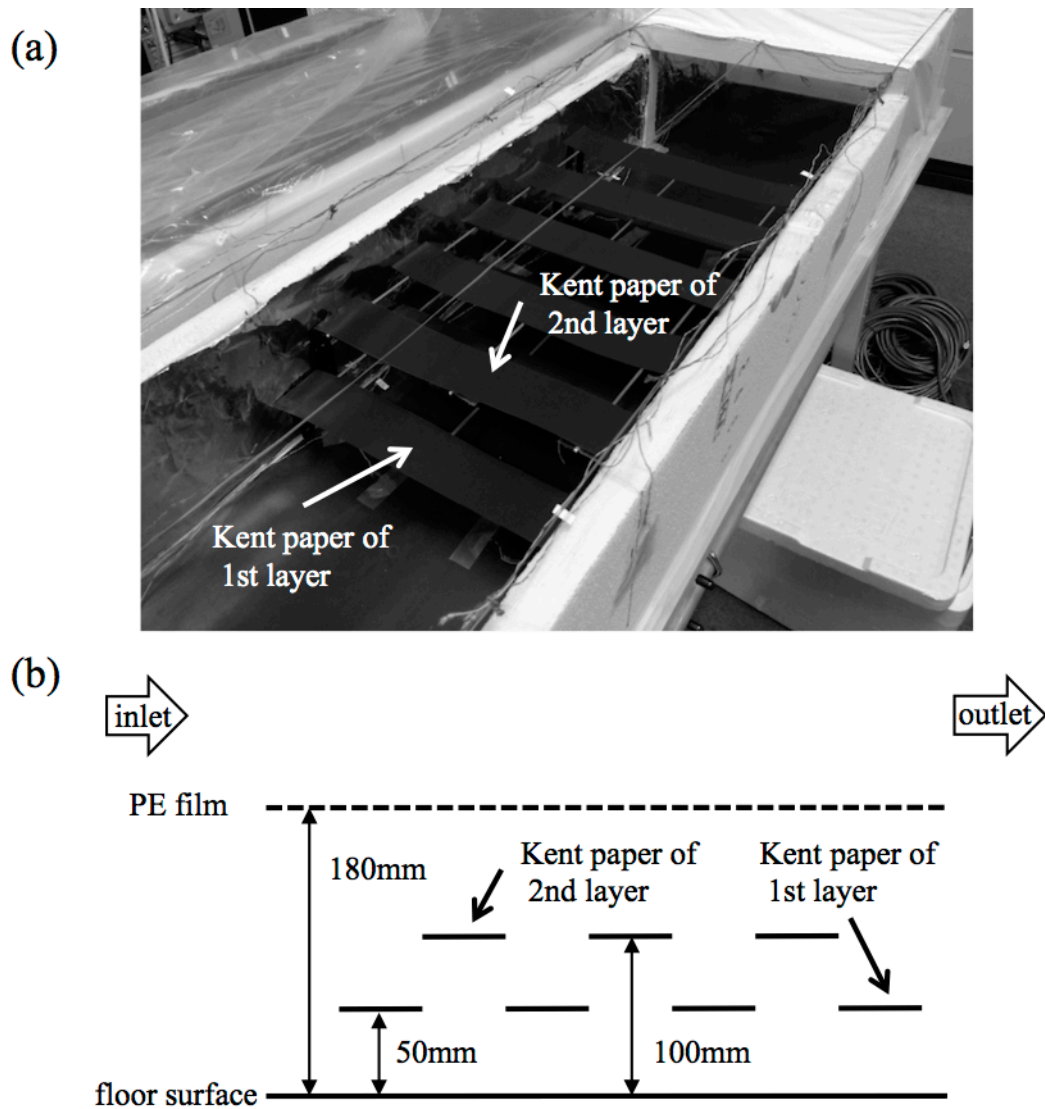
Fig. 4.10. (a) View of the scattered Kent paper inserted into the PE section. (b) Cross-section schematic of a part of the scattered Kent paper in the PE section. Kent papers of first and second layer were alternatively placed in the PE section. The heights of 1st and 2nd layer were 50mm and 100mm, respectively.
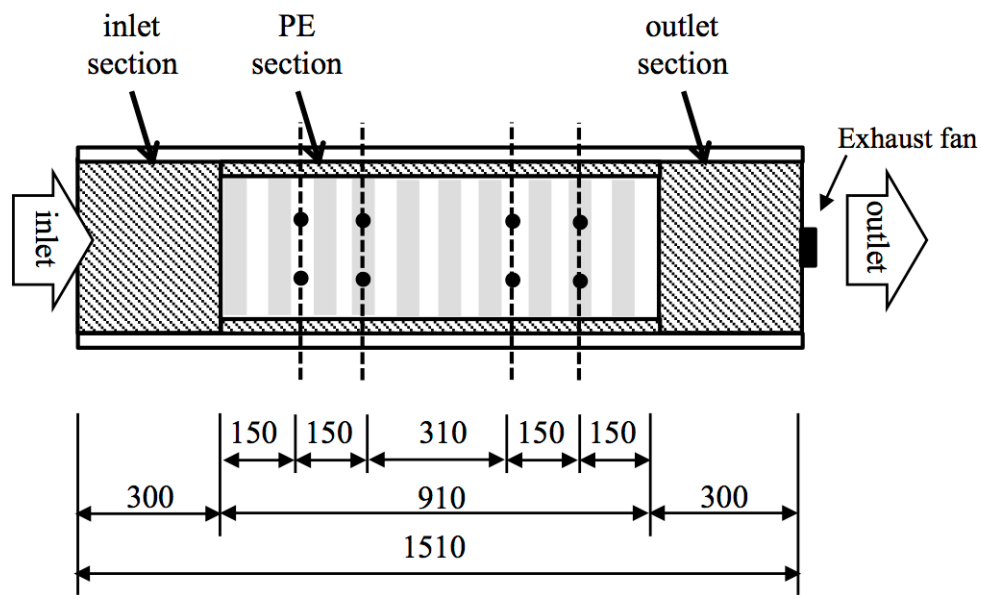
Fig. 4.11. Plane view of the measurement points for paper surface temperature of the scattered Kent paper. Values written in the figure indicate length (mm). Shadowed areas indicate an extruded polystyrene foam panel. Circle symbols indicate the measurement points. The gray area in the PE section indicates the Kent paper of first layer that was floated at a height of 50 mm. The white are in the PE section indicates the Kent paper of second layer that was floated at a height of 100 mm.
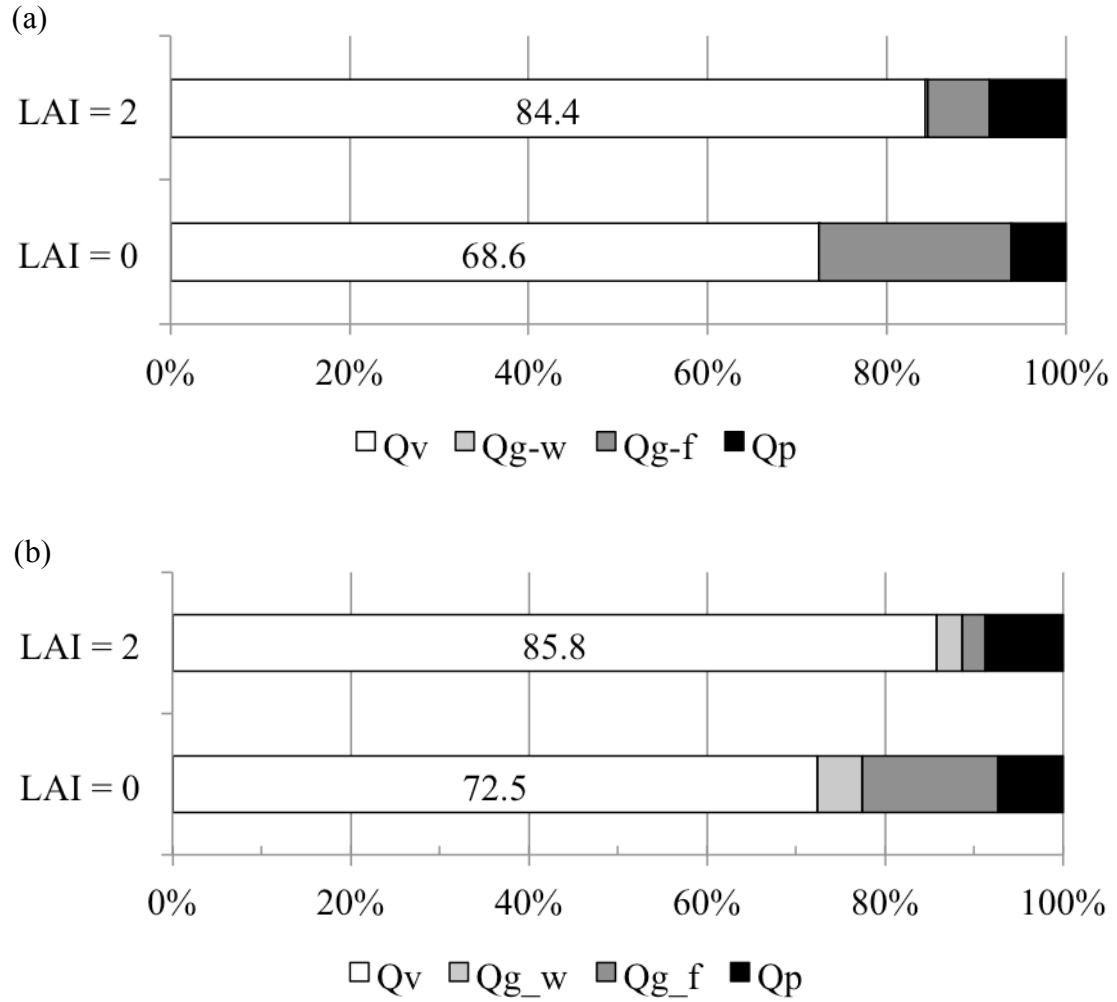
Fig. 4.12. 100% stacked bar chart of the heat balance component in the nighttime (a) and daytime (b). Q_v is heat flux due to ventilation, $Q_{g\text{-}w}$ is conductive heat flux through the sidewalls, $Q_{g\text{-}f}$ is conductive heat flux through the floor, and Q_p is heat transmission through the PE film. The values written in Q_v mean the ratio of Q_v for the whole heat balance.
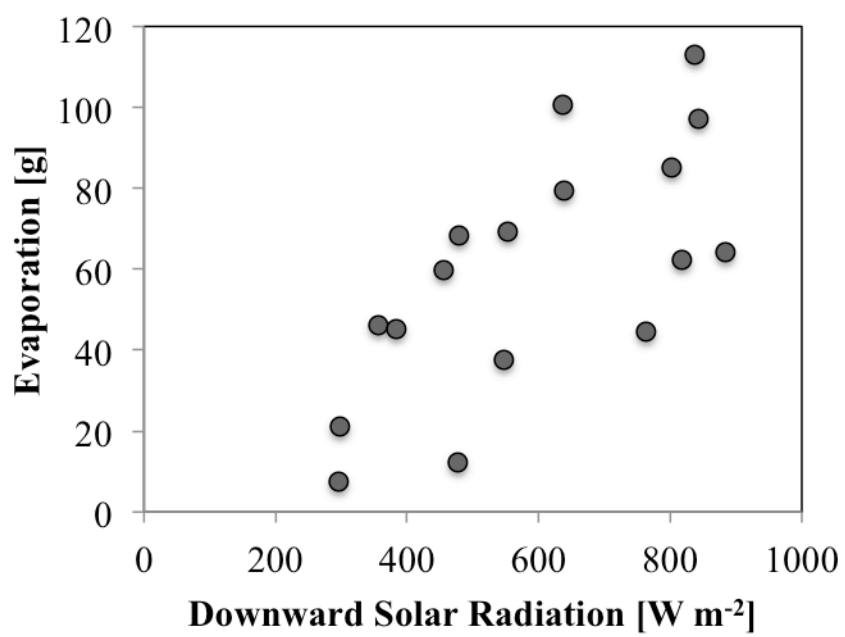
Fig. 4.13. Dependence of the evaporation on downward solar radiation. Evaporation from the wet non-woven fabric was calculated from the weight difference before and after the measurement of heat exchange.
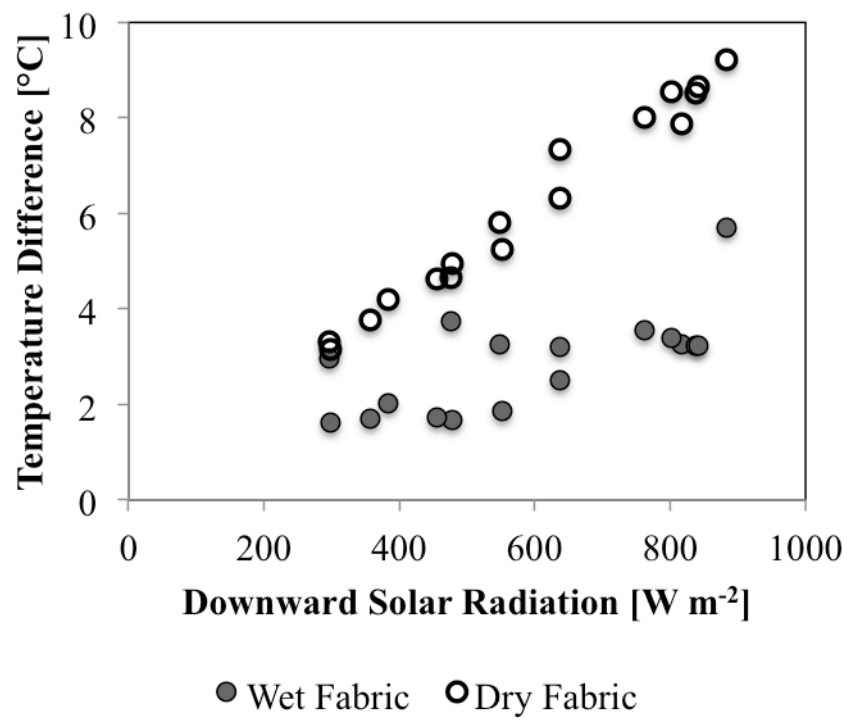
Fig. 4.14. Dependence of temperature difference between the inlet and outlet air on downward solar radiation. The white and gray circles indicate the results in the chamber with dry and wet non-woven fabric, respectively.
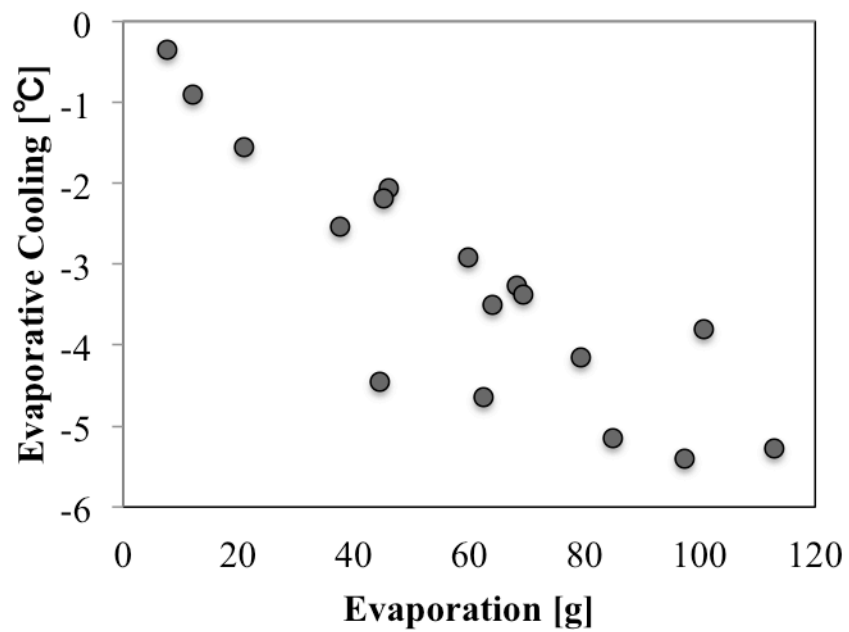
Fig. 4.15. Relationship between the evaporation and the evaporative cooling. Evaporation from the wet non-woven fabric was calculated from the weight difference before and after the measurement of heat exchange. The evaporative cooling was calculated from the increment of the temperature difference of the camber with the wet and dry non-woven fabric.
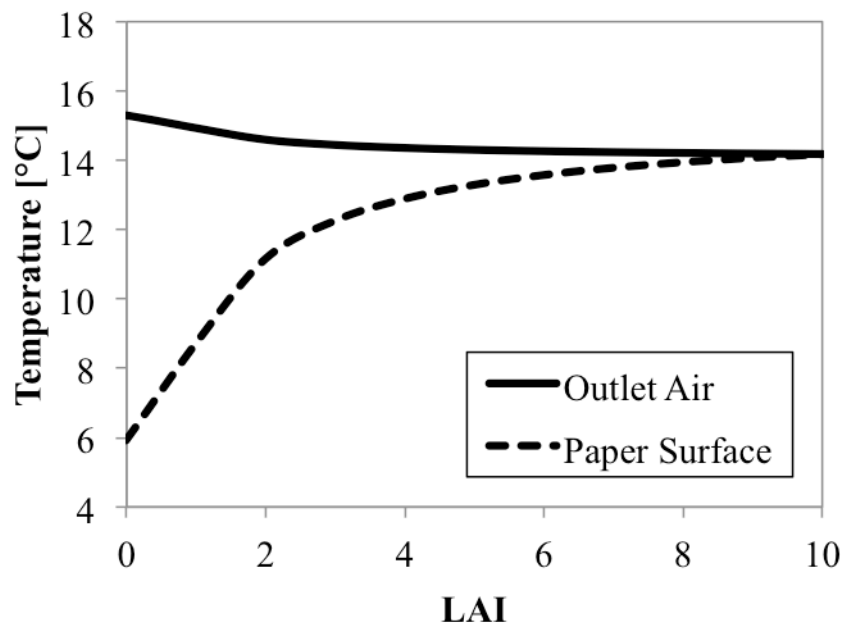
Fig. 4.16. Dependence of the outlet air temperature and the leaf model surface temperature on LAI in the simple heat balance equation. The outlet air temperature was calculated from **Eq. 4.14**, while the Kent paper surface temperature was calculated from **Eq. 4.18**.
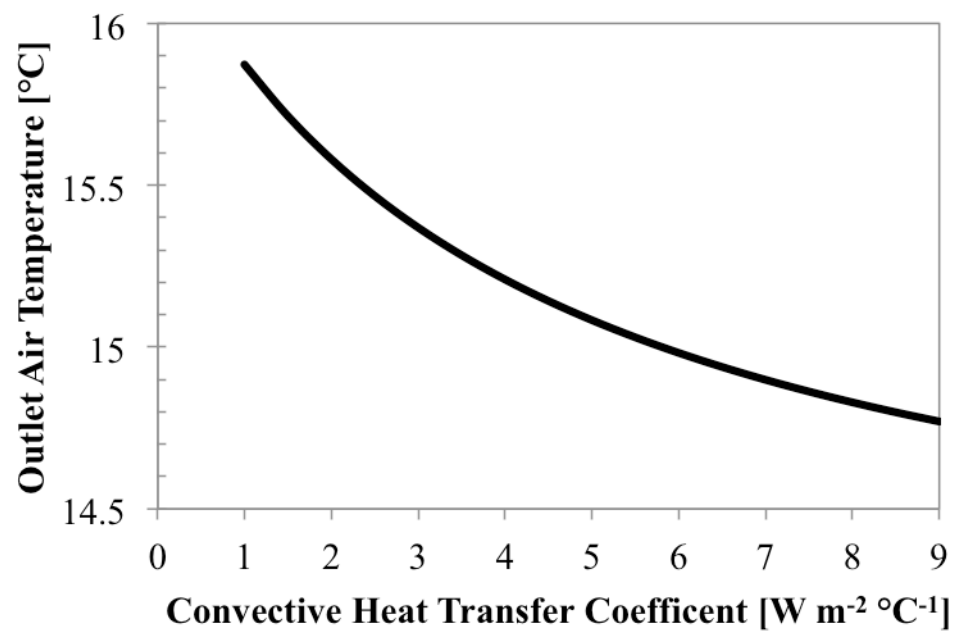
Fig. 4.17. Dependence of the outlet air temperature on the convective heat transfer coefficient in the simple heat balance equation. The outlet air temperature was calculated from **Eq. 4.14**.

	Chamber with a Kent paper	Chamber without a Kent paper
Surface temperature*	Higher	Lower
Radiation loss	Larger	Smaller
Outlet air temperature	Lower	Higher
Convective heat exchange	Larger	Smaller

Increase of radiation loss converts to heat exchange by convection

Radiation = Convection $\quad g_R\left(T_{sky}-T_k\right)=g_H\left(T_{in}-T_k\right)$ **Eq. 4.8**

Convection = Ventilation $\quad g_H\left(T_{in}-T_k\right)=g_V\left(T_{inlet}-T_{outlet}\right)$ **Eq. 4.5**

Heat in the air was absorbed by the surface in the chamber via convective heat exchange

Air traveling in the chamber with the paper is cooled more effectively than that in the chamber without the paper

*Paper surface temperature in case of the camber with a Kent paper
Floor surface temperature in case of the camber without a Kent paper

Fig. 4.18. Difference of heat exchange process in the chamber between with and without a Kent paper. The paper surface temperature in the chamber with the paper was higher than the floor surface one in the chamber without the paper. Increase of radiation loss increased convective heat exchange between the air and the surface in the chamber. Then, the heat in the air was absorbed by the surface in the chamber via the convective heat exchange. As a result, the outlet air temperature in the chamber with the paper was lower than that in the chamber without the paper.

5. Conclusions

This study performed two developments: 1) The development of a new formula to estimate globe temperature derived from the heat balance at the black globe surface. 2) The development of a new experimental equipment, the polyethylene chamber, to research heat exchange between vegetation surface and its surrounding air.

To develop a new estimation formula for globe temperature, in Chapter 2, we revealed the heat balance at a globe surface and derived a new estimation formula for globe temperature from its heat balance equation. The results are summarized as follows:

1) Globe temperature depended curvilinearly on global solar radiation. Previous empirical formulae for globe temperature expressed this dependency either by hyperbolic function of global solar radiation, or dividing formula into two linear formulae. However, there were inherent defects in these formulae, such as lack of wind speed dependency, and a discontinuity in the predicted nonlinear response to global solar radiation.

2) The new formula developed in this study was able to estimate the curvilinear dependence of globe temperature on global solar radiation, and it also showed the globe temperature response to wind speed.

The new estimation formula was applied to an extension area using long-term observation data of four major cities by Okada et al. (2013c). The use of their formula required only air temperature, global solar radiation, and wind speed. Thus, their formula is expected to monitor and predict WBGT in the numerical meteorological simulation.

To accumulate the basic knowledge about nocturnal heat exchange between vegetation surface and surrounding air, we developed a new apparatus, polyethylene (PE) chamber. The design and related heat balance about the PE chamber were introduced in Chapter 3. In Chapter 4, we examined heat exchange depending on heat exchange surface morphology particularly focusing on the nighttime. Then, we inserted black Kent papers into the PE chamber instead of a real leaf. Additionally, the simple heat balance equation about the PE chamber was introduced to discuss the measurement results. The results are summarized as follows:

1) The PE chamber has two ends serving as an air inlet and an air outlet, and it was ventilated in the longitudinal direction using an exhaust fan. Therefore, there is an air temperature difference between the inlet and the outlet of the chamber. Using the air temperature difference between the inlet and the outlet and other heat balance components, we could evaluate the heat exchange process.

2) A PE film cover section was the measurement section of the PE chamber and was covered with thin PE film. Thin PE film has a transmittance as high as 85% or larger for not only shortwave radiation but also longwave radiation. Therefore, the radiative environment in the PE chamber was similar to outdoor that. Hence, the PE chamber was applicable to evaluate heat exchange under nocturnal radiative cooling.

3) In the nighttime, radiation loss from surface in the chamber to the sky converted to convective heat exchange between the air and all surface in the chamber. Thus, the heat in the air was absorbed by the surface in the chamber via the convective heat exchange. Installation of the Kent paper in the chamber increased heat exchange between the air and the all surface in the chamber. The paper surface temperature in the chamber with the paper was higher than the floor surface one in the chamber without the paper. Also, the outlet air temperature in the

173

chamber with the paper was lower than that in the chamber without the paper. In other words, the air traveling in the chamber with the paper was cooled more effectively than that in the chamber without the paper. These results indicate that the colder surface did not necessarily produce the larger cooling the surrounding air.

4) Increasing the area of the heat exchange surface resulted in an increase of convective heat transfer. Then, this increase of convective heat transfer resulted in the acceleration of cooling air in the nighttime or heating air in the daytime. However, this relationship did not change linearly, and outlet air temperature and surface temperature approached a balance point.

5) The scattered heat exchange surface resulted in an increase of convective heat transfer. As with the experiment for the area of the heat exchange surface, this increase of convective heat transfer resulted in the acceleration of cooling air in the nighttime or heating air in the daytime. However, this relationship did not change linearly, and outlet air temperature and surface temperature approached a balance point.

These results indicated that the PE chamber is useful to understand the quantitative aspects of nocturnal heat exchange between vegetation surface and surrounding air. The basic knowledge obtained from the PE chamber would contribute to propose the effective greening for cooling the urban atmosphere. Finding 3) implies that the cooler urban park does not cool the urban atmosphere more effective. Findings 4) and 5) imply that the scattered urban park with dense vegetation is able to cool the urban atmosphere well. Note that these suggestions are given from the viewpoint of the meteorology only. For example, an open grass park is necessary for providing an evacuation area in the time of disaster. It is important to determine the optimal vegetation size and its allocation considering the purpose of each park in each urban area.

According to the above results, two developments are expected to progress the more reliable influence assessment on human health and to accumulate the basic knowledge for cooling the urban atmosphere. In Japan, for example, Kumagaya city in Saitama prefecture and Tajimi city in Gifu prefecture has been known as the extreme hot city. Numerous studies investigated the thermal environment and formation mechanisms of extreme high air temperature in these cities (e.g., Sakurai et al. 2009; Shinohara et al. 2009; Watarai et al. 2009a,b; Takane and Kusaka 2011, Takane et al. 2013; Okada et al. 2014). For the mitigation of the thermal environment in such cities, it is expected to use proactively the new estimation formula and the PE chamber.

6. Future issues

In this study, we developed a new estimation formula for globe temperature under all weather conditions and a new apparatus, polyethylene (PE) chamber, to investigate heat exchange between vegetation surface and surrounding air. The followings are the future issues about each development.

Development of a new estimation formula for globe temperature:

• We assumed that a black globe was placed on the open field. Then, a new estimation formula expressed net shortwave radiation in global solar radiation only. However, the shortwave radiation balance in the urban canyon is much complicated (Kondo and Liu 1998; Kusaka et al. 2001). The improvement of the expression of shortwave radiation is the subject to use the new formula in the urban canyon.

• We assumed that the black globe surface was dry in the derivation process. Latent heat is exchanged between the black globe surface and the air when wetted by precipitation. It would be necessary to consider the globe temperature after the precipitation in the region with a high rainfall like Japan. Thus, an estimation formula derived from heat balance at the "wet" black globe surface is suitable to estimate globe temperature after the precipitation.

Development of the PE chamber:

• In this study, we used the black Kent paper instead of a real leaf and the PE chamber was elevated on the ground surface. Hence, the influence of the conductive heat transfer was much small in the PE chamber. The ground heat flux and the photosynthetic energy storage of the

176

vegetation canopy are dominant in the nocturnal energy balance in the forest (e.g., McCaughey and Saxton 1988: Baldocchi et al. 2000: Silberstein et al. 2003). The influence of the conductive heat transfer is the subject of further study using the PE chamber.

• Smallness of the PE chamber is the advantage of investigating heat exchange between the vegetation surface and its surrounding air without considering the similarity law. The results obtained from the PE chamber are quantitative, and cannot be scaled up for the actual phenomena of an urban park. The remaining issue is the enlargement of the PE chamber for further study.

Acknowledgements

178

References

Arya, P. S., 2001: Introduction to micrometeorology (*2nd ed.*). Academic Press, California, 420 pp.

Baldocchi, D. D., B. E. Law and P. M. Anthoni, 2000: On measuring and modeling energy fluxes above the floor of a homogeneous and heterogeneous conifer forest. *Agric. For. Meteorol.*, **102**(2), 187-206.

Barradas, V. L., 1991: Air temperature and humidity and human comfort index of some city parks of Mexico City. *Int. J. Biometeorol.*, **35**(1), 24–28.

Brunt, D., 1939: Physical and Dynamical Meteorology. Cambridge University Press, London, 428 pp.

Budd, M., 2008: Wet-bulb globe temperature (WBGT) -its history and its limitations, *J. Sci. Med. Sport*, **11**, 20–32.

Bureau of Social Welfare and Public Health, Tokyo Metropolitan Government, 2013: The situation (23 wards of Tokyo) of the heat stroke dead of the summer of 2013

Ca, V. T., T. Asaeda and E. M. Abu, 1998: Reductions in air conditioning energy caused by a nearby park. *Energy. Build.*, **29**, 83–92.

Campbell, G. S. and J. M. Norman, 1998: An Introduction to Environmental Biophysics (*2nd ed.*). Springer, New York, 286 pp.

Chang, C. R., M. H. Li and S. D. Chang, 2007: A preliminary study on the local cool-island intensity of Taipei city parks. *Landscape Urban Plann.*, **80**(4), 386–395.

Defraeye, T., P. Verboven, Q. T. Ho and B. Nicolai, 2013: Convective heat and mass exchange predictions at leaf surfaces: Applications, methods and perspectives. *Comput. Electr. Agric.*,

96, 180–201.

Denmead, O. T., 1984: Plant physiological methods for studying evapotranspiration: problems of telling the forest from the trees. *Agric. Water Manage.*, **8**(1), 167–189.

Dimiceli, V. E., S. F. Piltz and S. A. Amburn, 2011: Estimation of black globe temperature for calculation of the wet bulb globe temperature index. Proceedings of the World Congress on Engineering and Computer Science, **2**, 591-599, San Francisco, USA.

Eliasson, I. and H. Upmains, 2000: Nocturnal airflow from urban parks-implications. *Theor. Appl. Climatol.*, **66**(1-2), 95–107.

Fanger, P. O., 1972: Thermal comfort. McGraw Hill, New York, 256pp.

Fiala, D., K. J. Lomas and M. Stohrer, 2001: Computer prediction of human thermoregulatory and temperature responses to a wide range of environmental conditions. *Int. J. Biometeorol.*, **45**(3), 143–159.

Fire and Disaster Management Agency, 2013: The situation of the emergency conveyance due to the heat stroke on July, 2013. (available at http://www.fdma.go.jp/neuter/topics/houdou/h25 /2508/250809_1houdou/01_houdoushiryou.pdf)

Funk, J. P., 1959: Improved polythene-shielded net radiometer. *J. Sci. Instrum.*, **36**, 268–270.

Gagge, A. P., J. A. Stolwijk and Y. Nishi, 1971: An Effective Temperature Scale based on a Simple Model of Human Physiological Regulatory Response, *ASHRAE Trans.*, **71**(1), 247–262.

Gaspar, A. R. and D. A. Quintela, 2009: Physical modeling of globe and natural wet bulb temperatures to predict WBGT heat stress index in outdoor environments. *Int. J. Biometeorol.*, **53**(3), 221–230.

Georgescu, M., M. Moustaoui, A. Mahalov and J. Dudhia, 2012: Summertime climate impacts

of projected megapolitan expansion in Arizona. *Nat. Clim. change*, doi: 10.1038/nclimate1656

Hagishima. A., K. Narita and J. Tanimoto, 2007: Field experiment on transpiration from isolated urban plants. *Hydrol. Process.*, **21**, 1217–1222.

Hamada, T. and T. Mikami, 1994: Cool island phenomena in urban green spaces: A case study of Meiji shrine and Yoyogi park. *Geogr. Rev. Jpn.*, 67A(8), 518–529. (in Japanese with English abstract).

Hino, M. and M. Kanda, 1989: Study on the climate moderation effect of plant by lysimeter with wind-tunnel. *J. Jpn. Soc. Hydrol. Water Resour.*, **2**(1), 61–69. (in Japanese with English abstract).

Honjo, T. and T. Takakura, 2000a: Validation of the two dimensional k-ε model for analysis of the thermal effect of urban green areas. *J. Agric. Meteorol.*, **56**(4), 243–251. (in Japanese with English abstract).

Honjo, T. and T. Takakura, 2000b: Simulation of the influence of urban green areas with various scales and allocation. *J. Agric. Meteorol.*, **56**(4), 253–260. (in Japanese with English abstract).

Horie, K. and H. Fujiwara, 2010: Measurement of globe temperature at Sapporo District Meteorological Observatory and trait of the empirical equations to estimate WBGT. *Saihyo*, 56, 19–21. (in Japanese).

Horie, T., H. Nakagawa, J. Nakano, K. Hamotani and H. Y. Kim, 1995: Temperature gradient chambers for research on global environment change. III. A system designed for rice in Kyoto, Japan. *Plant. Cell. Environ.*, **18**(9), 1064–1069.

Huang, H. Y., S. A. Margulis, C. R. Chuand and H. C. Tsai, 2011: Investigation of the impacts

of vegetation distribution and evaporative cooling on synthetic urban daytime climate using a coupled LES-LSM model. *Hydrol. Process*, **25**(10), 1574–1586.

Hunter, C. H. and C. O. Minyard, 1999: Estimatin wet bulb globe temperature using standard meteorological measurements, 2nd Conference on Environmental Applications, Report No. WSRC-MS-99-00757, Long Beach, USA.

Inoue, K., K. Nakazono and T. Kawakata, 2004: Numerical experiments for vegetation mitigation effects on thermal environment. *Bull. Natl. Agric. Res. Cent.*, **5**, 1–21. (in Japanese with English abstract).

IPCC, 2013: Working Group I Contribution to the IPCC Fifth Assessment Report Climate Change 2013: The Physical Science Basis Summary for Policymakers. (available at http://www.climatechange2013.org/images/uploads/WGIAR5-SPM_Approved27Sep2013.pdf

ISO 7243, 1989: Hot environments-Estimations of the heat stress on working man, based on the WBGT Index (Wet Bulb Globe Temperature). International Standard (1st ed.) International Organization for Standardization (ISO), Geneva.

Japanese Ministry of the Environment, 2010: Report of provision of heat stroke prevention information by WBGT observation. http://www.env.go.jp/air/report/h22-04/index.html

Jauregui, E., 1991: Influence of a large urban park on temperature and convective precipitation in a tropical city. *Energy. Build.*, **15-16**, 457–463.

JIS Z 8504, 1989: Hot environments-Estimation of the heat stress on working man, based on the WBGT-index (wet bulb globe temperature). Industrial Standard, Japan Standards Association. (in Japanese).

Kanda, M. and M. Hino, 1990a: Numerical simulation of soil-plant-air system (1) modeling of

plant system. *J. Jpn. Soc. Hydrol. Water Resour.*, **3**(3), 37–46. (in Japanese with English abstract).

Kanda, M. and M. Hino, 1990b: Numerical simulation of soil-plant-air system (2) numerical experiment on the effect of plant on meteorological and environment. *J. Jpn. Soc. Hydrol. Water Resour.*, **3**(3), 47–55. (in Japanese with English abstract).

Kanda, M., R. Moriwaki, Y. Takayanagi, H. Yokoyama and T. Hamada, 1997: Environmental effect of Meiji shrine forest as a sink for atmospheric energy and pollutants (1) Field observation in summer 1996. *Tenki*, **44**(10), 31–40. (in Japanese).

Kim, H. Y., T. Horie, H. Nakagawa and K. Wada, 1996: Effects of elevated CO_2 concentration and high temperature on growth and yield of rice 2. The effect on yield and its components of Ahihikari rice. *Jpn. J. Crop. Sci.*, **65**(4), 644–651.

Kimura, K., 1970: Fundamental theories of building services. Gakkensya, Tokyo, 416pp.

Kobayashi, K., 1981: A subroutine for function minimization by the simplex method. *Rep. Agric. For. Fish. Res.*, A17, 51-70. (in Japanese).

Kondo, J., 1994: Hydrometeorology, water and heat budgets on ground surfaces. Asakura Publishing Co. LTD, Tokyo, 350 pp. (in Japanese).

Kondo, J., 2000: Atmospheric science near the ground surface. University of Tokyo Press, Tokyo, 324 pp. (in Japanese).

Kondo, H. and F. H. Liu, 1998: A Study on the Urban Thermal Environment Obtained through One-Dimensional Urban Canopy Model. *J. Japan. Soc. Atmos. Environ.*, **33**, 179–192. (in Japanese).

Kondo, J. and T. Watanabe, 1992: Studies on the bulk transfer coefficients over a vegetated surface with a multilayer energy budget model. *J. Atmos. Sci.*, **49**(23), 2183–2199.

Kusaka. H, M. Hara and Y. Takane, 2012: Urban climate projection by the WRF model at 3-km horizontal grid increment: dynamical downscaling and predicting heat stress in the 2070's August for Tokyo, Osaka, and Nagoya Metropolises. *J. Meteorol. Soc. Jpn.*, **90B**, 47–63.

Lee, J. S., T. Usami, and T. Oikawa, 2001: High performance of CO2–temperature gradient chamber newly built for studying the global warming effect on a plant population. *Ecol. Res.*, **16**(2), 347–358.

Leuning, R. and I. J. Foster, 1990: Estimation of transpiration by single trees: comparison of a ventilated chamber, leaf energy budgets and a combination equation. *Agric. For. Meteorol.*, **51**(1), 63–86.

Maruta. Y., 1972: The various studies on urban climatology have demonstrated the following findings. *City. Plan.*, **69-70**, 49–77. (in Japanese)

McAdams, W.H., 1954; Heat transmission (3rd ed.). McGraw Hill, New York, 249 pp.

McCaughey, J. H. and W. L. Saxton, 1988: Energy balance storage terms in a mixed forest. *Agric. For. Meteorol.*, **44**(1), 1-18.

Mochida, T., K. Kuwabara and T. Sakoi, 2007: Theoretical expressions of WBGT and examinations of the original WBGT from standpoint of thermo-physiological engineering: characteristics of WBGT for outdoor conditions. *T. Soc. Heat. Air-Condition. Sanit. Engineers. Jpn.*, **128**, 1–9 (in Japanese with English abstract).

Mochida, T. and T. Sakoi, 2010: WBGT derived from heat balance equation on human body and its characteristics : thermal physiological meaning of WBGT proposed by Yaglou et al. *Jpn. J. Biometeorol.*, **47**(4), 139–148. (in Japanese).

Mochida , T. and T. Sakoi, 2011: Science of WBGT. *Jpn. J. Biometeorol.*, **48**(4), 103–110. (in Japanese).

Munn, R. E., 1966: Descritive micrometeorology. Academic Press, New York and London, 245 pp.

Murakami, M. and F. Kimura, 2010: Manual of handmade field-portable forced ventilation thermometer. *Terr. Environ. Res. Cent. Rep., Univ. Tsukuba*, **11**, 29-33. (in Japanese).

Nakai, S., A. Yorimoto and T. Morimoto, 1992: The Relation between environmental conditions and the occurrence of exertional heat disorders during physical activity. *Jpn. Soc. Phys. Fit. Sport Med.*, **41**(5), 540–547. (in Japanese with English abstract).

Narita, K., T. Mikami, H. Sugawara, T. Honjo, K. Kimura and N. Kuwata, 2004: Cool-island and cold air-seeping phenomena in an urban park, Shinjuku-Gyoen, Tokyo. *Geogr. Rev. Jpn.*, **77**(6), 403–420. (in Japanese with English abstract)

Nelder, J. A. and R. Mead, 1965: A simplex method for function minimization. *Comput. J.*, 7(4), 308–313.

Ohashi, Y., Y. Kikegawa, K. Yamaguchi, T. Ihara and K. Oka, 2010: Evaluations of hot environment at outdoor activity spaces with a numerical meteorological model. *Jpn. J. Biometeorol.*, **47**(2), 91–106. (in Japanese)

Ohashi, Y., H. Ryumon and Y. Shigeta, 2009: Comparison among WBGT values observed at various living and sports spaces in an urban area. *Jpn. J. Biometeor.*, **46**(2), 59–68. (in Japanese with English abstract).

Okada, M. and H. Kusaka, 2013: Proposal of a new equation to estimate globe temperature in an urban park environment. *J. Agric. Meteorol.*, **69**(1), 23–32.

Okada, M., H. Kusaka, M. Takaki, S. Abe, Y. Takane, Y. Fuji and T. Nagai, 2014: Distribution of air temperature in Tajimi city in summer. *Tenki*, **61**(1), in press.

Okada, M., Y. Wakazuki, S. Inukai, R. Hirota and H. Kusaka, 2013a: An investigation of air

temperature distribution in-and outside of a wooded area in early winter morning -A case study for the Yoyogi-park and the Meiji-shrine-. *Heat Island Inst. Inter.*, **8**, 7–12.

Okada, M., M. Okada and H. Kusaka, 2013b: Proposal of a polyethylene chamber for a physical model experiment of heat exchange on vegetation surfaces. *Boundary-Layer Meteorol.*, in revision.

Okada, M., M. Okada and H. Kusaka, 2013c: Parameter adjustment and application to an extension area of Okada and Kusaka's formula for the black globe temperature. *J. Heat Island Inst. Inter.*, in press.

Okada, M., 1983: The measurement of infrared properties of plastic films by means of a commercial emissivity measuring instrument. *J. Agric. Meteorol.*, **39**(1), 31–34. (in Japanese)

Okada, M. and M. Hayashi, 1983: Proposing an equation to evaluate greenhouse heat transmission. *J. Agric. Meteorol.*, **39**(2), 91–95. (in Japanese with English summary).

Okada, M., T. Hamasaki and T. Hayashi, 1995: Temperature gradient chambers for research on global environment change. 1. thermal environment in a large chamber. *Biotronics*, **24**, 85–97.

Oke, T. R., 1987: Energy and mass exchange. In *Boundary Layer Climates* (2*nd ed*.). Routledge, London, 332pp.

Oke, T. R., 1989: The micrometeorology of the urban forest. *Philos. Trans. R. Soc. London, Ser. B*, **324**, 335–349.

Ono, M., A. Shimizu and K. Tsuda, 2006: The evaluation of WBGT based on continuous observation. *Jpn. J. Biometeorol.*, **43**(3), S27. (in Japanese).

Rawson, H. M., R. M. Gifford and B. N. Condon, 1995: Temperature gradient chambers for

research on global environment change. I. Portable chambers for research on short−stature vegetation. *Plant. Cell. Environ.*, **18**(9), 1048–1054.

Rijal, H. B., R. Ooka, H. Huang, T. Katsuki and B. Oh, 2010: Heat island mitigation effect of large-scale greenery using numerical simulation. *Seisankenkyu*, **62**(10), 54–61. (in Japanese with English abstract).

Sakai, S., M. Nakamura, K. Furuya, N. Amemura, M. Onishi, I. Iizawa, J. Nakata, K. Yamaji, R. Asano and K. Tamotsu, 2012: Sierpinski's forest: New technology of cool roof with fractal shapes. *Energy. Build.*, **55**, 28–34.

Sakurai, M., Y. Shinohara, K. Mashita and T. Sunaga, 2009: The high temperature event of over 40.8 °C in the Central Kanto area, summer 2007. Part 1: Case studies for 15 and 16 August 2007. *Tenki*, **56**, 248–253. (in Japanese)

Shinohara, Y., K. Mashita, M. Sakurai and T. Sunaga, 2009: The high temperature event of over 40.8 °C in the Central Kanto area, summer 2007. Part 2: Numerical simulation using the JMA- NHM and considerations of formation factors. *Tenki*, **56**, 543–548. (in Japanese)

Silberstein, R. P., M. Sivapalan, N. R. Viney, A. Held and T. J. Hatton, 2003: Modelling the energy balance of a natural jarrah (Eucalyptus marginata) forest. *Agric. For. Meteorol.*, **115**(3-4), 201-230.

Sinclair, R., 1970: Convective heat transfer from narrow leaves. *Aust. J. Biol. Sci.*, **23**(2), 309–322.

Spronken-Smith, R. A. and T. R. Oke, 1998: The thermal regime of urban parks in two cities with different summer climates. *Int. J. Remote Sens.*, **19**(11), 2085–2104.

Spronken-Smith, R. A., T. R. Oke and W. P. Lowry, 2000: Advection and the surface energy balance across an irrigated urban park. *Int. J. Climatol.*, **20**(9), 1033–1047.

Sugawara, H., K. Narita, T. Mikami, T. Honjo and K. Ishii, 2006: Cool island intensity in a large urban green: seasonal variation and relationship to atmospheric condition. *Tenki*, **53**(5), 393–404.

Suzuki, H., I. Misaka, A. Mizutani and Y. Tashiro, 2005: Estimating the effects of wall greening on improving the thermal environment using the indices of WBGT and SET*. *J. Jpn. Inst. Landscape Arch.*, **69**(5), 441–446.

Takaichi, M., T. Hosono, H. Kurosaki, S. Watanabe, H. Kawashima and Y. Nakano, 2003: Estimation of WBGT and evaluation of time and space to work healthily in a greenhouse. (available at http://www.naro.affrc.go.jp/project/results/laboratory/ vegetea/2003/vegetea03-24.html) (in Japanese).

Takane, Y. and H. Kusaka, 2011: Formation mechanism of the extreme surface air temperature of 40.9 °C observed in the Tokyo metropolitan area: Considerations of dynamic foehn and foehn-like wind. *J. Appl. Meteor. Clim.*, **50**(9), 1827–1841.

Takane, Y., H. Kusaka, M. Takaki, M. Okada, S. Abe, T. Nagai, Y. Fuji and S. Iizuka, 2013: Observational Study and Numerical Prediction Experiments on Wet-Bulb Globe Temperature in Tajimi, Gifu Prefecture: Consideration of Uncertainty with a Physics Parameterization Scheme and Horizontal Resolution of the Weather Research and Forecasting Model. *Geophysical Review of Jpn.*, **86**(1), 14–37. (in Japanese with English abstract).

Thom, E. C., 1959: The Discomfort Index, *Weatherwise*, **12**(2), 57–61.

Tonouchi, M. and K. Murayama, 2008: Regional characteristic for the risk of heat attack and HWDI. *Jpn. J. Biometeorol.*, **45**(3), S62. (in Japanese).

Toriyama, A., N. Monji, Y. Aono and K. Hamotani, 2001: Effects of foliage and sky view factor

on the urban thermal environment. *J. Agric. Meteorol.*, **57**(1), 21–27. (in Japanese with English abstract).

United Nations, Department of Economic and Social Affairs, Population Division, 2012: World Urbanization Prospects, the 2011 Revision. (available at http://esa.un.org/unup/pdf/FINAL-FINAL_REPORT%20WUP2011_Annextables_01Aug2012_Final.pdf)

Upmanis, H. and D. L. Chen, 1999: Influence of geographical factors and meteorological variables on nocturnal urban-park temperature differences - a case study of summer 1995 in Göteborg, Sweden. *Climate Res.*, **13**(2), 125–139.

Watanabe, K., 1965: Principles of Architectural Planning (Kenchiku-Keikaku Genron). Maruzen Co., Tokyo, 240 pp. (in Japanese).

Watanabe, T., 1994: Bulk parametarization for a vegetated surface and its application to a simulation of nocturnal drainage flow. *Boundary-Layer Meteorol.*, **70**, 13–35.

Watarai, Y., K. Nakagawa and Y. Fukuoka, 2009a: Numerical simulation of the intense heat over the central Kanto Plain in 15–16 August 2007, using the regional meteorological model. *Jpn. J. Biometeorol.*, **46**, 35–41. (in Japanese)

Watarai, Y., K. Nakagawa and Y. Fukuoka, 2009b: Numerical experiments of the intense heat over the central Kanto Plain in August 2007 using the regional meteorological model. *Global Environ. Res.*, **11**, 71−80. (in Japanese with English abstract)

Winslow, C. -E. A., L. P. Herrington and A. P. Gagge, 1937: Physiological reactions of the human body to varying environmental temperatures. *Amer. J. Physiol.*, **120**(1), 1–22.

Yaglou, C. P. and C. D. Minard, 1957: Control of Casualties at Military Training Centers, *Amer. Med. Assoc. Arch. Ind. Health*, **16**, 304–314.

Yu, C. and W. N. Hien, 2006: Thermal benefits of city parks. *Energy Build.*, **38**(2), 105–120.